# BUCKLING INSTABILITIES OF NANOSCALE POLYMER FILMS AND COLLOIDAL PARTICLE LAYERS

A Dissertation
Submitted to the Graduate Faculty
of the
North Dakota State University
of Agriculture and Applied Science

By

Bekele Jemama Gurmessa

In Partial Fulfillment of the Requirements
for the Degree of
DOCTOR OF PHILOSOPHY

Major Department:
Physics

April 2015

Fargo, North Dakota

North Dakota State University

Graduate School

---

Title

BUCKLING INSTABILITIES OF NANOSCALE POLYMER FILMS AND COLLOIDAL PARTICLE LAYERS

By

Bekele Jemama Gurmessa

The Supervisory Committee certifies that this *disquisition* complies with North Dakota State University's regulations and meets the accepted standards for the degree of

**DOCTOR OF PHILOSOPHY**

SUPERVISORY COMMITTEE:

Andrew Croll
Chair

Alexander Wagner

Erik Hobbie

Xinnan Wang

Approved by Department Chair:

04/09/2015 Sylvio May

# ABSTRACT

Nanoscale polymer films have numerous potential applications such as protective coatings, flexible electronics, energy harvesting devices, and drug delivery systems. For realization of these potential applications, the mechanical properties of these materials and the underlying physics need to be understood.

This dissertation focuses on understanding the responses of nanoscale films to mechanical deformations. In this regard, an elastic instability was exploited to locally bend and impart a local tensile stress in a nanoscale polystyrene film, and directly measure the resulting residual stress caused by the bending. Our results indicate that the onset of permanent deformation for thin polystyrene films is an order of magnitude smaller than what has been reported for the bulk value. In addition, not only is the onset of failure strain found to be small but also it increases with increased confinement. Using similar processing techniques, the yield strain of a more complex material - poly(styrene-b-divinylpyridine) - was studied. Similar to the polystyrene films, failure in polystyrene-b-poly(2-vinylpyridine) is also initiated at extremely low strain and is influenced by thin film confinement effects. In addition, we have demonstrated that internal nanostructure of self-assembled polystyrene-b-poly(2-vinylpyridine) affects the onset of failure strain.

Having introduced an idealized heterogeneity to a sample through ultraviolet/ozone treatment, we have created samples ranging from continuous thin films to sets of isolated plates. We demonstrated that, when subjected to mechanical deformation, the unbounded plates form isotropic undulations that persist even beyond high strain. In contrast, isolated plates undergo non-isotropic undulations in the range of high strains. The non-isotropic undulation shape has been described through a simple numerical modeling subjected to controlled boundary conditions. The agreement between experiment and numerical modeling is remarkable.

Finally, through an integrated experimental methods and theoretical modeling, the response of discrete colloidal layers to mechanical deformations have been exploited. The buckling profiles measured experimentally demonstrate a great insight that the continuum model may not be able to predict the response of discrete systems. Theoretically, a granular model was constructed and structural stability analysis was investigated to predict the experimental observations. The overall agreement of the experiment and the modeling was good.

# ACKNOWLEDGMENTS

There are so many people who deserve many thanks without whom this project would have been impossible. I would like to sincerely thank my advisor and supervisor Andrew Croll for his unreserved support, excellent and generous guidance throughout my work. While working with him, I have got the chance to share his research experience which benefited me a lot. Being moved from theory to his experimental group, my start-up was not so easy. Thank you so much for your unreserved guidance and support. Thanks for being on my side for all those hard times. I would like to thank you also for introducing me to the soft matter community by giving me the opportunity to participate in many national and international conferences.

Deep gratitude is also due to my graduate committee members: Erik Hobbie, Alexander Wagner and Xinnan Wang for taking time from their busy schedule to serve on my committee. I greatly appreciate their invaluable suggestions and comments during various stages of my research.

To all my lab mates, Damith Rosairo, Joseph Miller, John Harris, Mattew Semler, Ahmed Elbaradei and Sam Brown, thank you for the enjoyable time we had during our stay together, especially during our occasional racquetball, volley ball and tennis games which I enjoy most; not the game nights though. Also many thanks to the theoretical physics groups: Eric Foard, Goetz Kaehler, Stephan Loew and Deyan Mihaylov.

Finally, I would like to thank my wife, Rahel Gemmeda for her persistent support and invaluable advice. I have no words to describe my love and appreciation for her. Had it been not for her courage to keep my little awesome boys Rebira and Oli happy everyday, including during my stay in the lab in the evenings, this thesis would have most certainly be impossible. I feel truly blessed that I met Rahel with whom I can share the rest of my life.

# DEDICATION

To my father,

Jemama Gurmessa

(1922-2007)

and

my Mother,

Shewaye Shashi

(1925-1997)

# TABLE OF CONTENTS

# LIST OF TABLES

# LIST OF FIGURES

# 1. INTRODUCTION

## 1.1. Research Motivation

In the past several decades, the electronics industry has been dominated by inorganic films (silicon technology). In recent years, polymer films have been gaining more attention in the electronics industry. This is due, in part, to newly emerging polymer thin film technologies such as flexible electronics (e.g. wearable computers, E-paper, and flexible displays), energy harvesting, drug delivery, protective coating, etc. Despite their wide potential technological applications, the mechanical properties of thin polymer films are not yet well studied, particularly when the film thickness approaches *nanometer* scales. Hence, it is essential to understand and improve the mechanical limits of these materials.

## 1.2. Research Objective

The research objective of this dissertation is to experimentally investigate the mechanical response of nanoscale polymeric materials to mechanically induced deformation. The nanoscale films are made from two systems of model materials: 1.) continuum systems which include homopolymers, block copolymers, ultraviolet/ozone oxidized polydimethylsiloxane surfaces and 2.) discrete systems (colloidal particle layers). Studying the mechanical response of these systems will bridge the gap between scientific communities independently involved in the studies of the continuum and discrete materials. Throughout this study, surface characterization techniques such as laser scanning confocal microscopy, atomic force microscopy and optical microscopy are used. The wide range of thin film applications and the importance of mechanical behavior to the function of the material gives reason to anticipate that this thesis will have a profound impact on thin film technology.

## 1.3. Outline of the Research

This dissertation discusses four projects investigated experimentally and is organized along these lines. Chapter one contains a brief introduction to the concepts of mechanical deformation of materials, the fundamentals of buckling instabilities and polymers - the cornerstones of the projects described in this thesis. Following the introduction, subsequent chapters present the methodologies, the findings and the conclusions of each project.

The first project, discussed in the second chapter, was designed to explore how to quantify the onset of failure in thin films made from an amorphous, glassy polymer that is generally rigid and relatively inexpensive - polystyrene. In the effort of reducing the size of functional devices, the thickness of polymeric materials has reached values smaller than the size of unperturbed molecule. When the film thickness is comparable to the characteristic length scale of the unperturbed molecule, interesting phenomena emerge. For example, the glass transition temperature, the inter-chain entanglement density and the elastic modulus of thin polymer films are now known to deviate from their bulk measurement as confinement increases [60, 106, 70]. While these deviations, as film thickness approaches zero, are well documented,very little work has centered on failure processes under confinement. Here, we make use of an elastic instability to locally bend a nanoscale polymer film made from homopolymer in order to induce local stress and experimentally quantify failure strain and the influence of thin film confinement on the onset of plastic deformation.

Motivated by the significant observations made in the first project - coupled with our quest to investigate more complex thin film materials - we pursued the response of thin films made from diblock copolymers to external stress. This work is presented in the third chapter. Block copolymers are a class of material made up of two or more than two chemically different homopolymers that are covalently bonded together to form a larger

and more complex macromolecule. The simplest block copolymers is a diblock copolymer which is made from two homopolymers connected by a covalent bond. Diblock copolymers are known to self-assemble into a variety of micro-phase separated morphologies depending on the relative volume fractions of the components, the number of statistical segment, and the degree of miscibility between the monomers of the two blocks [4, 5, 72, 48, 77]. Here we study the effect of such nano-structures on the plastic deformation of lamellar and cylinder forming polystyrene-b-poly (2-vinylpyridine) thin films. An important result emerging from this work is that a thin film with lamellar nanostructures will stretch further before failure compared to as cast films made from the same material.

In chapter four, we study how idealized, spatially heterogeneous thin films respond to mechanical deformations. The idealized/patterned surface layers are created by selective ultraviolet/ozone treatment of the top surface of polydimethylsiloxane (PDMS) using TEM grid as a mask. By controlling the exposure time of UV/O3, samples ranging from continuous thin films to sets of isolated small plates were created. When subjected to externally applied strains, each region responds in a very different way due to the inhomogeneity of the surfaces. While the continuous regions maintain periodic undulations (even at high strains) the patterned regions show strong localization as the applied strain increases. Often time localized deformations are associated to non-homogeneous strain fields in the materials. In this project, we investigate variation of the responses of each region as a function of globally applied and local strains. Furthermore, we develop a simple model that qualitatively describes the deformation profile heights of each region by using appropriate boundary conditions.

The final major topic of this thesis concerns colloidal layers and is presented in chapter five. In this chapter, the response of thin films made from nanoscopic colloidal particles subjected to external stress is investigated. This system is also observed to buckle out of plane forming a sinusoidal topography when a threshold stress is reached. This

is a common elastic instability seen in continuum films. In the continuum system, it has previously been shown that the threshold wavelength of wrinkling instability is directly proportional to the film thickness and the cubic root of the ratio of the elastic moduli of the film and substrate, respectively. Our finding suggests that the critical wavelength of colloidal buckling instability is independent of the particle modulus and directly related to the radius of the films.

Finally, an overall summary of the results discovered and conclusion will be presented in chapter six of the dissertation.

## 1.4. Mechanical Deformation

Mechanical behavior of a material is characterized by how it deforms when an external force is applied. When a sufficient force is applied to any material, it will cause the material to change shape (deform) [67]. Under certain conditions, an equilibrium state can be achieved after applying a stress (stress, denoted by $\sigma$, is defined as the magnitude of the applied force ($F$) divided by the area ($A$) over which the force is applied. Mathematically, $\sigma = F/A$.). Often, equilibration takes time. Time dependent deformation can also give important insights.

In order to understand the differences, it is useful to consider how atomic displacement takes place under an applied stress. At static equilibrium, each atom prefers occupying a position that minimizes its free energy. When a stress is applied, atoms move from their initial stable state because the free energy has been changed by the applied stress. If the stress is small, then only small displacement will occur and eventually the motion will cease. Upon removal of the stress, atoms will return to their original positions. This type of recoverable deformation is known as elastic deformation. In contrast, when a large stress is applied, then the material responds to the stress not only at short times but also through delayed, time dependent deformation. In this situation, a fraction of strain

is often no longer recoverable (strain, denoted by $\varepsilon$, is the change in length ($\Delta L$) of a material relative to the initial length ($L_0$). It is a measure of by how much a material departs from its natural configuration. Mathematically, $\varepsilon = \Delta L/L_0 = (L_f - L_0)/L_0$ in 1D, where $L_f$ denotes the final length.). Microscopically speaking, the nonrecoverable deformation occurs when the atomic motion is so large that atoms move over a potential hill, to the next local free energy minima. Once atoms move over the potential hill, then even if the stress is removed, they may not have enough energy to go back to their original positions. This kind of deformation is irreversible and said to be plastic deformation. The stress at which the material ceases elastic deformation and starts showing plastic deformation is termed the *yield point or yield stress* or the point of the onset of plasticity whereas the corresponding strain is termed *yield strain*. The yield point is a material dependent property. i.e. every material possesses a distinct yield point value. For example, it was documented that the yield strain of bulk polystyrene varies between 1% to 2.5% [1, 74] using traditional bulk techniques. However, common techniques such as tensile tests, nanoindentation are limited when attempting to characterize polymer thin films due to their relative softness and fragility. Thus, it is essential to develop a better technique to fill this gap. In this thesis, a surface buckling instability based metrology is used to overcome these experimental difficulties and to determine the onset of plasticity of glassy polymer thin films.

## 1.5. Buckling Instabilities

### *1.5.1. Buckling of Thin Plate*

Suppose a thin plastic ruler is picked up and held at the two ends and gently compressed. The ruler will not buckle out plane at first. It absorbs any displacement by compressing in plane. Next, the ruler responds by buckling out of plane when a

characteristic threshold compressive force is achieved. Buckling instabilities typically occur when the applied compressional force exceeds the material yield stresses. According to Euler-buckling theory [114], the deflection, y(x), of thin rod of length $L$ from its flat axis is related to the applied load, $F$, through the differential equation

$$\bar{E}I\frac{d^2y(x)}{dx^2} + Fy(x) = 0 \tag{1.1}$$

where $\bar{E}$ is the reduced elastic modulus of the material (i.e. $\bar{E} = 1/(1-\nu^2)$ where $\nu$ is the poisson ratio), $I$ is the second moment of area for the buckling cross-section. Solving this equation with fixed edge boundary conditions (i.e. y(0) = y(L) = 0), gives $F = \frac{\pi^2 \bar{E} I n^2}{L^2}$, where n is the mode of deformation. Since n=1 is the minimum, it corresponds to the critical applied force, $F_c$, required to buckle a simply supported columnar elastic material of a specified cross-sectional geometry. This leads to

$$F_c = \frac{\pi^2 \bar{E} I}{L^2}. \tag{1.2}$$

The moment of inertia, $I$, varies with the geometry of plates considered. For example, a plate of rectangular cross-section with width b and thickness $h$ has the moment of area: $I = bh^3/12$ and hence the critical buckling load will be

$$F_c = \frac{\pi^2 \bar{E} b h^3}{12 L^2}. \tag{1.3}$$

Until the applied force reaches this threshold value ($F_c$), the plate absorbs elastic energy and then buckles out of plane when the critical force is attained to release the stored/absorbed energy. Beyond this critical force, the system responds by undergoing periodic undulations.

In general, the mechanism behind the formation of periodic surface buckling instabilities lies in the competition between bending and stretching deformation modes [2, 32]. In the framework of Hookean elasticity, which is valid for small strain (a strain that allows

one to consider that the elastic response of a given material is linear) in general, the elastic energy, $E_{elastic}$, of the plate reads [2]:

$$E_{elastic} = \frac{1}{2}\int\int dxdy \int_{-h/2}^{h/2} dz(\sigma_{ij}\varepsilon_{ij}) \tag{1.4}$$

where x and y denote coordinates along the center surface of the plate, while z is in the transverse direction. Notice that in the stress, $\sigma_{ij}$, has two indices - the first index refers to the plane on which the stress is acting while the second one refers to the direction of the stress on this plane. For pure bending (bending that doesn't involve twisting), also known as isometric deformation, the lengths along the center surfaces are not changed upon deformation. Any out-of-plane component of the stress on the top and bottom surfaces are zero because the surfaces are assumed free boundaries. As a result, the implicit sum in equation 1.4 runs only over the in-plane indices $i, j = \alpha, \beta \in \{x, y\}$ which reduces equation 1.4 to

$$E_{elastic} = \frac{1}{2}\int\int dxdy \int_{-h/2}^{h/2} dz(\sigma_{\alpha\beta}\varepsilon_{\alpha\beta}). \tag{1.5}$$

By approximating the in-plane components of strain, $\varepsilon_{\alpha\beta}$, which are responsible for bending, as $\varepsilon_{\alpha\beta} \sim z/R$, (which will be discussed below), and the constitutive equation, $\sigma_{\alpha\beta} = E\varepsilon_{\alpha\beta}$, where $R$ is the radius of curvature of the neutral axis of the plate, equation 1.5 reduces to the expression of plate bending:

$$E_{bending} \sim \frac{1}{2}\int\int dxdy \frac{E}{R^2(x,y)} \int_{-h/2}^{h/2} z^2 dz. \tag{1.6}$$

Integrating over $z$, the bending energy becomes [2]

$$E_{bending} \sim \frac{1}{2}\int\int dxdy \frac{Eh^3}{12}\left(\frac{1}{R(x,y)}\right)^2, \tag{1.7}$$

or simply

$$E_{bending} \sim Eh^3. \tag{1.8}$$

In order to approximate the stretching energy, an assumption made is that the dependence of the energy density on the transfer coordinate ($z$ running from -$h/2$ to $h/2$) is isotropic. This essentially means that the stress is averaged over the whole thickness implying that, in contrary to the assumption made for bending energy approximation, the plate involves stretching (or compression) at the outer and inner edges, respectively, does not hold.

$$E_{stretching} = \frac{1}{2}\int\int dxdy(\sigma_{\alpha\beta}\varepsilon_{\alpha\beta})\int_{-h/2}^{h/2} dz. \tag{1.9}$$

Integrating over z gives the elastic (stretching) energy along the center line [2] given as

$$E_{stretching} = \frac{1}{2}\int\int dxdyh(\sigma_{\alpha\beta}\varepsilon_{\alpha\beta}). \tag{1.10}$$

By introducing the constitutive equation, $\sigma_{\alpha\beta} = E\varepsilon_{\alpha\beta}$, equation 1.10 reduces to

$$E_{stretching} \sim Eh\int\int dxdy(\varepsilon_{\alpha\beta})^2, \tag{1.11}$$

or

$$E_{stretching} \sim Eh. \tag{1.12}$$

In order to realize the response of geometrically different plates to similar external stress, let us compare equations 1.8 and 1.12. The bending energy scales as $\sim h^3$ while the stretching energy scales as $\sim h$. Consequently, for very thin plates, the energy of pure bending deformations (no twisting) is much lower than those involving significant stretching. From this comparison it is clear that the thickness of the plate plays a crucial role in determining which mode of deformation (bending or stretching) is preferable (see Fig. 1.1). When a thin, stiff material and a thick, soft material are subjected to an externally

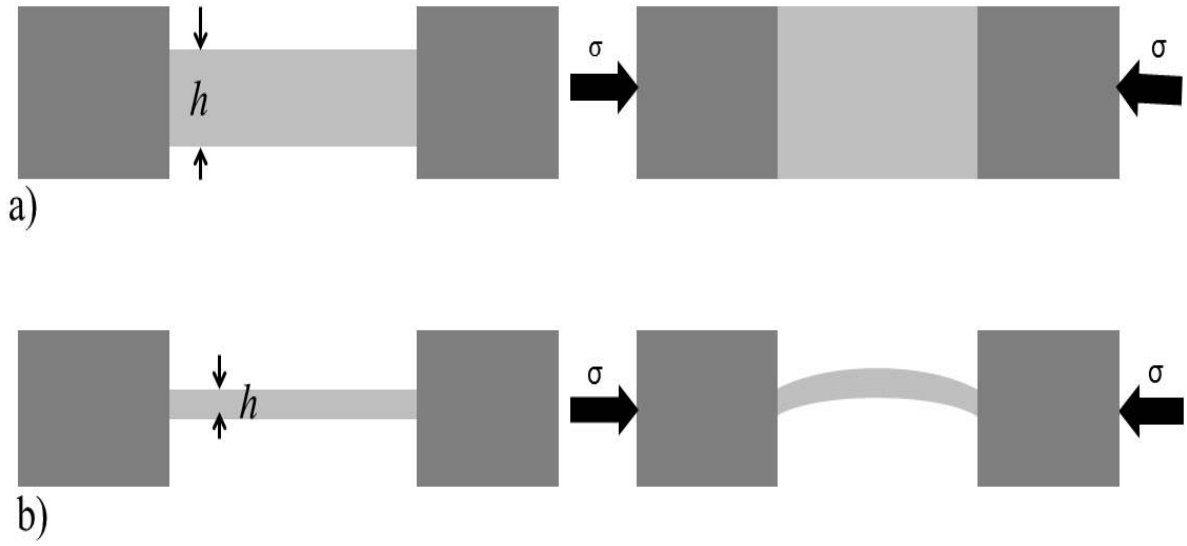


Figure 1.1. Illustration of how different material geometries are responding to an applied compressive stress, $\sigma$: a) a thick bulk material ; b) a thin plate. While thick plate prefers stretching, thin plates prefer bending to stretching upon uniaxial compressional stress. The width of the sample denoted by b is shown into the page and $h$ denotes the thickness.

applied compression (see Fig. 1.1), the thick material prefers stretching (see Fig. 1.1a) while the material with small thickness will bias the deformation towards bending as shown in Fig. 1.1b. The low energy obtained in a pure bending deformations can be explained in what we experience on a daily basis. For instance, if we pick up a sheet of paper and try to deform it into cylindrical or spherical shape, we know from every day experience that it is much easier to bend a sheet of paper into shapes such as conical or cylindrical than to pull (or stretch) it onto a spherical shape [123].

Now that we have established how each plate responds to mechanical deformation when treated separately, a composite of the two materials, a thick bulk solid and a thin plate, is considered. When the two materials are laminated together, they prevent each other from attaining their preferred state of deformation. At small strains, the energy required for simple compression is smallest, however as compression increases, buckling the thin

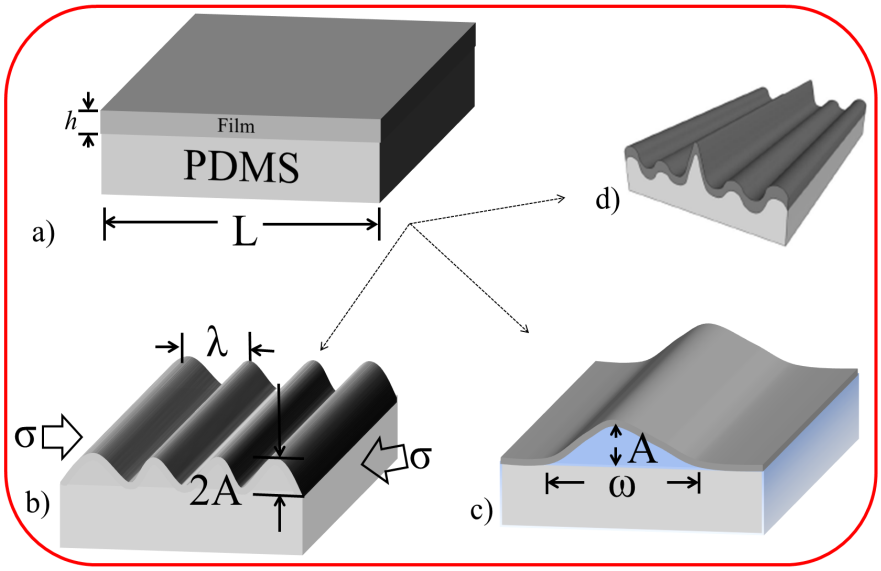


Figure 1.2. Schematic illustrations of: a) a thin film of thickness $h$ and length $L$ bound to a softer substrate (PDMS). When subjected to uniaxial compression, $\sigma$, the composite first responds by undergoing b) surface wrinkling with periodicity of $\lambda$ and amplitude of $A$. Further compression may lead to c) delamination of width $\omega$ and amplitude $A$ or to d) a more focused deformation (localization).

film becomes more favorable (Fig. 1.2). Ultimately compressing the composite leads to a periodic instability, wrinkling, which combines aspects of both bending and stretching.

### *1.5.2. Buckling of Thin Plate Coupled with Soft Foundation*

A material can respond to an applied stress in a variety of ways. For example, when a thin plate described in the previous section is bound initially to a stress free elastic substrate is subjected to a compressive uni-axial stress, the plate will initially be compressed in-plane. As compression increases, the plate will buckle out of plane in a repetitive sinusoidal pattern (known as surface wrinkling) [110, 20] when a critical wrinkling stress is reached. Increasing the applied stress further may result in either delamination or folding or both [31, 81, 118].

*1.5.2.1. Wrinkling Mechanics*

Surface wrinkling can be modeled mathematically through a force balance or an energy balance [21, 43] in order to obtain equations that govern the deformation of the plate. In this thesis we follow the force balance approach used by Timoshenko [114]. Consider a beam bending under a distributed lateral load *q(x)* (i.e. the restoring force of an elastic foundation) whose intensity varies with $x$ along the beam and axial load F as shown in Fig. 1.3. We will assume a Hookean substrate such that $q(x) = Ky(x)$ where $K$ is Winkler's modulus (the reaction force per unit area of the elastic foundation or substrate) [126] given by ($K = E_s b\pi/\lambda(1-\nu_s^2) = \bar{E}_s b\pi/\lambda$) with the variables s, $\nu$ , $b$ and $\lambda$ referring respectively to substrate, Poisson ratio, width of the plate (film) and the wavelength of the distortion. Consider an element of length $dx$ between two cross sections taken normal to the original (undeflected) axis of the beam as indicated in Fig. 1.3. Assume that the lateral load remains constant over the distance $dx$ and positive in the positive $y$ direction. Furthermore, the shearing force $V$ and the bending moment $M$ acting on the sides of the element are assumed positive in the directions shown.

The balance of forces acting on the beam along the y directions is

$$-V + qdx + (V + dV) = 0. \tag{1.13}$$

The balance of moments acting around point n, assuming small deflection, is

$$M + qdx\frac{dx}{2} + (V + dV)dx - (M + dM) + F\frac{dy}{dx}dx = 0 \tag{1.14}$$

From equation 1.13,

$$q = -\frac{dV}{dx}. \tag{1.15}$$

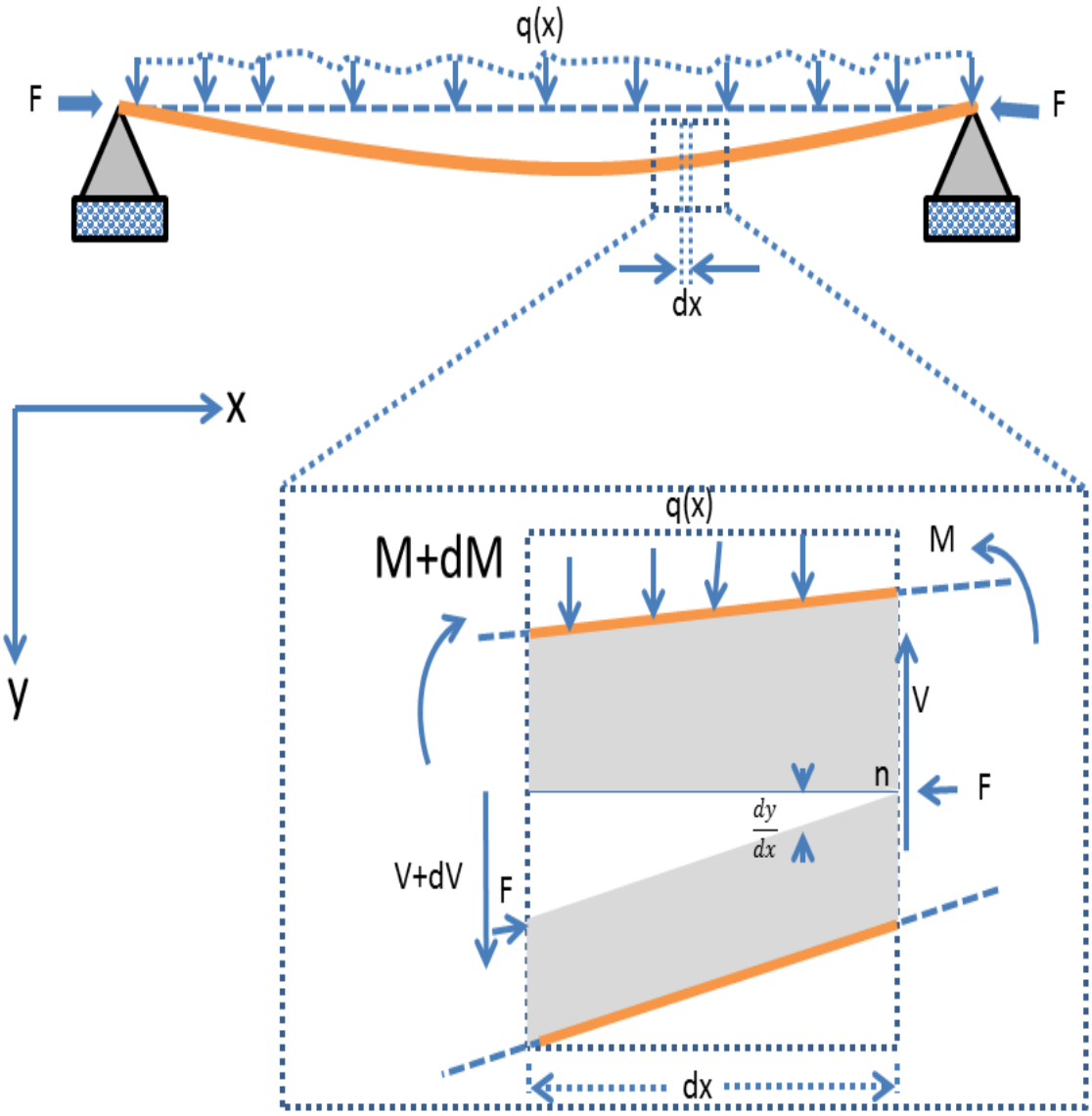


Figure 1.3. Beam bending under a distributed load. A beam bent under a distributed load $q(x)$ and an axial load F with inset representing a differential element of the beam in equilibrium. Redrawn inspired from [114].

Plugging for dV from equation 1.13 into equation 1.14 and neglecting higher order terms (i.e. neglecting terms containing $(dx)^2$), the shear force will be:

$$V = \frac{dM}{dx} - F\frac{dy}{dx}. \tag{1.16}$$

The curvature of the axis of a beam is related to the bending moment [114], $M$, by

$$\bar{E}_f I \frac{d^2y}{dx^2} = -M \tag{1.17}$$

where $I = wh^3/12$, $w$ and $h$ are respectively the moment of inertia, the width and thickness of the film and $\bar{E}_f$ is the reduced modulus related to the modulus and Poisson ratio of the film, $\nu_f$, by $\bar{E}_f = E_f/(1-\nu_f^2)$. Combining equations 1.15,1.16 and 1.17, along with the definition of $q(x) = Ky(x)$, yield:

$$\bar{E}_f I \frac{d^4y(x)}{dx^4} + F\frac{d^2y(x)}{dx^2} + Ky(x) = 0. \tag{1.18}$$

In equation 1.18, the first and third terms refer to the classical Euler-Bernoulli beam-bending equation where as the second term consists of the effect of the applied force $F$. If the thin plate is not bound to an elastic foundation(i.e. the third term in equation 1.18 is zero) equation 1.18, reduces to the equation governing the buckling of a column (see equation 1.1).

Assuming the instability causes a sinusoidal vertical displacement of the surface of the form $y(x) = A\sin(kx)$, the minimization of the force (i.e. $\partial F(x)/\partial\lambda = 0$) leads to the determination of critical wavelength

$$\lambda = 2\pi h \left(\frac{\bar{E}_f}{3\bar{E}_s}\right)^{\frac{1}{3}}. \tag{1.19}$$

Equation 1.19 is independent of the applied strain and is the basis for surface wrinkling metrology [84, 21]. Furthermore, the critical stress and strain required to trigger the instability will be

$$\sigma_{cw} = \frac{F_c}{hb} = \left(\frac{9}{64}\bar{E}_f\bar{E}_s^2\right)^{\frac{1}{3}} \tag{1.20}$$

and

$$\varepsilon_c = \frac{\sigma_{cw}}{\bar{E}_f} = \frac{1}{4}\left(\frac{3\bar{E}_s}{\bar{E}_f}\right)^{\frac{2}{3}} \tag{1.21}$$

respectively. Since $\lambda$ is independent of the applied strain, amplitude of the wrinkling is derived by assuming that the release of tensile strain in the system is the same as the over-strain ( the difference between the applied strain and the strain required to cause the instability):

$$\varepsilon - \varepsilon_c = \frac{1}{\lambda}\int_0^{\lambda}\sqrt{1+\left(\frac{dy(x)}{dx}\right)^2}dx - 1. \tag{1.22}$$

Equation 1.22 represents the contour length of a wrinkle over one period. To show this, suppose a length $L_0$ went into a buckling wavelength under a small angle approximation (i.e. $L_0 \sim \lambda$). After buckling, the new length (x-component) will be $L$. This $L$ will be obtained from the contour length through $L = \int_0^{L_0} dscos(\theta)$ where $ds = \sqrt{(1+\dot{y}^2)}dx$ and $\theta$ is the angle made between the displaced plate and the horizontal and $\dot{y}$ is derivative with respect to x. Then, the released tensile strain will be $\Delta L/L_0 = L/L_0 - 1$. Assuming small deflection of the plate, $cos(\theta) \sim 1$ to the first order (small angle approximation). Equating the strain-released with the over-strain, as assumed earlier, it becomes $\varepsilon - \varepsilon_c = L/L_0 - 1$. Substituting for L gives equation 1.22 which after integration yields

$$\varepsilon - \varepsilon_c = \frac{\pi^2 A^2}{\lambda^2}. \tag{1.23}$$

Combining equations 1.19 and 1.21 with equation 1.23 gives

$$A = h\sqrt{\frac{\varepsilon}{\varepsilon_c} - 1}. \tag{1.24}$$

These three parameters defined in equations 1.19, 1.21 and 1.24 represent the fundamental measurable features of the surface instability: the wavelength of the instability, the critical strain where the instability occurs and the evolution of the amplitude with the applied strain.

#### *1.5.2.2. Delamination*

The delamination-buckling of thin films refers to a buckled film when it is partly debonded from the substrate [54]. Delamination is mostly dictated by the strength of adhesion between the film and the substrate as well as the balance of the mechanical strain energy (i.e. delamination takes place when the wrinkling energy exceeds the adhesion energy between the film and the substrate). Many early studies of buckle-delamination assume fixed-end conditions at the edge of delamination, which essentially neglect the effect of elastic deformation in the film at the edges. That is, the deflection and slope of the delaminated film are both zero at the clamped (fixed-end) edge (i.e. y(x) and $\partial y(x)/\partial x$ are both zero at the delamination front). With these clamped boundary conditions and the assumption that the buckling displacement remains reasonably small, the displacement of the delaminated film is given by $y = A/2(1 + cos(\pi/b)x)$ in the post-buckling. The stress necessary to cause the delaminated thin film to buckle is predicted by the classical Euler buckling theory to be [130, 16]

$$\sigma_{cd} = \frac{\pi^2}{3}\left(\frac{h}{\omega}\right)^2 \bar{E}_f, \tag{1.25}$$

where $h$ is the thickness of the film, b is half the width of the delamination and $\omega$ is the width of the delamination. According to Hong-Hui Yu and John W. Huchinson [130], the

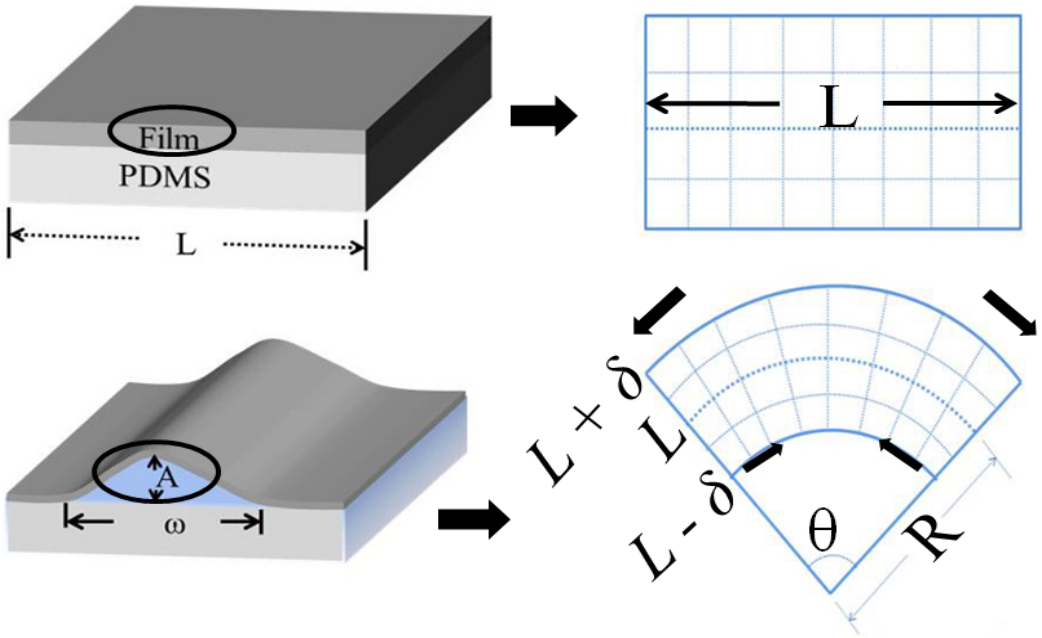


Figure 1.4. Illustration of pure bending deformation of thin plates. For pure bending deformations, the length along the center surface remains the same while the inner and outer edges are compressed and stretched, respectively.

stress, $\sigma_{cd}$, is independent of the substrate modulus, but depends on the relative sizes of the delamination at the interface of film and substrate, $h/w$.

### *1.5.2.3. Bending*

The surface instabilities (such as buckle-delamination and buckle-wrinkling) induced mechanically in a thin polymer film bound to a soft substrate have one thing in common: the *bending of the film* under consideration. When the system is subjected to compression, the thin film eventually undergoes a buckling instability resulting in bending. Bending changes the geometry of the film.

Although the delamination of a compressed thin film has been studied both theoretically [123] and experimentally [87] for many years, very little work has focused on the study of the effects caused by locally bending thin films (i.e. delamination) such as

the onset of plastic deformation. Consider a film delamination as if it were a clamped plate under uniaxial compression. In this case, the delaminated-buckled film takes on a geometry as dictated by the general solution to the equilibrium plate equation. When the clamped boundary conditions (same as the classical Cauchy boundary condition) (i.e. $y(x = \pm b) = 0$ and $\partial y(x)/\partial x \mid_{x=\pm b} = 0$) are applied to the buckled film, the post buckled shape of the delaminated film becomes [130, 118]:

$$y(x) = \frac{A}{2}\left(1 + cos(\frac{\pi x}{b})\right), \tag{1.26}$$

where A and $b$ refer to the amplitude and half the width of the delamination, respectively, assuming that the buckling displacement remains reasonably small. The curvature of the film at the crest of the delamination can be quantified as a function of the amplitude and width of the delamination as

$$\kappa \sim \frac{\partial^2 y(x)}{\partial x^2} \sim \frac{A}{\omega^2}. \tag{1.27}$$

In order to estimate the strain induced by the bending, a classical beam bending approach [114, 2] in which an initially flat plate of length $L$ undergoes stretching (at the outer most edge) and contraction (at the inner most edge) by a small amount $\Delta$, yet leaves a neutral (an unstretched) region at the center of the plate (See Fig. 1.4) is considered. Under bending, the final length of the plate at any distance $z$ from the neutral axis will be $l_f = \theta(R(x,y) + z)$, whereas at R(x,y) (or z = 0), the neutral axis will be $l_0 = \theta R(x,y)$ where R(x,y) is the radius of curvature of the neutral axis which is related to curvature, $\kappa$, as $R(x,y) = 1/\kappa$ and $\theta$ is the angle that subtends the curved plate as show in Fig. 1.4. Thus the strain induced in the film at a distance of z from the neutral axis will be

$(l_f - l_0)/l_0 = z/R(x,y) = z\kappa$. At the crest of the delamination, $z = h/2$, the surface strain, in terms of its curvature, becomes

$$\varepsilon_s = z\frac{\partial^2 y(x)}{\partial x^2} \mid_{z=h/2} \sim \kappa h. \tag{1.28}$$

Having quantified the localized strain, one can find the stress the film is undergoing due to bending. This implies that localized bending leads to a type of stress localization in the film.

#### *1.5.2.4. Stress Localization*

In order to understand the concept of stress localization, consider a large spherical container with a piece of paper inside. When the volume of the container is reduced, the paper first deforms smoothly and then develops sharp points and bends. The resulting sharp structures are commonly described as crumpling and represent a form of energy focusing [123]. Initially, the elastic energy of the piece of paper is smoothly distributed. As the container shrinks, the piece of paper's smoothly distributed elastic energy becomes more nonuniform and concentrated within strongly bent regions. The thinner the initial sheet, the more pronounced the stress concentration and strongly bent regions become. Likewise, in polymer thin films, this kind of deformation where much distortion is focused within a narrow region of surface is termed as folding. Folding is considered a characteristic feature of nonlinearity and is commonly observed in films deposited on water [93] or foam [96] substrates. Similarly, when a film is deposited on elastic substrate, as has already been described, the surface of the film initially forms arrays of wrinkles (unless the film is ultra thin [31]) as the applied stress exceeds the critical stress required for the onset of wrinkling [110, 20]. However, upon further compression, a few wrinkles will eventually develop into delamination as shown in Fig. 1.2(c) or to a more focused deformation known as localization (see Fig. 1.2(d)). These kinds of deformations are an indication of energy

focusing. Such localized buckling amounts to the gathering of energy from the entire surface into a small region. It is noteworthy that stress focusing usually leads to failure of materials such as delamination, crazing, shear deformation zone, fracture.

## 1.6. Brief Introduction to Polymers

### *1.6.1. The Structure of Polymers*

Polymeric materials are everywhere; they are found in objects that human beings come across on a daily basis such as the cars we drive, the computers we use, the packaging materials we use in food courts and grocery stores, etc. What is a polymer, anyway? A polymer is a very large molecule made up of smaller repeating units called monomers which are joined sequentially with covalent bonds forming a chain. Polymer can be classified as naturally occurring or synthetic. Proteins, DNA, starches and cellulose are some examples of naturally occurring polymers. Examples of synthetic polymers are plastics and elastomers. Materials that are commonly termed plastics such as polystyrene, polyethylene are synthetic polymers. Most polymers are synthesized through polymerization process as illustrated in Fig. 1.5. The figure illustrates examples of polymerization of polystyrene and poly (2-vinyl pyridine) - polymers mainly used in this thesis. The former one is made from styrene while the latter one is from 2-vinyl pyridine monomers, respectively. The degree of polymerization depends on the number of monomers $N$ in a chain. Notice that the double bonds in the monomers must break for the addition polymerization to take place. It is also worth noting that the two polymers shown in the figure (polystyrene and poly (2-vinyl pyridine)) similar in their physical sizes as can be seen from their chemical structures. The only distinct feature is in the presence of the nitrogen atom in the side groups of the poly (2-vinyl pyridine).

The molecular architecture of a polymer is determined by how monomers are assembled during polymerization. For example, a polymer chain can be synthesized

in a wide variety of architectures such as linear, branched, networked, etc. (Fig. 1.6). The simplest molecular architecture is a linear (Fig. 1.6(a)) molecule that consists of identical monomer units connected end-to-end while branched (Fig. 1.6(b)) and cross-linked (Fig. 1.6(c)) polymers contain, respectively, branches bonded covalently to the main chain and monomers of one chain bonded to the monomers of a chemically different chain through covalent bonds.

One distinguishing feature of most synthetic polymers is that they are polydisperse (i.e. all the polymer chains in the sample have different number of monomers). If all the polymers in a given sample are made up of the same number of monomers, then the sample is monodisperse and all molecules have a molecular weight simply given as $M = NM_0$, where $M_0$ denotes the molecular weight of a monomer that appears in the chain. Practically, number averaged and weight averaged molecular weights are used to estimate the size of a polymer. Number averaged and weight averaged molecular weights are mathematically defined, respectively, as $M_n = \sum_i^\infty N_i M_i / \sum_i^\infty N_i$ and $M_w = \sum_i^\infty N_i M_i^2 / \sum_i^\infty N_i M_i$ where $N_i$ is the number of polymers with molecular weight $M_i$. The ratio $M_w/M_n$, known as polydispersity index, measures the distribution of polymer sizes in a sample. Monodisperse samples have a polydispersity index of one while larger polydispersity index corresponds to samples with broader chain distributions.

Polymers can also be classified depending on the chemical type of the monomer units constituting the chains. These are homopolymers and copolymers. When a polymer is made by joining only one type of N small monomer units with covalent bonds, it is termed as homopolymer (see Fig. 1.7(a)). The chemical formula for such polymer is -$(A)_N$-, where **A** is the monomer and the integer $N$ represents the number of monomers that constitute the chain. By combining different monomers, another class of macromolecule called heteropolymers with unique properties will be formed. For example, macromolecules containing two different monomers are called copolymers with a variety of architectures such

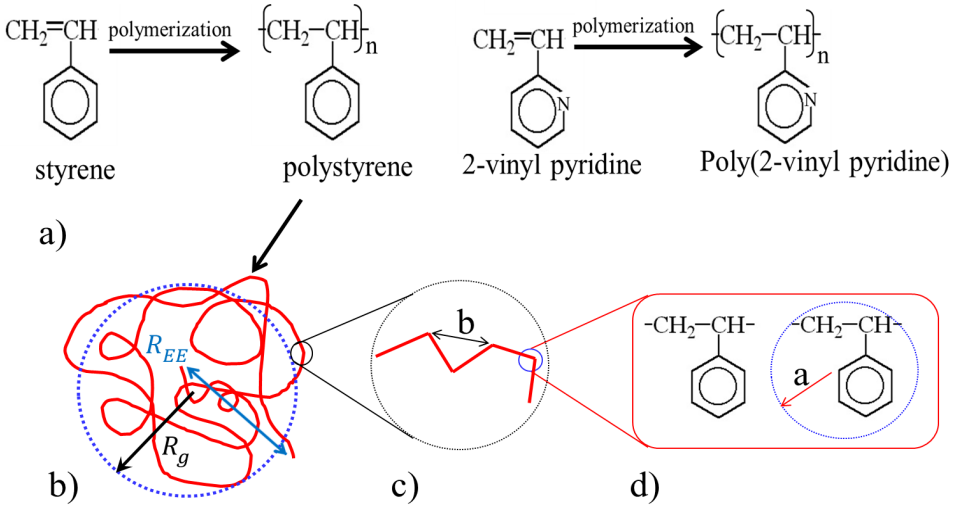


Figure 1.5. a) Example of polymerization of the two polymers mainly used in the thesis: a) polystyrene and poly(2-vinylepyridine). b) schematic illustration of polystyrene at different length scales. The red line in the circle of (b) denotes the polystyrene chain in part (a). The characteristic length over which segment correlation is lost (Kuhn length) is shown in (c) and the actual molecule is shown in the blow up as illustrated in (d) with monomer size of *a*.

as random copolymers, alternating copolymers, block copolymers, etc. Block copolymers, for example, are made by covalently bonding two or more than two polymer blocks together to form a larger and more complex macromolecule. Block copolymers containing two, three and multi blocks connected together are known as diblock, triblock and multiblock copolymers, respectively (see Fig. 1.7(b-e)).

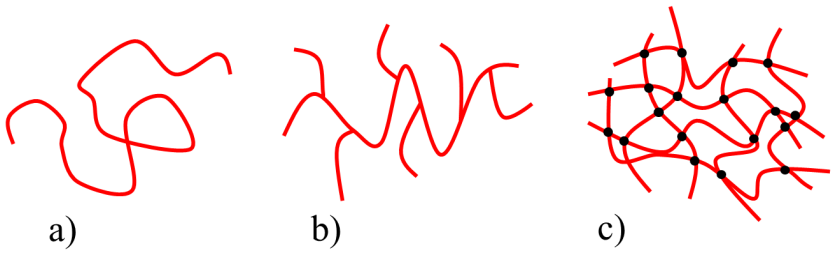


Figure 1.6. Examples of polymer architectures: a) linear, b) branched molecule and c) cross-linked network.

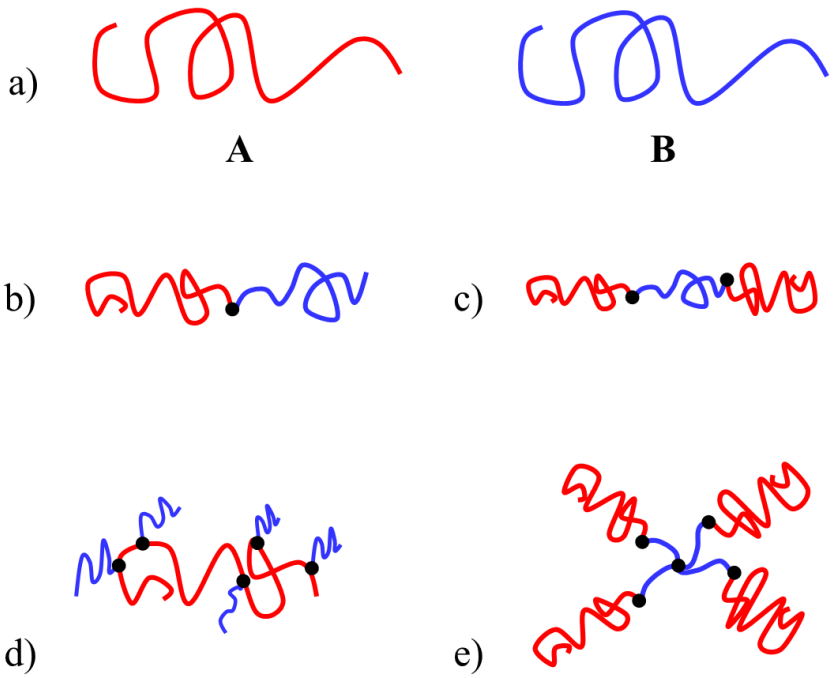


Figure 1.7. Schematic representation of common AB block copolymer architectures: a) homopolymer A & B b) diblock, c) triblock, d) graft block and e) four arm starblock.

Structurally, polymeric materials can be amorphous (see Fig. 1.8(a)) or semi/partially crystalline (see Fig. 1.8(b)). Amorphous polymers have chains arranged in a completely random manner and lack order whereas semi-crystalline polymers have partially ordered crystalline structures [99]. In order to understand the difference between these two types of polymers, one can imagine amorphous polymers as plateful of boiled spaghetti which are entangled and coiled up in a random fashion. On the other hand, a crystalline polymer can be visualized as uncooked spaghetti where all the chains are highly oriented and well-ordered in the same direction. In reality, a complete crystallinity is impossible to achieve. More often, polymers are semi-crystalline. Semi-crystalline polymers are those composed of both amorphous and crystalline regions as shown in the schematics of Fig. 1.8(b). The typical examples of amorphous and semicrystalline polymers are, respectively, atactic polystyrene and isotactic polystyrene. Atactic polystyrene have the functional groups attached to the back-bone in a random fashion. Since this random

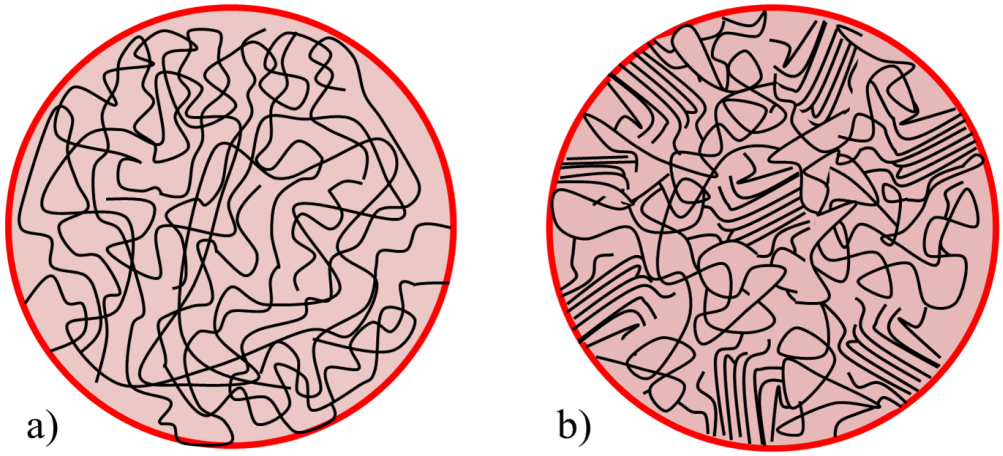


Figure 1.8. a) Amorphous polymer with entangled chains, b) Semicrystalline polymer.

positioning prevents the chains from aligning with sufficient regularity, atactic polystyrene cannot be crystalline and thus they are amorphous. In the isotactic polymers, the functional groups are attached from one side of the back-bone polymer. These polymers usually make semicrystalline structures.

The differences in crystallinity of polymeric materials lead to differences in physical properties. For example, the variation of relaxation modulus (defined as the stress divide by strain as recorded after 10s of constant straining) as a function of temperature of both semicrystalline and amorphous polystyrene is illustrated in Fig. 1.9. The figure comprises of five main regions denoted as I, II, III, IV and V which correspond, respectively to, the glassy, glass transition, rubbery plateau, rubbery flow and liquid flow regions. In region I, the modulus of the polymer is surprisingly constant. In this glassy state, the molecular motions are largely restricted to vibration and short-range rotational motions which implies that there is very little segmental mobility.

In the glass transition region, the modulus of polystyrene (the glass transition temperature of polystyrene is $\sim$100 $^{\circ}$C)[1] drops by a factor of 1000. The behavior of the polymer is described as leathery. In this region, long-range, coordinated molecular motion

[1] discussed in detail in chapter two

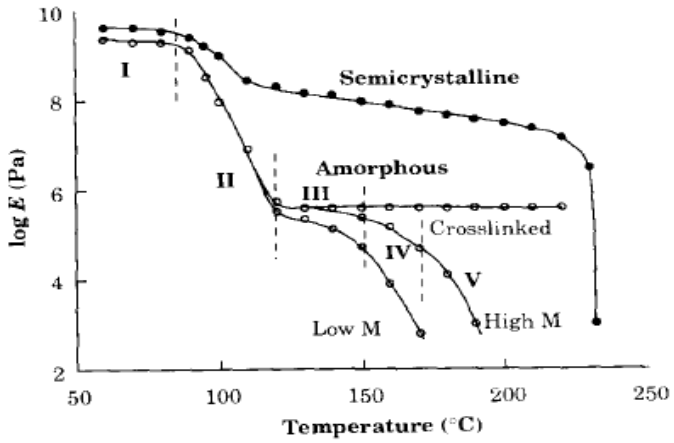


Figure 1.9. The logarithm of the relaxation modulus as a function of temperature for semi-crystalline (isotactic) polystyrene and fully amorphous (atactic) polystyrene in three versions: low molar mass uncross-linked, high molar mass uncross-linked and cross-linked. Note that isotactic are polymers having functional groups attached on the same side of the chain whereas atactic are polymers whose functional groups are completely random). (adapted from [41]).

begins [41, 109]. Above the glass transition region (region III), the modulus becomes almost constant once again. The width of the 'plateau' depends on the molecular weight of the polymer; it is much longer for a high $N$ polymer compared to a low $N$ polymer, as illustrated in Fig. 1.9. Also, compared to the cross-linked polymer, the uncross-linked polymers show a pronounced drop in modulus at high temperature.

The semicrytalline polystyrene (isotactic polystyrene) shows a weak (slow drop) glass transition at 100°C due to softening of the amorphous component of the two phase (amorphous and semicrystalline) polymer. When the crystalline component (which is unchanged by $T_g$) [41] of the semicrystalline polymer melts, the modulus shows a pronounced drop as can be seen from Fig. 1.9.

### *1.6.2. Polymer Conformations*

A polymer chain moves continuously from one state to another in solution or the melt (i.e. absence of solvent) due to thermal energy and relatively low barrier to rotations

about single bonds. As a result, it changes its shapes incessantly. The instantaneous shape of a polymer chain in a melt or solution is called a *conformation* [113]. For a linear polymer of N monomers and a bond vector of $\vec{a}$, the end to end vector is given by the sum of the individual bond vector, $\vec{R}_N = \sum_i^N \vec{a}$. If a polymer is in its extended state, the maximum length will be $R = Na$. However, the more realistic view of a polymer molecule in a melt (or solution) is the random coil picture (i.e. a polymer exhibits a Gaussian random coil or move in a random walk fashion in a melt state). In such configuration, there is no preferred bond orientation implying that $< \vec{R}_N >= 0$, where the ensemble average, $< >$, is over all possible states of the system. Thus, the overall size of the coil for linear polymers can be characterized by the root mean square end-to-end distance, $R_{EE} = \left\langle \vec{R}_N^2 \right\rangle^{1/2} = \left\langle \sum_i^N \vec{a}_i . \sum_j^N \vec{a}_j \right\rangle^{1/2} = \left( \sum_i^N \sum_j^N \left\langle \vec{a}_i . \vec{a}_j \right\rangle \right)^{1/2} = \left( a^2 \sum_i^N \sum_j^N \left\langle \cos\theta_{ij} \right\rangle \right)^{1/2}$. For the freely jointed chain model (a type of model with a constant bond length $a = |\vec{a}|$ and no correlations between the directions of different bond vectors), $\langle \cos\theta_{ij} \rangle = 0$ for $i \neq j$ and 1 for $i = j$. Hence, $R_{EE} = aN^{1/2}$, where $N$ is the size of the polymer chain and $a = |\vec{a}|$ is the size of the monomers (or the bond length between consecutive C-C atom on the back bone of the polymer) constituting the chain (see Fig. 1.5(b)). The root mean square end-to-end distance, $R_{EE}$, is the measure of the average distance between the two ends of a polymer chain [111]. However, for branched polymers, $R_{EE}$ is not well defined, because they have too many ends. Hence, the ideal way of characterizing the size of such polymers is radius of gyration, $R_g$. The square radius of gyration is defined as the average square distance between monomers in a given conformation and the center of mass of the polymer ($R_g^2 = 1/N \sum_i^N (\vec{R}_i - \vec{R_{cm}})^2$, where $\vec{R}_i$ and $\vec{R_{cm}}$ denote the position vector and the center of mass position vector, respectively, of a given polymer conformation). For an ideal linear chain $R_g$ is related to $R_{EE}$ as $R_g = R_{EE}/\sqrt{6}$; implying that a polymer molecule can be described by length scales ranging from the size of monomer, $a$, to the overall size of the coil, $R_{EE}$ [99] (see Fig. 1.5b).

Another equally important length scale often used in describing the size of a polymer chain is *Kuhn length*, a characteristic distance over which correlations are lost between segments of a freely jointed chain. Here, instead of considering the local bond lengths of the chemical structure itself, an effective bond length $b$ is constructed such that $N$ freely jointed segments of bend length $b$ constitute the actual polymer. The newly constructed equivalent chain has two unique properties: it has the same maximum end to end distance, $R_{max}$, and the same mean-square-end-end distance, $\langle R^2 \rangle$, as the actual polymer [99]. Mathematically, the contour length of this equivalent freely jointed chain is $R_{max} = bN$, and its mean-square and-to-end distance is $\langle R^2 \rangle = Nb^2 = bR_{max}$.

### *1.6.3. Polymer Thin Films*

The demand for miniaturized functional devices is consistently growing. The production of such products requires components with structure sizes in micro/nanometer range. This is accomplished by the reduction of one of the dimensions of the raw materials to nanometer or micrometer scale compared to the remaining two dimensions. A material with one dimension in a nano/micrometer length scale is known as a thin film. A typical example is polymer thin film. Polymer thin films are made from polymer solutions in a variety of ways. The most common one is spin coating, where a dilute solution in a solvent is made to a glassy state through evaporation of the solvent.

Thin films are used for a wide range of emerging applications including flexible electronics (like wearable computers, E-paper, and flexible displays) [19, 62], energy harvesting [115], protective coatings (e.g. drug delivery) [112], adhesive [3], etc. Many previous studies of polymer thin films focused mainly on understanding of varieties of phenomena associated with reduced dimensionality (thickness). For example, variation of glass transition temperature, reduction of inter-chain entanglement density and variation of elastic modulus of thin polymer films are well studied as the film thickness is decreased.

The mechanical aspects of thin polymer films are not yet well studied, particularly when the film thickness approaches *nanometer* scales. Hence, it is essential to understand the mechanical limits of thin polymer films.

## 1.7. Introduction to Colloids

What are colloids? "Colloids" refer to homogeneous suspension/dispersion of small solid particles in a fluid medium [8, 124]. The typical examples of colloidal suspensions include milk, paints (filled with particles which stick to surface when they dry), blood (filled with blood cells) and polystyrene and silica spheres in water. The size of colloidal particles can vary from nanometers to micrometers. The fraction of volume occupied by these particles (also referred to as packing fraction) is the key control parameter of the colloidal suspension. For example, at low volume fraction, colloids can easily diffuse and behave like a gas and undergo simple Brownian motion. However, sufficiently large volume fraction leads to a transition from being a gas, simple Brownian motion to a jammed state, where their movement is highly constrained [53]. Researchers propose the idea of jamming as a way of understanding the glass transition in colloids [9, 53].

Colloids are often unstable systems because, given time, the initially homogeneous suspension tends to sediment to the bottom due to gravity (in fact this depends on the size of the particles) or tends to float to the top surface if they are less dense than the dispersing fluid. The individual small colloidal particles stay in suspension only when the Brownian forces are strong enough to prevent such segregation. However, when colloidal particles come in contact, they may stick together permanently. As time evolves, more and more particles may stick together in a process known as aggregation [56]. Once they aggregate, sedimenting will take place. In order to maintain the dispersed state of colloids, the attractive force between the particles is modified through processes such as charge stabilization (a process in which the layers of counterions in the fluid are attracted to the

surface of colloids by electrostatic fields, produce repulsive force) or steric stabilization (coating the colloids by polymer layer which increase osmotic pressure, causing the repulsive force).

Colloidal particles which are not aggregated are often likened to simple hard-spheres. Hard spheres, which are idealizations of billiard balls in free space, behave as free particles in which the particles neither attract nor repel over distances beyond their diameter and hence don't aggregate together.

It is not our intention to describe the jamming process or the phase behavior of colloidal suspensions. Instead, we will use these brief introductory remarks as a starting point for our study of the response of colloidal layers to mechanical deformation as presented in chapter 5. In this regard, 2D monolayers of colloidal arrays will be constructed under the assumption of hard spheres, thus no interaction between the colloids is anticipated.

# 2. ONSET OF PLASTIC DEFORMATION IN NANOSCALE POLYSTYRENE FILMS

## 2.1. Background

In this chapter we present the results of our experimental investigation of the onset of plastic deformation in nanoscale polystyrene films. Polystyrene (abbreviated as PS) is an amorphous, glassy polymer that belongs to the group of thermoplastics. Thermoplastics are types of polymers that can be melted and cooled back to solid multiple times (like butter) unlike thermosets which remain in a permanent solid state (like rubber). Other thermoplastics include polyethylene, polypropylene, poly(vinyl chloride). Polystyrene is a comprehensively studied, glass-forming polymer with well-known bulk material properties which makes it ideal model material for studying certain behavior of polymers. The main focus of the current chapter is to present a new approach that was developed in order to quantify the magnitude of the yield strain in nanoscale films.This chapter is intended to answer several questions: 1.) How big/small is the yield strain just before the film starts failing? 2.) How does the yield strain evolve with the change in film thickness? 3.) Is the yield strain dependent on the entanglement density, the glass transition temperature or other extensive properties? Before delving into the experimental descriptions, a brief review and discussion of some background ideas pertaining to the topic will be presented.

### *2.1.1. Deformation and Failure in Bulk Glassy Polymers*

The term glass has a broader definition. It encompasses every solid that possesses a non-crystalline (i.e. amorphous) atomic-scale structure. Glasses commonly used for

[0]Andrew Croll and Bekele Gurmessa designed and conducted the experiment in this chapter in close cooperation. The work in this chapter is published in [46].

window panes, tableware, etc. are made from silica (main constituents of sand). The lighter alternatives to silica glasses are made from polymers (e.g. laboratory safety glasses, CD cases). Glassy polymers are ubiquitous materials belonging to the group of thermoplastics that are widely used in our daily life and industry. The most common glassy polymers are Polystyrene (PS), Poly(methyl methacrylate) (PMMA), Poly(vinyl chloride) (PVC) and Polycarbonate (PC) [82, 108]. These materials show rich behavior when subjected to mechanical deformation. For example, they exhibit an initial stress-strain response for small deformation (Hookean regime) that is approximately linear. This is followed by a crossover to often-complex nonlinear behavior. Under compression, the non-linear behavior is characterized by onset of plastic deformation (yield), strain softening and strain hardening. The terms strain softening and strain hardening refer, respectively, to noticeable reduction in stress for small change in strain and monotonically growing in mechanical stress for small change in strain. The softening and hardening regions can lead to large deformations before finally ending with sample failure. In the linear region, the material recovers its initial shape if the applied stress is removed. As the stress-strain behavior crosses over to non-linear, removing the applied stress may not bring the sample back to its initial shape (zero strain). This can mean the material has undergone permanent plastic deformation. Several researchers have demonstrated these properties, particularly for bulk polymers, both through computer simulations [18, 119] and through experiment [1, 94, 102]. Experimentally, standard techniques such as compression and tensile testing are used to study the response of such bulk materials. The traditional methods require the specimen to be in a bulk form. If the sample is in nanoscale size, the standard technique may not be applicable. In this regard, it is essential to develop a new technique that allows us to quantify the magnitude of yield strain in nanoscale films.

It is important to note that the deformation of polymers is highly dependent on temperature. At low temperatures, a polymer may be glass-like with large Young's modulus

while at high temperatures it may be rubber-like with reduced Young's modulus. There is an intermediate temperature range called *glass transition range* in which the polymer is neither glassy nor rubber-like with an intermediate modulus [13, 109] and has viscoelastic properties.

### *2.1.2. Glass Transition Temperature in Bulk Polymers*

When a liquid sample is sufficiently cold and the cooling occurs rapidly, the microscopic dynamics of the particles constituting the sample cease. This sudden arrest of the dynamics is called the *glass transition*. This phenomenon is best described by a fundamental parameter called glass transition temperature, $(T_g)$, where a material shows a viscous liquid like behavior above this temperature and solid like behavior below $T_g$ [38].

In the bulk, glass transition temperature can be measured experimentally by using standard techniques such as Differential Thermal Analysis (DTA) and Differential Scanning Calorimetry (DSC). In DSC, two samples are considered: a reference sample with predetermined heat capacity and a sample under experiment. Both samples will be subjected to the same temperature throughout the experiment while the amount of heat absorbed/released by the sample under experiment is measured. When the $T_g$ is reached, there will be a sudden jump in the heat absorbed/released by the sample. DTA is similar to DSC except the heat flow to both the reference sample and the sample under investigation remains the same instead of the temperature. Because heat is now supplied to the two holders at the same rate, a difference in temperature between the sample and the reference develops, which is recorded by thermocouples embedded in the sample and reference. Measuring physical properties such as heat capacity, coefficient of thermal expansion, enthalpy, specific volume, etc. with any standard method will show a sudden jump which is attributed to the glass transition [109]. The temperature at this point is the experimental glass transition temperature.

The glass transition temperature is not a true thermodynamic phase transition [42] (note that in a true thermodynamic phase transition the $n^{th}$ order transition is considered as one in which all the $(n-1)$ derivatives of the free energy are continuous and the $n^{th}$ derivatives of the free energy are discontinuous). This is because of its dependence on the rate of cooling. For example, if the specific volume of a glass forming liquid is measured as a function of temperature, the expected result can be shown schematically as in Fig. 2.1. When the specific volume in the glassy state is extrapolated toward the specific volume in the liquid state, a specific point where the two lines intersect corresponds to the glass transition temperature. A material that is cooled faster will have larger $T_g$ compared to the same material during a slow cooling. When a material is cooled faster, the molecules of the liquid do not have enough time to rearrange and the system is trapped in a less stable high-energy state (far from true equilibrium). In contrast to fast cooling, the system will have enough time to explore deeper, minimum energy (equilibrium state) in the slow cooling rates [42].

### *2.1.3. Glass Transition in Polymer Thin Films*

The concept of a glass transition is not yet perfectly understood in bulk materials [39, 41]. Even less is known about how reduced dimensionality of a material affects the glass transition temperature. For example, despite more than 20 years of research, there is still no consensus of why the values of glass transition temperature of thin films do not agree with that of the bulk polymers' values. In the effort of understanding the fundamental features of the glass transition in nanoscale materials, a variety of experimental techniques have been developed over the past few decades. The most common ones are ellipsometry, x-ray reflectivity, positron annihilation lifetime spectroscopy and Brillouin light scattering [57, 30, 39]. These approaches directly or indirectly probe the coefficient of thermal expansion or change of polymer density (index of refraction) of the sample as the

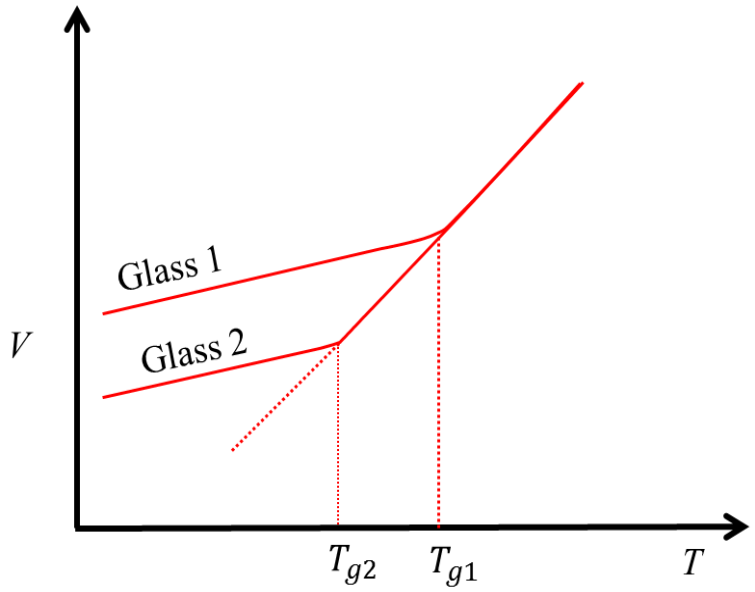


Figure 2.1. Schematics of volume V versus Temperature T of a glass forming material for two different cooling rates. When a material is cooled faster, it undergoes a larger $T_g$ as shown in glass 1 and slower cooling rate results in a lower $T_g$ value as in glass. Redrawn inspired from ref [30].

.

temperature is increased or decreased. Despite the different techniques employed, many researchers [60, 57, 30, 39, 98] have shown that the glass transition temperature of thin films do not agree with their corresponding values in the bulk as the confinement increases (see subsection 2.1.3.1).

In order to explain the variation of the glass transition temperature with film thickness, Keddie and his coworkers [60] developed a phenomenological model termed a *layer model* based on the notion of cooperativity. The model makes the assumption that, when annealed, the film consists of a high mobility surface layer (fluid like layer) on top of the less mobile bulk like layer; which together constitute the overall thickness of the film. The phenomenological equation they developed to fit their data is given as

$$T_g(h) = T_g(bulk)\left[1 - \left(\frac{\ell}{h}\right)^{\delta}\right], \tag{2.1}$$

where $h$ is the film thickness, $\ell$ is the near surface mobile layer $\sim 3nm$ and the exponent $\delta \sim 1.8$. There are two main reasons reported as to why the surface layer is more mobile when the sample is annealed: an increase in the number fraction of chain ends (that act as a plasticizer for the $T_g$ of the polymer) and reduction of entanglement density (due to the limitation imposed by the boundary) at the free surface [117, 106]. In addition, Keddie and coworkers [60] applied the bilayer model to their study of the coefficient of linear thermal expansion of polymer thin films in the glassy and melt states. In this study the researcher found that the coefficient of expansion significantly increases with increasing film confinement. By assuming the coefficient of thermal expansions of the mobile layer and the bulk to follow simple additive relations, the researchers showed the best curve fitting to the data as

$$\alpha = \ell/h(\alpha_L - \alpha_B) + \alpha_B, \tag{2.2}$$

where $\ell$ is the thickness of the fluid layer, $\alpha_L$ and $\alpha_B$ are, respectively, the expansion coefficients of the layer and the bulk and $h$ is the over all thickness of the film. In thinner films the expansivity of the mobile layer is dominant over the thicker films'; in which case the over all expansivity tends to remain finite.

Further attempts to understand the effects of thin film confinement on the glass transition temperature have been focused on the importance of interfacial interactions: interaction between film and substrate and film and air. This prompted two different thin film geometries. These are supported films and free-standing films.

#### *2.1.3.1. Supported Film*

This geometry refers to a thin film supported by a substrate from the bottom and air from the top. The study of glass transition temperature variation in supported polystyrene thin films was first carried out by Keddie et al., in 1994 [60]. Since the first investigation by Keddie, there have been many studies of the glass transition temperature of polystyrene on

different substrates using a variety of experimental techniques [39, 57, 61, 125]. Although a variety of techniques have been used by many researchers, the conclusion was amazingly similar - the glass transition value for polystyrene reduces below the bulk value as a function of thin film thickness and this decrement becomes more pronounced as the confinement increases. Forrest et al. [39] took a step further to summarize the overwhelming conclusions reported by different researchers and documented the result as illustrated in Fig.2.2, where the solid line is the best to the data using equation 2.1. As can be inferred from the figure, there is apparent reduction of the glass transition temperature below the bulk value as the film thickness decreases below 100 nm. It is also worth noting that the effect is essentially independent of the molecular weight of the polymers [57]. On the other hand, there are studies reporting increasing $T_g$ as the film confinement increases. For example, poly(2-vinylpyridine) (P2VP) and poly(methyl methacrylate) (PMMA) supported on native-silicon oxide coated substrates revealed increment in $T_g$ with reduced thickness. The former one showed a very strong increase [90] while the latter one showed small increase [120]. These increase of $T_g$ on silicon substrate was attributed to the fact that both polymers (P2VP and PMMA) possess a repeat unit structure that can hydrogen bond with the hydroxyl groups on the silica substrate. In contrast, by replacing the silicon substrate by a gold substrate, Keddie et al. showed that $T_g$ suppression similar to polystyrene [61, 125] was observed using ellipsometry. Despite an apparent controversies, it is a fact that there are no reports for the glass transition temperature values for polystyrene films to show increases as the confinement increases.

#### *2.1.3.2. Free Standing Film*

When the glass transition temperature measurements for supported polystyrene films were first reported, there were controversies about the effects of the substrate [120, 61, 125]. In particular, the scattered data collected from the different measurement techniques

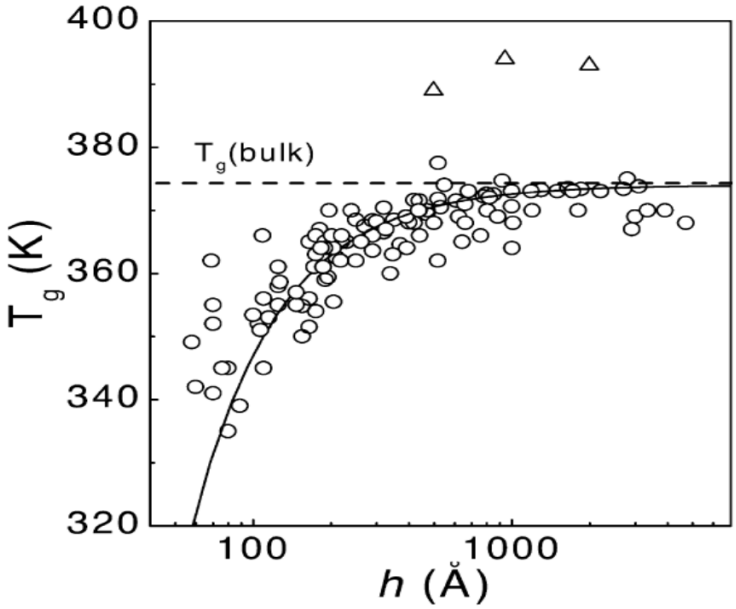


Figure 2.2. Compilation of all measured $T_g$ values for supported PS films. "Republished with permission of ELSEVIER , from ref [39]. Copyright (2001)."

.

as compiled in Fig. 2.2 and the controversial report of results for the same polymer but different substrates were attributed to the interaction between the film and the substrate. Motivated by the controversial reports (i.e. some researchers report the $T_g$ increases [120] yet others report $T_g$ decreases [61, 125] for the same polymer but different substrates), researchers designed a free standing experiment using Brillouin light scattering (BLS). Free standing film refers to a thin film bounded by air front and back without a substrate. In this case, the sample is placed on a circular sample holder (washer) with a hole of a certain *mm* scale diameter. The results of the free standing polystyrene films were first reported by Forrest and coworkers [38], which removed the complication imparted by the substrate. Firstly, there is analogy in the way the $T_g$ reduction below the bulk value takes place between the two systems: supported and free standing, albeit the reduction is more pronounced in the case of free standing films. Unlike the supported films, however, it has been conclusively shown that a molecular weight dependence of the glass transition temperature exists in the free standing $T_g$ measurement [26, 25, 39]. Glass transition

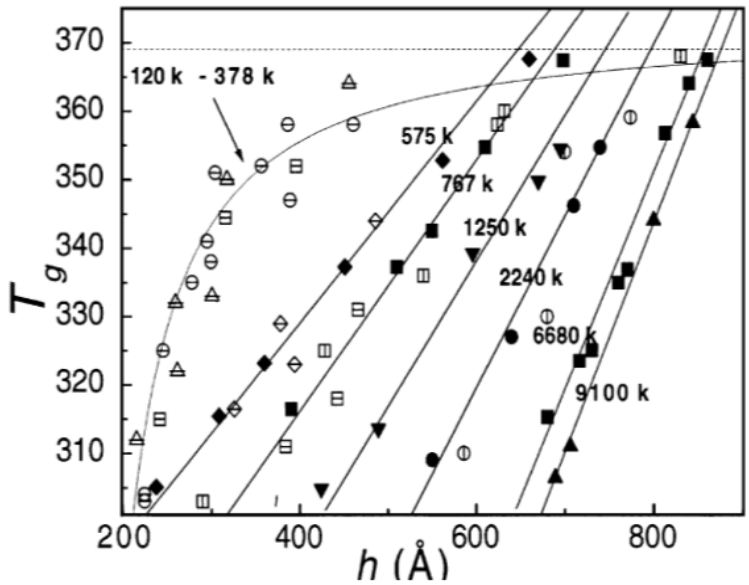


Figure 2.3. Measured glass transition temperature values for free standing PS films. "Republished with permission of ELSEVIER, from ref [39]. Copyright (2001)."

.

temperature varies both linearly (for $M_w \geq 575k$) and non-linearly (for$120k \leq M_w \leq 378k$) as a function of thickness as shown in Fig. 2.3.

### *2.1.4. Polymer Chain Entanglement*

In the bulk melt state, polymer chains exhibit Gaussian conformational properties which represent random walks of the backbone chain. As discussed in chapter one, an average lengthscale is commonly expressed by the root-mean-squared end-to-end distance, $R_{ee} \sim aN^{1/2}$, where $N$ is the number of monomers per chain and $a$ is the size of the monomer. Due to random thermal motions, an ideal polymer chain explores a pervaded volume proportional to $R_{ee}^3$. In this volume, there will be interactions of the chain under consideration with itself (*interachain*) and with other chains (*interchain*). Some of these interactions restrict the mobility of a polymer chain through entanglements. Entanglements are considered as the cornerstone of many unique polymeric properties such as very high melt viscosity, toughness and rubber viscoelasticity [40, 73, 106].

In a highly confined geometry, the thickness of the film can become comparable to (or even less than) the characteristic length scale, $R_{ee}$. When it does, the interchain entanglement density decreases because segments from other chains are excluded from a specific chain's pervaded volume. The overall entanglement density remains fixed since the self-entanglement density increases [106].

When subjected to mechanical strain, a thin film responds by creating shear deformation zone (a thinning or neck that forms in the film) and/or crazing (small nanoscopic voids formed due to the strain) based on the magnitude of the applied strain. One of the properties describing shear deformation zone (SDZ) and crazing is maximum extension ratio, $\lambda$. The theoretical definition of $\lambda$ is the ratio of the distance between two entanglement points for ideal Gaussian chains before and after a strain and is $\sim M_e^{1/2}$ as defined by Kramer [66]. $M_e$ refers to a molecular weight between entanglement cross links. In their recent publication, Lun Si et al. extended this definition to thin films undergoing SDZ and showed that $\lambda$ is related to the ratio of the initial thickness, h, of the film that went into forming the deformation to the thickness, $h_c$, of the deformed region after an applied strain by assuming conservation of volume in the neck and the film region [106]. They then inferred the effective entanglement molecular weight $M_{eff}$ by measuring $\lambda$ as illustrated in the inset of Fig. 2.4. From this measurement $M_{eff}$ in the thinest films is seen to be greater than in the thicker films. This implies that thiner films can stretch further before failure due to the loose entanglement networks in the thin film. Thus, interchain entanglement also decreases as the film thickness reduces below $\sim 100nm$.

### *2.1.5. Mechanical Properties*

Another interesting observable which may be related to film thickness is the mechanical properties of the film. Similar to the $T_g$, Lee and his colleagues have shown that polymer thin films exhibit reduced elastic modulus as compared to their counterparts in

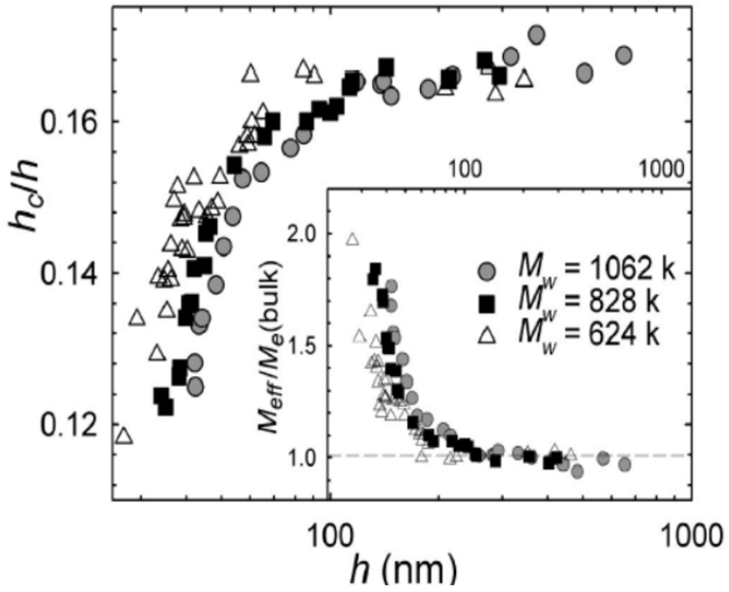


Figure 2.4. Variation of the ratio of the neck thickness,$h_c$, to the film thickness, h as a function of thickness for three different molecular weights. The inset illustrates the replotted data of $M_{eff}$ normalized to the bulk value. "Adapted from ref [106] with permission. Copyright (2005) American Physical Society."

bulk by using surface wrinkling metrology [70]. They concluded that polystyrene thin films have a markedly reduced elastic modulus compared to their bulk values as demonstrated in Fig. 2.5. The justification these researchers give for the reduction of the modulus as the thickness decreases is related to the reduction of inter-chain entanglement density near the free surface. As pointed out earlier, reduced entanglement density would enhance the molecular mobility but reduce the intermolecular forces; and hence the reduction of the modulus.

Most recently, another group of researchers reported a controversial result on the mechanical properties of polystyrene films [22]. These researchers performed nanoindentation experiment of a series of glassy polymer films on silicon substrates using AFM and found that the moduli of PS, PMMA, and PC increase while that of PVC remains the same as the film thickness decreases as shown in Fig. 2.6. This result contradicts with what has been reported by Lee's group for PS films. The enhancement of the moduli, as the film

thickness is reduced, is attributed to the interaction between indentation induced stress on the film and stiff supporting substrate. These controversial reports stem, in part, from lack of well established methods of probing the mechanical properties of polymer thin films, especially when the film thickness approaches zero.

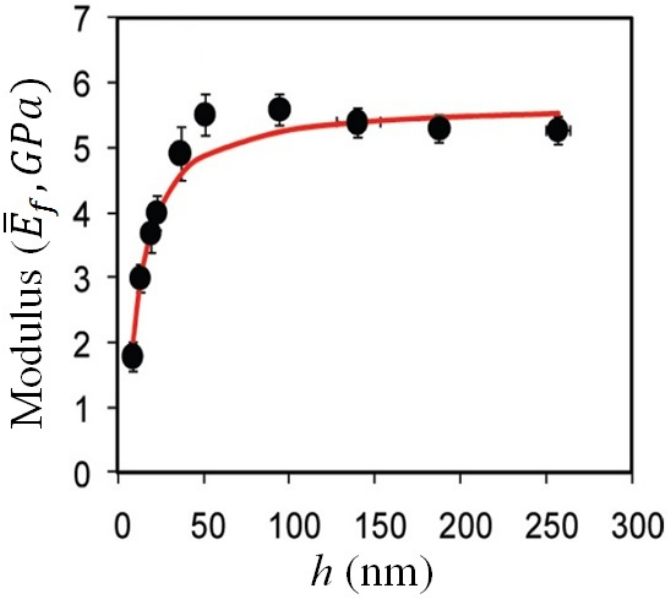


Figure 2.5. Elastic modulus as a function of thickness of polystyrene film. The solid line denotes a best fit to the data using bilayer model. "Adapted from ref [70] with permission. Copyright (2007) American Chemical Society."

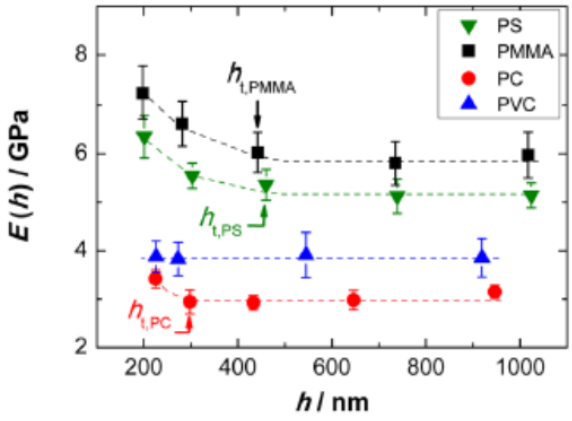


Figure 2.6. Effective elastic moduli as a function of thickness of a series of glassy polymer films. The dashed lines are guides for the eyes. "Adapted from ref [22] with permission. Copyright (2014) American Chemical Society."

## 2.2. Experimental Procedures

In the past several decades, there have been numerous theoretical models [123, 15] and experimental approaches [87, 93, 110, 20] describing pattern formation due to buckling surface instabilities. However, the validation of the effect of residual stress caused by local bending during buckling of polymer thin films are still lacking. In the following sections, the procedures used to investigate the role of local stress induced by bending thin films and the results found will be presented.

### *2.2.1. Substrate Preparation*

Proper substrate preparation is the most important step in order to achieve a successful experiment. In our experiment, the substrate is made from cross linked polydimethylsiloxane (PDMS). PDMS is a Si based organic polymer that is a highly viscous liquid in its raw form and optically transparent. A curing agent and PDMS prepolymer (Dow chemical Corning, Sylgard 184) are thoroughly mixed in different weight ratios such as 1:10, 1:20, 1:30. Thorough mixing for about ten minutes is needed in order to make sure that the curing agent is uniformly distributed. While mixing, the mixture will be filled with air bubbles. These bubbles need to be removed (degassed) before curing by placing the sample in a vacuum oven (Napco 5831 Vacuum Oven) and close and release the vacuum valve for sometimes until the trapped bubbles are fully removed. After degassing, the polymer mixture is poured into a 9.6 cm x 9.6 cm petri dish to a thickness of about 3 mm and cured at 85$^{\circ}$C for two hours in a vacuum oven and then are cooled in the oven for the next 12-15 hours. After cooling, the PDMS substrate is cut into a rectangular sections of 1.2 cm x 7 cm x 0.3 cm. Furthermore, the elastic modulus of this substrate is measured by tensile test (Instron 5545 Tensile Tester: 100N load cell, environmental chamber). The average modulus measured are 0.113MPa and 0.094MPa for the 1:20 and 1:30 weight ratio, respectively.

### *2.2.2. Polymer Solution Preparation*

In order to prepare the thin films, the polymer should be dissolved or dispersed in a solvent. In this chapter, different homopolymers and a block copolymer were used as listed in table 2.1 (Polymer Source Inc.). The polymer is dissolved in toluene (Anhydrous 99.8%, Sigma-Aldrich Inc.) with concentration varying from 0.5% to 3% by weight. Once mixed, the solution will be kept at room temperature for two to three days for a complete dissolution before use. Finally, the solution will be filtered through a micro-pore system (pore size 0.482 $\mu$m, Cadence Science Inc.) before spin coating.

### *2.2.3. Thin Film Preparation*

Once the solution is ready, various methods can be used for the preparation of thin polymer films. Among others, spin coating is one of the most commonly used method [91, 69, 45]. In order to spin coat, a drop or two (depending on the required thickness) of the the solution prepared is dispensed atop a solid substrate, a freshly cleaved piece of mica that is fixed to a glass microscope slide by capillary force. Mica is used due to its uniform flatness. Next, the glass slide is placed on a stationary spin-coater (a machine used for spin coating) disk. The microscope slide is then rotated at high speed (ranging from 500 rpm- 6000 rpm) based on the thickness required. The film then spreads uniformly by centrifugal forces on the mica, and the volatile solvent is rapidly driven off. Higher polymer concentrations or viscosities result in thicker films, and higher angular velocities of the disk result in thinner films.

The coated thin film is cut into approximately 1 cm x 1 cm pieces (see Fig. 2.7) and transferred to a clean deionized water surface (Milli-Q) through a process known as flotation. Finally, a piece of floating film is lifted up and transfered on to a stress free flat polydimethylsiloxane (PDMS) substrate by using a very smooth, piece of mica held with a tweezer.

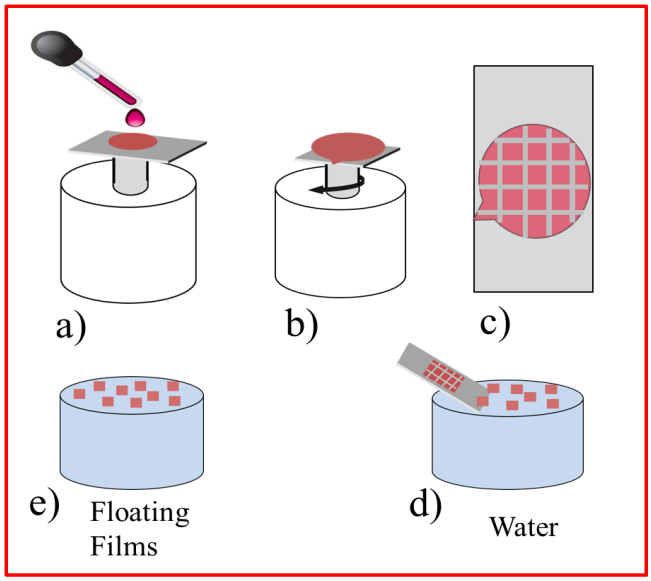


Figure 2.7. Schematics illustrating the procedures of making freely floating thin films: a) a drop of solution is placed on mica attached to glass slide; b) spin-coating a thin layer of the solution on a mica and c) cut the uniform thin film into a desired size; d) immerse the glass slide aslant into water and the film is detached from the mica substrate; e) the film freely floats on the surface of water.

### *2.2.4. Mechanism of Compression*

The arrays of wrinkles and delaminarions are obtained through homogeneous in-plane compressive stress applied externally as explained in the previous sections. The in-plane compressive stress is exerted to the bilayer (film and substrate) by a custom built strain stage. The strain stage allows careful control of strain which results in arrays of wrinkles and delaminations perpendicular to the direction of strain. It consists of two grips (one fixed and the other one moving) in order to strain the substrate. The strain stage also posses a locking groove that is useful in order to maintain an applied strain when separating the stage from its base and motor for various purposes such as drying the loaded sample in vacuum oven.

Table 2.1. List of the molecular details of the polymers used in the chapter.

| Samples | $M_N$(kg/mol) PS | $M_N$(kg/mol) P2VP | PDI |
|---|---|---|---|
| PS | 1100 | - | 1.10 |
| PS | 115 | - | 1.00 |
| PS-b-P2VP | 40.5 | 40.0 | 1.10 |

### *2.2.5. Mechanism of Inducing Reversible Deformation*

Previous experimental studies of the mechanics of wrinkling and delamination [83, 20, 110, 59, 52] have utilized compression-induced stresses from a prestrained substrate. In our study, we utilize stresses induced from a nominal tension, not compression. That is, the substrate-film composite is loaded into a uni-axial extension strain stage and then placed under extension along its long axis. As extension is increased, the incompressible nature of the rubber leads to a Poissonian contraction in the sample's other dimensions. This compression induces buckling, and eventual delamination of the thin polymer film. Most importantly, the stress can then be removed returning the sample in its initially flat configuration. As illustrated in Fig. 2.8a, a flat film subjected to a uniaxial compression results in several wrinkles and a tall delamination. When the compression is completely removed, the film returns to the initially flat state.

### *2.2.6. Measurement Tools*

In all cases, we make use of atomic force microscopy (AFM-DI Dimension 2100) and Laser Scanning confocal microscopy (LSCM-Olympus Fluoview 1000) in order to collect and analyze our data. Both AFM and LSCM provide the topography of the films (i.e.they are both surface characterizing tools). AFM is primarily used for high resolution images and thickness measurements. On the other hand, LSCM is used to measure the wrinkle wavelengths and delamination widths. More importantly, through optical

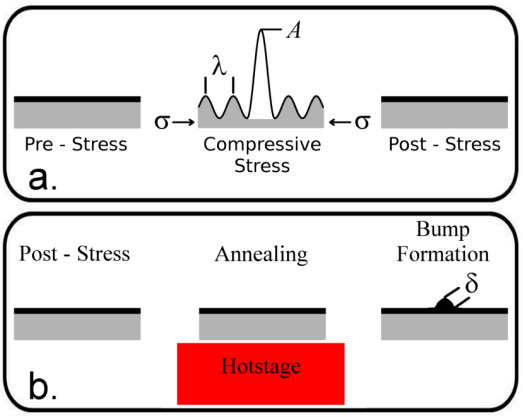


Figure 2.8. Schematic illustration of the two stage experiment. a) Stage 1:Preannealing: a thin polymer film is placed on a soft elastomer substrate, uniaxial compression is added and finally removed. The sample is left in a measurably flat state. b) Stage 2: Postannealing:the sample, after all applied stress has been removed, is placed on a hot-stage and annealed. During annealing, "bumps" form at locations correlated with high curvature during the compression stage of the experiment.

sectioning, we also determine the height of each pixel along the delamination. Additionally, confocal microscopy provides a significant imaging improvement over conventional (or light) microscopes. It creates sharper images by incorporating the ideas of point-by-point illumination of the sample and rejection of out-of-focus light via pinhole at confocal point (i.e. by having the pinhole, the microscope can efficiently reject out of focus light). The light that passes through the pinhole is measured by a detector i.e. photomultiplier tube (PMT). The detector is attached to a computer which builds up the image, one pixel at a time, gives more detailed 2D images, and allows collection of data in three dimensions.

### *2.2.7. Measurement Methods*

In order to examine what happens to the surface of the film corresponding to the initial delamination spot, two independent approaches have been used to scan the topography of the film after the film has been relaxed. These methods are termed direct and indirect. The former refers to a method of scanning the topography of the relaxed

(in its flat state) film with AFM in order to detect any signs of damage as a result of the preceding bending. However, because of the smallness of the amplitude of the damaged film and the scan size of AFM, it requires stitching many separate AFM images together; and for that reason this method is error-prone. Also, the softness of the substrate along with the rigidity of the film make imaging through the direct method difficult due to probe/film interactions. In order to alleviate these problems, we devised an alternative method termed the indirect method. This method is used to measure the surface of the film after the relaxed film has been annealed above the glass transition temperature of the polymer making up the rigid film. It has a benefit of increasing the amplitude of the bump height. Furthermore, LSCM alone can be used to measure independently the curvature and the extent of plastic deformation. This approach cancels out calibration differences that may occur between the two instruments.

## 2.3. Modeling of the Flow of Thin Film

In this section we derive a simple scaling model that will help to understand how the thin film flows in response to the local residual stress when annealed above the glass transition temperature of the bulk polymer. Films annealed above the $T_g$, changes to fluid (flowing film). Since the density of the film (fluid) is not expected to change (because to change the density, high pressure is required; which we don't apply), the film can be considered as an incompressible (constant density). In the incompressible Newtonian fluid, $\sigma = \eta\dot{\gamma}$, where $\sigma$ = force/area, $\eta$ is constant viscosity and $\dot{\gamma}$ is the local velocity gradient. Hence, the flow of the film (fluid) can be described by the principles of hydrodynamics of incompressible Newtonian fluids.

### *2.3.1. Hydrodynamics*

In hydrodynamics, the equations of motion of an incompressible, Newtonian fluid are given by the Navier-Stokes equations. The Navier-Stokes equations state that an infinitesimal volume element moving with flowing fluid is accelerated due to the forces acting on it [68]. Mathematically,

$$\rho\left(\frac{\partial \mathbf{u}}{\partial t} + (\mathbf{u}.\nabla)\mathbf{u}\right) = -\nabla p + \eta\nabla^2\mathbf{u} + \rho\mathbf{g}, \tag{2.3}$$

where $\mathbf{u}$ is the average velocity and $\rho$ is the density, $p$ is the pressure within the film. Since our film has large aspect ratio (L/h), the flow of the film will be restricted to the lateral direction (x-axis). Hence, rewriting equation 2.3 along x-coordinate, explicitly yields

$$\rho\left(\frac{\partial u}{\partial t}\right) + \rho\left[u_x\frac{\partial u}{\partial x} + u_y\frac{\partial u}{\partial y} + u_z\frac{\partial u}{\partial z}\right] = -\frac{\partial p}{\partial x} + \eta\left(\frac{\partial^2 u}{\partial x^2} + \frac{\partial^2 u}{\partial y^2} + \frac{\partial^2 u}{\partial z^2}\right) + \rho g, \tag{2.4}$$

with the velocity vector expanded as $\mathbf{u} = \left(u_x, u_y, u_z\right)$.

### *2.3.2. The Lubrication Approximation*

By considering the fact that polymer melts have high viscosity, equation 2.4, further reduces to the lubrication approximation; a simplified version of the Navier-Stokes equation designed for use with thin films. More importantly, the velocity of polymer melt is considered to be small; because of the large viscous forces resulting from the small length scales in the problem. In this regard, the inertial terms of the Navier-Stokes equations can be neglected since they are proportional to $V^2/L$, where L is the characteristic length and $V$ is the characteristic velocity (small due to high viscous forces caused by small length scales) [86, 64]. Neglecting velocities in the y and z directions, equation 2.4 reduces to

$$\frac{\partial p}{\partial x} = \eta \frac{\partial^2 u(x,z,t)}{\partial z^2}. \tag{2.5}$$

### *2.3.3. Modeling of Curvature and Total Thickness*

Liquid surface almost never stays completely flat. The residual stress induced by the initial bending will have a wavelength of $\lambda$ and amplitude $\delta(t)$ as illustrated in Fig. 2.9. Therefore, the surface stress due to the bending curvature (see Fig. 2.10) can be defined as

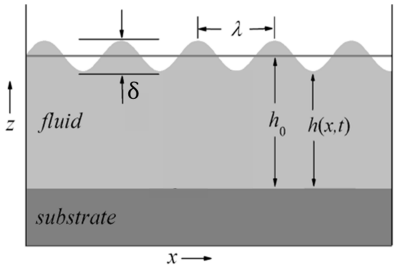


Figure 2.9. General schematics of a supported, fluidized polymer thin film of its initial thickness of $h_0$ and the new thickness, $h(x,t)$, which varies with the formed bump denoted by $\delta$ after the film is annealed above its glass transition temperature.The annealing temperature and the pressure due to bending induce capillary surface wave with a wavelength denoted by $\lambda$.

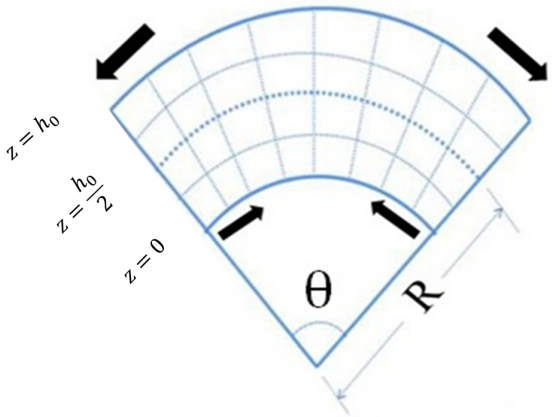


Figure 2.10. Illustration of the stress distribution of a thin plate under isometric deformations. In such deformations, the length of the plate along the center surface remains the same before and after deformation while the inner and outer edges are compressed and stretched, respectively.

$$p = p_0 \cos(kx) \tag{2.6}$$

with

$$p_0 = \frac{A}{\omega^2}\left(z - \frac{h_0}{2}\right)\bar{E}_f. \tag{2.7}$$

As a result of the perturbation due to the residual stress-coupled with thermal motion, the total thickness of the film (or the z-coordinate as a function of x and time) can be defined by

$$h(x,t) = h_0 + \delta(t)\cos(kx), \tag{2.8}$$

where $k = 2\pi/\omega$ is the wave vector of the undulation, $\delta(t)$ is the amplitude of the undulation of the perturbed film at the free surface. Two boundary conditions are considered. First, we assume that there is no slip-condition at the film-substrate interface. That is at the bottom of the film, where the fluid meets the solid, the velocity of the fluid film is zero. Secondly, we assume that there is no shear at the film-air interface (i.e. at the top surface of the fluid film the derivative of the horizontal velocity with respect to z is zero) [64, 58, 129]. In this case, we obtain the thin film horizontal velocity profile (along the x-direction) from equations 2.5, 2.6, 2.7, and 2.8 as

$$u = \frac{AkE_f}{\eta\lambda^2}\left(\frac{h_0 z^2}{4} - \frac{z^3}{6}\right)\sin(kx) \tag{2.9}$$

where $\eta$ is the viscosity of the flowing fluid film and $h_0$ is the initial film thickness. By conservation of volume, the amount of film material flowing along the x axis ($\Delta Q$) must be the same as the amount of the volume decrease in the perpendicular direction ($\Delta T$) (i.e. volumetric flow in the $x$ direction is equal to volumetric decrease in the $z$ direction). Mathematically, $\Delta Q = \Delta T$, where

$$\Delta Q = \int_0^{h(x)} u dz \tag{2.10}$$

and

$$\Delta T = -\frac{\partial h(x)}{\partial t} dx, \tag{2.11}$$

in [x, x+dx]). Integrating equation 2.10 yields,

$$\Delta Q = \frac{E_f A k h_0^4}{24 \eta \omega^2} \sin(kx). \tag{2.12}$$

Equating equations 2.11 and 2.12 results in

$$-\frac{\partial h(x,t)}{\partial t} = \frac{\partial (\Delta Q)}{\partial x}. \tag{2.13}$$

Finally, using equations 2.8 and 2.12 in equation 2.13 gives the bump height in terms of the material property, $\bar{E}_f$, as

$$\delta(t) \sim C\left(\frac{A}{\omega^4}\right), \tag{2.14}$$

where $A$ and $\omega$ are respectively the amplitude and width of the initial delamination. The parameters in $C = \left(\frac{t\bar{E}_f}{6\eta} h_0^4\right)$ with $h_0$ being the initial thickness of the film, $t$ the time the flowing film takes to totally equilibrated (no more flowing) when annealed above $T_g$, $\bar{E}_f$ the Yong's modulus of the film, and $\eta$ the viscosity of the flowing fluid film, are assumed to be fixed.

## 2.4. Results and Discussion

We have made significant progress in investigating the effect of locally bending and relaxing polystyrene thin films. As discussed earlier, under compression the film will typically first wrinkle and then form several delaminations whose profile can be measured as described in the previous sections. Each delamination has large amplitude at the sample

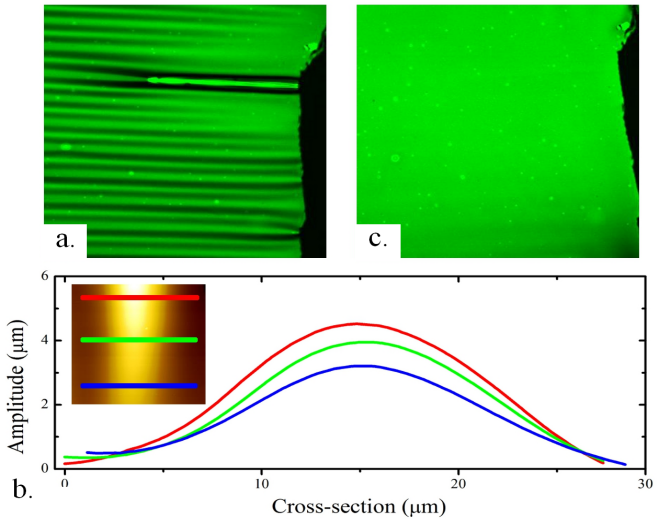


Figure 2.11. Pre-annealing experiment. a) confocal microscope image of wrinkles (low curvature) and a delamination (high curvature) near a sample edge. Scale bar indicates 32 $\mu$m. b) The same location after removal of stress - there is no observable change in the film. c) Cross sections through the delamination illustrating its variable amplitude (inset: an AFM micrograph of a segment of delamination).

edge, which slowly decreases as the delamination crest is followed orthogonally to the sample edge. Figure 2.11 illustrates results of the initial part of the experiment (pre-annealing experiment). It shows a typical confocal microscopy image of wrinkles (low curvature) and a delamination (high curvature) near a sample edge (see Fig. 2.11a). A cross section of a segment of the delamination of the film under compression is shown in Fig. 2.11b as obtained from AFM micrograph (see the inset). This figure clearly illustrates that both the amplitude and wavelength of the delamination vary as one moves away from the crack/sample edge of the film toward the tip of the delamination, implying that there is high residual stress near the crack edge. The same location is scanned after removal of stress. As indicated in Fig. 2.11c, there is no observable change in the film's topography suggesting that the film has remained in the elastic limit of deformation.

### *2.4.1. Formation of Bumps*

A closer look at the samples under investigation leads to the observation of slowly emerging bumps correlating to the initial delamination spot. This is possible by annealing the relaxed and now flat film above $T_g$ of its bulk. As a result of annealing, numerous thickened regions (called bumps and denoted by $\delta$, see Fig. 2.8b) emerge following the initial delamination spots. The results of this post-annealing experiment is shown in Fig. 2.12. The sample shown in Fig. 2.12a is the same sample shown in Fig. 2.11c after compressional stress is removed. The thermal annealing experiment is carried out by using a hot-stage (Linkam TMS94, Linkam Scientific Instrument, ltd) set to predetermined temperatures ranging from $165^oC$ to $200^oC$ depending on the specific thin film thickness under examination. In particular, we set the hot stage to a temperature of $165^oC$ for the film shown in Fig. 2.12a. In the course of annealing time of 15 to 30 minutes, the surface morphology of the film is closely monitored through out the experiment with Charge Coupled Device (CCD) camera mounted on an Olympus Microscope. Initially, the film surface is smooth and featureless. As the annealing time progresses, material begins building up at specific locations and measurable bumps start to gradually develop. After it has fully been annealed, the sample shown in Fig. 2.12a is transferred to silicon wafer for further imaging. Interestingly, the formed bumps (the localized brightest regions) are clearly observable and measurable by LSCM as illustrated in Fig. 2.12b and evidence to the flow of thin film. The bumps correlate with the locations of high curvature that occur when the sample is in the deformed state. The thickening can occur if and only if there exists flow of material from neighboring regions. The flow is dictated by the residual stress stored in the film due to the initial curvature of the delamination. Figure 2.12c shows a segment of an AFM image of the resulting bump structure along with the cross sectional measurement indicating the variation of the height and width of the bump formed. Again, we note that the variation of the bump height and

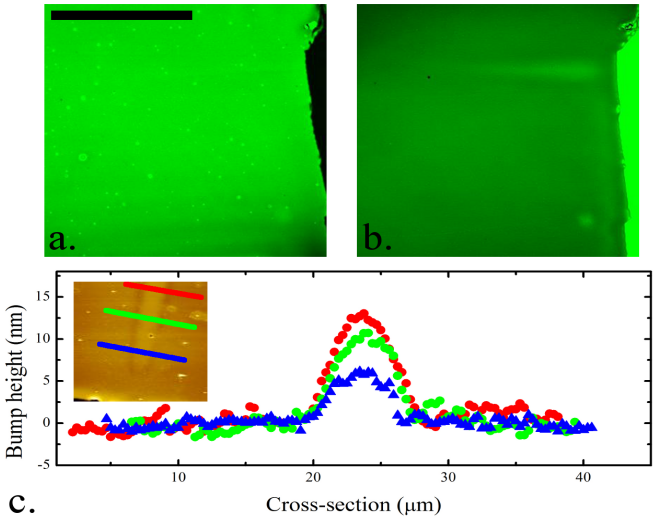


Figure 2.12. Post-annealing experiment. a) the same film shown in Fig. 2.11 after compression. Scale bar indicates 32 $\mu$m. b) After annealing at 140°C for approximately 10 minutes. The sample has been transferred to silicon for imaging. c) AFM of the resulting structure.

width follow the same pattern as its preceding delamination.

### *2.4.2. Evolution of the Bump Amplitude*

The thickness inhomogeneity described earlier will not take place instantaneously. It takes a finite time for the material to flow. In order to characterize its time dependence, the following procedures are followed. First, a sample in a mechanically relaxed state (with initial film thickness of 299 nm), is loaded on a hot stage and annealed to a temperature of 60°C and allowed to equilibrate under observation by confocal microscope ($\sim$ 10 min). At this point, the surface temperature of the sample remains somewhere below the bulk $T_g$ of the sample as 60°C is much lower than the $T_g$ of the bulk polystyrene (note that the glass transition temperature of glassy bulk polystyrene is $\sim$ 100°C) [105]. Next, the temperature is raised above $T_g$ to 140°C with a rate of 50 deg/min in order to allow the film to flow. The film is repeatedly imaged under illumination of a wavelength of 405

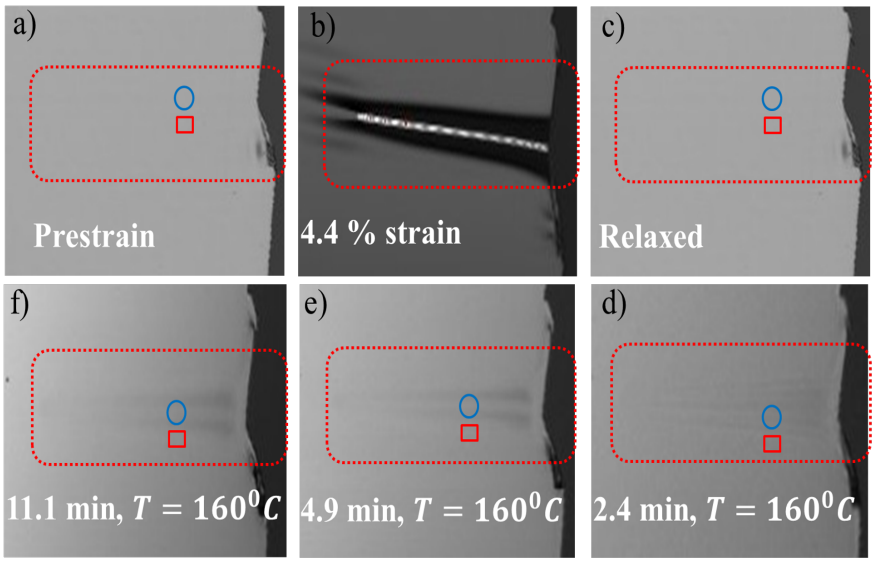


Figure 2.13. This figure illustrates time evolution of the bump formation. a) Prestrain (b) 4.4% copressive strain, c) Relaxed state at room temperature, d) Annealed for 2.4 min at $160^{\circ}C$, e) Annealed for 5.1 min at $160^{\circ}C$ and f) Annealed for 11.1 min at $160^{\circ}C$.

nm for the next 30 min. The typical representative response of this annealing is shown in Fig. 2.13. Finally, the ratio of intensities of a laser reflected from center of the bump and from the non-deformed film surface have been measured and plotted as a function of time (see Fig. 2.14). This ratio is related directly to the films thickness because of thin film interference. Initially, the thickness inhomogeneity is not observed as evidenced by a uniform light intensity. As annealing progresses, the bump starts forming and the ratio of intensities gradually deviates from one. Eventually, the flow ceases, the bump reaches its maximum height, and the intensity ratio no longer changes. The data is well described by defining an exponential function $f(t) = A \times Exp(-t/\tau) + B$. The best fit to the data is obtained for $A = 0.06$ and $B = 0.98$ which gives a relaxation time of $\tau = 2.33$ min.

### *2.4.3. Correlation Between Curvature and Bump Height*

Figure 2.15 shows the curvature and bump height as a function of distance from the crack/sample edge, illustrating the high degree of correlation between the two variables,

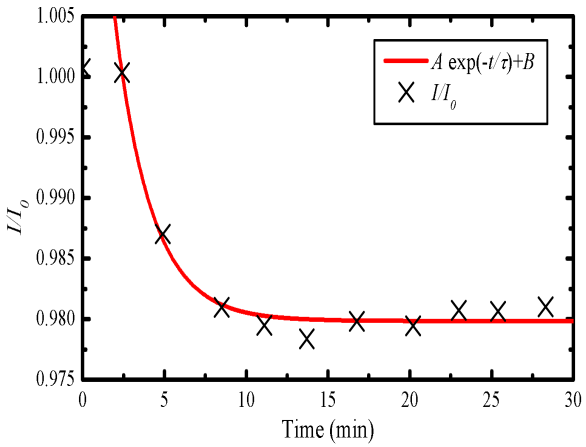


Figure 2.14. Time evolution and growth of the bump height. This figure illustrates the ratio of the intensities of monochromatic laser reflected from center of the bump and from the non-deformed film surface. Initially, the thickness inhomogeneity is not observed as evidenced by a uniform light intensity. As annealing progresses, the bump starts forming and the ratio of intensities gradually deviates from 1 and $\delta$ reaches maximum and the ratio of intensities no longer change. The solid line is a curve fitting which gives a relaxation time of $\tau$ = 2.23 min with A = 0.06 and B = 0.98.

curvature and bump height. The correlation between the curvature at the peak of the delamination and $\delta$, the height of the thickened region, is evident upon comparison of the topography along the long axis of the feature, as shown in Fig. 2.15 ($\kappa$ indicates curvature). As the width of the delamination is approximately equal to the intrinsic spacing of the wrinkling instability which precedes it, the decreasing amplitude means that the curvature at the delamination's peak is also decreasing away from the sample edge. Similar experiments were conducted with films of different thicknesses and the correlation between the bump height and curvature is shown as in Fig. 2.16. Although they do not collapse onto a master curve, the data show linear correlation for each thicknesses.

### *2.4.4. Onset of Plastic Deformation*

In the previous subsection, we have shown that there is a strong correlation between peak curvature of a film under compression and the corresponding bump height formed after the sample is transferred to a silicon substrate. This correlation was investigated by

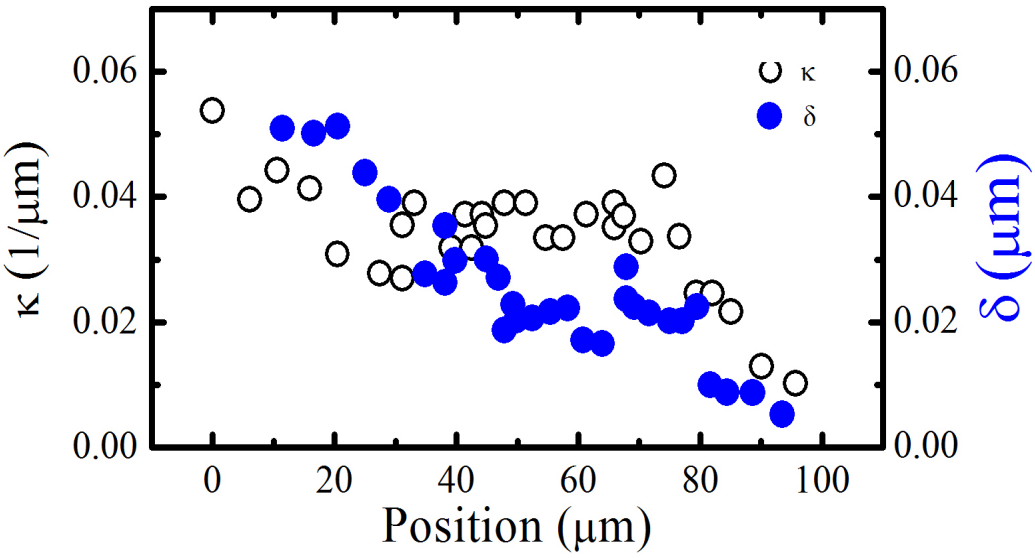


Figure 2.15. Curvature and bump height as a function of position, illustrating the high degree of correlation between the two variables: bending curvature is indeed the cause for the formation of the thickness variation in the film.

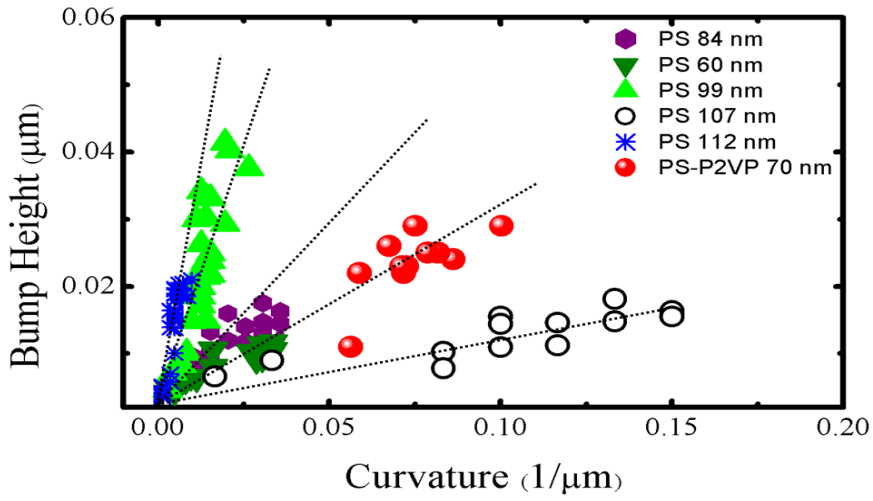


Figure 2.16. Correlation between bump height and curvature for a number of PS film thicknesses and a symmetric block copolymer(Red).This correlation has an implication that the bump height is thickness dependent. Also, note that the data with unfilled circles was obtained on a stiffer substrate.

considering the complete topographies along the long axes of delaminations and the bumps formed. To make the measurement more quantitative, we now switch from considering the complete topography to considering only the critical point of the onset of plastic deformation (the yield strain). The critical point is taken at the strain localization where damage is no longer visible. This change significantly reduces measurement error because the focus is now a measurement of a large length scale (the distance from $\delta = 0$ to the sample edge, $\sim 40$ $\mu$m see Fig. 2.18). To locate where the critical strain occurs, the micrograph of a post annealed sample is taken. Then a line is drawn across the formed bump starting from the crack edge until crossing the tip of the bump. This yields intensity versus distance from the crack edge. Similarly, another intensity versus distance is generated from an undeformed region (see the solid line in Fig. 2.18)(a). Here, since the thickness of the film remains uniform, the intensity does not change. Plotting the two intensities versus distance data together clearly show where the critical point occurs on the post-annealing micrograph. This is shown by the merging of the intensity line beyond the critical point (see Fig. 2.17).

In order to quantify the magnitude of the critical strain, the image of the sample taken when the sample was under compression is also required to first determine the curvature corresponding to the critical point. Once the critical point is determined from the intensity graph, using IMAGEJ (a free NIH software) (see Fig. 2.18(a)), that spot must be mapped onto the delamination as shown in Fig. 2.18(b) (here, it is worth mentioning that extra care must be considered in using appropriate microscope conversion factors when measuring the lengths if the two samples are not captured by identical microscope lenses). This will help to obtain the curvature of the sample under compression at the specific spot. Knowing the curvature and the thickness of the film yield the critical strain for a particular film. Our measurements, in this regard, yield several observations. For example, the onset of plasticity measured for thin polystyrene film shown in Fig. 2.11 yields $\varepsilon_p$ in

the order of 0.1%, an order of magnitude smaller than the bulk value reported in literature for bulk polystyrene [1, 65, 49]. In addition to the small value of the critical strain, our measurements show that *critical strain increases* for film thickness less than $\sim$ 100 nm as illustrated in Fig 2.19 for various film thicknesses.

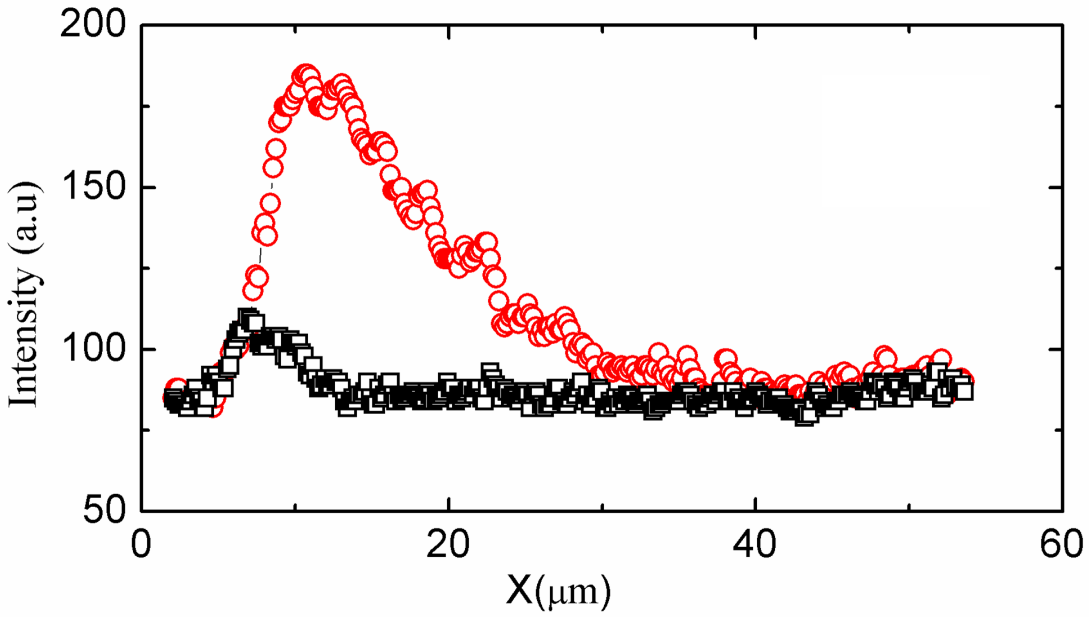


Figure 2.17. Method of precisely locating where the critical strain takes place on optical micrograph. This was possible by obtaining the variation of intensity along the bump and a certain distance away parallel to the bump. As one moves away from the crack edge along the bump, the intensity decreases gradually while the intensity taken from a line parallel to the bump remains the same; because there is no thickness change along that line. At the critical point the two intensities merge together (see Fig. 2.18). The red is from the bump whereas the black is from the undeformed region.

Several anomalous measurements (such as markedly reduced elastic modulus compared to the corresponding bulk material, reduction of glass transition temperature, reduction of the inter-chain entanglement density) have been reported for polymer thin films of thickness less than $\sim$ 100 nm as described in the beginning of the chapter [60, 34, 85, 95, 10, 78, 70, 97]. The change we observe here as the film thickness drops below $\sim$ 100 nm could be related to a reduction of inter-chain entanglements [14, 106], or to a change in the glass transition temperature of the film [60, 36, 34, 95, 85, 11].

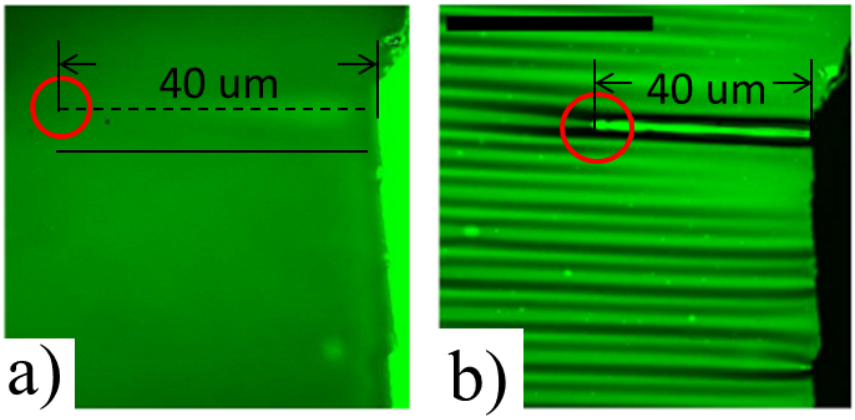


Figure 2.18. Method of mapping the location where the critical strain takes place on a) optical micrograph to b) laser scanning confocal microscopy image. The (a) image is captured in the post-anneling stage whereas the (b) is captured while the sample is under compression. The broken line on the (a) corresponds to where the intensity across the bump is taken from whereas the solid line refers to where the intensities are taken from (the undeformed area).

Bending gives the opportunity to make a clear distinction between the two possibilities (i.e. reduction of the glass transition temperature and reduction of the inter-chain entanglement density). This is because bending preferentially probes a film's free surface and the applied strains can be accurately measured in the vanishingly small strain limit. Small strain ensures that the network of polymer chains is not deformed significantly, and therefore the entanglements themselves cannot play a large role in the overall effect (this is not common in most failure measurements [106, 70]). As evidence for our contention, we duplicate the experiment with PS films of an order of magnitude larger molecular weight. Fig. 2.19 shows no observable effect of molecular weight on the location or magnitude of the upturn. We conclude that the critical strain for the onset of plastic deformation must then be related to the same mechanism behind reductions in the glass transition. While suggested by the simulations of B*ö*hme and de Pablo [11], a relationship between the glass transition depression and plasticity has not yet been fully examined. Qualitatively, the glass transition is reduced due to a region of increased mobility near the free surface of the polymer film (operating over a length scale of ($\sim 10nm$). In this region, a larger strain is

needed before stress can be stored as stress can more easily relax away. A trivial layered model, similar to that has been described in section 2.1.3 for thermal expansion coefficient of polymer films, can be written as

$$\varepsilon_p(h) = (l/h)(\varepsilon_p - \varepsilon_p^\circ) + \varepsilon_p^\circ \tag{2.15}$$

where $l$ is the size of the soft layer and $\varepsilon_p$, $\varepsilon^\circ$ refer to the surface strain of the liquid-like layer and bulk (remaining part of the film) strain respectively. A fit to our data in Fig. 2.19, assuming a typical lengthscale $l = 10$ nm, gives $\varepsilon_p = .017 \pm 0.002$ and $\varepsilon_p^\circ = 0$ $.001 \pm 0.001$. We measure the critical surface strain for stress storage in polystyrene films to be in the order of $10^{-3}$, which is notably below strains at which yielding is noted in bulk polystyrene [11, 74]. We will repeat similar measurement with a spin-cast polystyrene-b-poly (2 vinyl pyridine) block copolymer film in order to show the versatility of our technique (see chapter 3 below). This implies that we are measuring a material specific property as expected for a yield point. However, it must be realized that this material specific property changes as the film thickness goes below a 100nm as can be seen in figure 2.19. In other words, the critical strain becomes a function of film thickness for PS films below a thickness of approximately 100nm.

### *2.4.5. The Model*

The simple scaling model described in section 2.3 demonstrates the flow of thin film after after the film has been annealed above its glass transition temperature. It shows a qualitative description of the flow of the fluidized film and makes predictions with respect to the scale of the thickening (bump height) in the PS film. The data of Fig. 2.16 can be rescaled by equation 2.14 as illustrated in Fig. 2.20. Although the scaling expression has large exponents, the qualitative collapse of the data is remarkable and AFM measurements

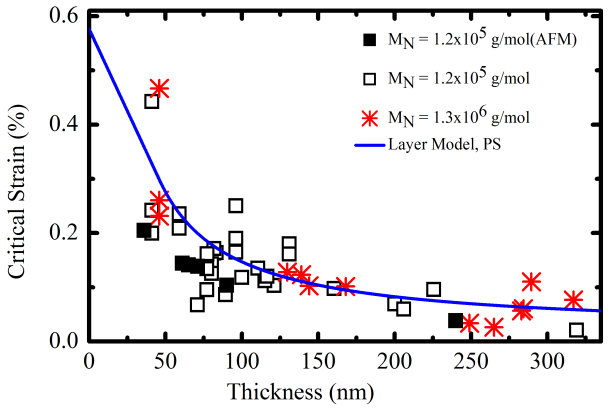


Figure 2.19. The figure shows variation of critical strain of PS films as a function of film thickness. The data were gathered from two molecular weights differing by an order of magnitude. Although molecules differing by an order of magnitude are considered, there is no significant difference observed. This has an implication that the increment of the yield strain as film thickness decreases below $\sim$ 100nm is not related to the reduction of inter-chain entanglement density. The solid line is a fit to the layer model.

of the thickening are consistent with this simple theory, backing up our primary conclusion: bending causes stress storage in thin PS films.

## 2.5. Summary

In this chapter, we developed a novel technique of characterizing threshold strain for nanoscale polymer films. Using this unique method, we demonstrated that the onset of plastic deformation for thin polystyrene films is an order of magnitude smaller than what has been reported for the bulk value. Furthermore, the onset of failure strain $\varepsilon_p$ is in the order of 0.1%. In addition to the small value of the critical surface strain, our measurements show that *critical strain increases* for film thickness less than $\sim$ 100 nm. Similar to several anomalous measurements (such as markedly reduced elastic modulus compared to the corresponding bulk material, reduction of glass transition temperature, reduction of the inter-chain entanglement density) that have been reported for polymer thin films of thickness less than $\sim$ 100 nm, our measurement also show that the variation

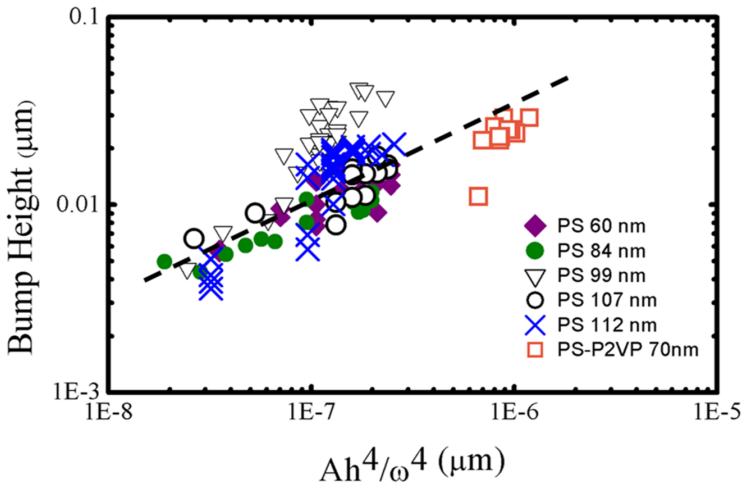


Figure 2.20. This figure illustrates scaling plot of bump height by equation 2.14 as a function of the control parameters for a number of PS film thicknesses and a symmetric block copolymer (Orange) indicated in Fig. 2.16. Although the scaling expression has large exponents, the qualitative collapse of the data is remarkable.

of yield strain is pronounced when the thickness reaches below $\sim$ 100 nm. Our initial hypothesis was that the change we observe could be related to a reduction of inter-chain entanglements, or to a change in the glass transition temperature of the film. Through our experiment, however, we not only clearly demonstrated that the reduction of inter-chain entanglement density is not contributing to the increment of the yield strain as the film confinement is increased, but also verified that the onset of plastic deformation could be related to the same mechanism behind reductions in the glass transition.

We have also showed a simple scaling model that describes the flow of thin film after annealing above its glass transition temperature. The model shows a qualitative description of the flow of the fluidized film and makes predictions with respect to the scale of the thickening (bump height) in the PS film. Although the scaling expression has large exponents, the qualitative collapse of the data is remarkable. Furthermore, the atomic force microscopy measurements of the thickening are consistent with this simple theory, backing up our primary conclusion: bending causes stress storage in thin PS films.

# 3. EFFECT OF NANOSTRUCTURAL ORDERS OF DIBLOCK COPOLYMER FILMS ON YIELD STRAIN

## 3.1. Background

The previous chapter was devoted to exploring the qualitative estimation of the onset of plasticity in nanoscale polystyrene films. Motivated by the significant observations presented in the previous chapter coupled with the goal of investigating more complex thin film materials, the mechanical response of thin films made from diblock copolymers was explored. Diblock copolymer is a polymer made from two blocks of homopolymers connected by covalent bonds. In the past, significant attention was given to the study of block copolymers due to their ability to phase separate (self-assemble) into well ordered nanometer scale structures [5, 6, 47, 48, 103]. The easy assemble of nanostructure put block copolymers at the forefront of potential applications in technologies ranging from lithography to high density storage devices. In order to realize these emerging applications, the mechanical properties and the underlying physics of block copolymers need to be understood.

Over the last several decades, the mechanical behavior of *bulk* block copolymers such as crazing and fracture have been extensively studied both experimentally [121, 101] and theoretically [76]. Unlike in homopolymers, these behaviors depend highly upon the response of the constituent blocks. Most importantly, the difference in mechanical properties [76], chain orientations relative to applied stress in a nanoscale self-assembled structure [50], degree of incompatibility [51] of the blocks can significantly change the materials' response. For example, by using a molecular dynamics simulation model,

[0]Andrew Croll and Bekele Gurmessa designed and conducted the experiment in this chapter in close cooperation. The work in this chapter is submitted to macromolecules for publication.

Makke et al. [76] concluded that large buckling deformation is first accommodated by the softer layer, when a layered (stack of soft and hard layers of) copolymer (rubber-glassy) is subjected to a tensile stress whereas the hard, glassy layer resists bending. Similarly, it has been shown experimentally that crazing processes are confined to a single microdomain (rubber domain) in the rubber-glassy bulk copolymers (e.g. polystyrene-b-polybutadiene) [121]. Lee and his colleagues have extended this concept to thin films and studied the effect of lamellar microstructural order of poly(styrene-b-2-vinylpyridine) on the crazing process [71]. They concluded that lamellar microstructure in self-assembled poly(styrene-b-2-vinylpyridine) thin films results in slower craze growth rate.

Although, the mechanical properties of bulk copolymers are studied extensively, there is still little known about the mechanical response of these materials in the limit of nanoscale thickness. Specifically, the response of microphase separated block copolymer thin films to mechanical deformation is still lacking. In this chapter, an experimental investigation of the effect of microstructural order of diblock copolymers on the onset of damage will be presented. The chapter begins with a brief review of thermodynamics of polymer phase separation in both bulk and confined materials followed by the experimental procedures used, the results found and discussion.

### *3.1.1. Phase Behavior in Diblock Copolymers*

The phase state of a given system is usually described by a balance between enthalpic (defined as $H = U + PV$, where U, P, and V stand for the systems internal energy, pressure and volume, respectively) and entropic contributions that together make up the Gibbs free energy, G, of the system written as $G = H - TS$ [5] with $S$ and $T$ being the entropy and temperature of the system. Phase separation between two species takes place when the magnitude of the enthalpic contribution to the free energy of mixing exceeds the magnitude of the entropic contribution. For example, in a blend of two

homopolymers A and B, the phase behavior is governed by the relative lengths of each block (degree of polymerization N), the composition volume fraction), $f$, and A-B Florry-Huggins interaction parameter, $\chi$. According to the Florry-Huggins formulation, the change in free energy ($\Delta G$) per segment (monomer) associated with mixing homopolymers on an incompressible lattice ($f_A + f_B = 1$) is approximated as

$$\frac{\Delta G}{k_B T} = \frac{1}{N_A} \ln f_A + \frac{1}{N_B} \ln f_B + f_A f_B \chi_{AB} \tag{3.1}$$

where $k_B$ is the Boltzmann constant, T is the temperature, $f_A = N_A/(N_A + N_B)$ and $f_B = N_B/(N_A + N_B)$ are the volume fractions of polymer A and B respectively. $N_A$ and $N_B$ are the degree of polymerization of chain A and B. The first two terms in equation 3.1 have entropic origin which always promote mixing because mixing always increases system randomness. These terms are usually controlled by changing the overall size of the polymer chains and the fractions of the chains A and B during polymerization [4]. The last term in equation 3.1 corresponds to the enthalpy of mixing (has energetic origin), which can increase or decrease $\Delta G$ depending on the sign of $\chi_{AB}$. The Flory-Huggins interaction parameter, $\chi_{AB}$, is a dimensionless parameter defined to characterize the differences in interaction energies between the blocks of an A-B diblock copolymer. Mathematically, it is defined as

$$\chi_{AB} \equiv \frac{z}{k_B T} \left( \varepsilon_{AB} - \frac{\varepsilon_{AA} + \varepsilon_{BB}}{2} \right), \tag{3.2}$$

where $\varepsilon_{AA}, \varepsilon_{BB}$ and $\varepsilon_{AB}$ are the interaction energies of the $A-A, B-B$ and $A-B$ contacts of the blocks, $z$ is a coordination number of a given lattice (the number of nearest neighbor monomers to a copolymer configuration cell). In the vast majority of cases, $\chi_{AB}$ is positive. Positive $\chi_{AB}$ indicates repulsion between the A and B monomers whereas a negative value signifies mixing of unlike monomers (in which case single phase mixture is favorable). Moreover, $\chi_{AB}$ usually varies inversely with temperature. Empirically, the Florry-Huggins

parameter is associated with the A-B monomer interactions and generally decreases with temperature [111, 99] as

$$\chi_{AB} \cong a + \frac{b}{T}. \tag{3.3}$$

The constants $a$ (referred to as the entropic part of $\chi_{AB}$) and $b$ (b/T is called the enthalpic part of $\chi_{AB}$) are unique for different blends and are experimentally obtained.

As with any system at equilibrium, the diblock copolymer chains will be arranged such that their free energy will be minimized. This free energy configuration can be disturbed by increasing $\chi_{AB}$ (this is often accomplished by reducing temperature). Consequently, the chains segregate into distinct phases. Unlike phase separation of mixtures of homopolymers, block copolymers are known to self-assemble into varieties of micro-phase separated morphologies such as spheres, hexagonally packed cylinders, lamellae, and bicontinuous 'gyroid' structures as shown in Fig. 3.1(a) [5, 111]. Micro-phase separation is a phenomenon similar to that of immiscible blends of homopolymers. Unlike homopolymers, the blocks cannot demix macroscopically as the two blocks are covalently bonded to one another. In essence, the bond highly reduces the entropic contribution by prohibiting the monomer units from independently occupying the entire space. Hence, in microphase separation each block forms nanometer-sized domains. It has been well documented that, the sizes of the domains formed and their morphologies are determined by the relative lengths of each block (degree of polymerization, $N_A$ and/or $N_B$) and the composition, ($f_A$ and/or $f_B$) [5, 77, 111]. For example, highly different block lengths form spheres of nanometer size of the first block in a matrix of the second. When the length of the blocks becomes more of symmetric, a hexagonally packed cylinder will be formed. Furthermore, blocks of similar lengths form alternating layers of one block after the other (often called lamellae) [6, 47]. On the other hand, the ordered phases can be disordered by rising the entropy of the system, for example, by reducing $\chi_{AB}$ or the degree of polymerization, N. Since the entropic component $\sim N^{-1}$ and the enthalpic component is

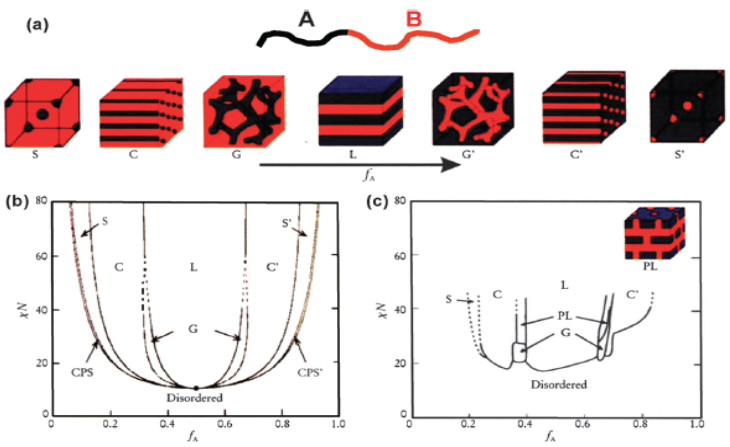


Figure 3.1. Phase behavior of AB diblock copolymer: a) Example of a linear AB diblock copolymer and the equilibrium morphologies in the bulk: spheres (S), cylinders (C), bicontinuous gyroids (G), and lamellae (L). b) Theoretical phase-diagram of AB diblocks predicted by self consistent mean-field theory depending on the volume fraction ($f$) of the blocks and the segregation parameter, $\chi_{AB}$N. c) Experimental phase-digram of poly(styrene-block-isoprene) (PS-PI) copolymers, in which $f_A$ represents the volume fraction of polyisoprene, PL denotes perforated lamellae. "Reproduced with permission from ref. [5]. Copyright (1991), American Institute of Physics."

$\sim \chi_{AB}$ (see equation 3.1), the product $\chi_{AB}N$ is the quantity that dictates the phase behavior of block copolymer.

### *3.1.2. Phase Diagram of Diblock Copolymers*

A number of researchers have reported the phase behavior of bulk block copolymers in both theory [4, 72] and experiment [4, 77] by plotting the segregation product, $\chi_{AB}N$, versus the composition of the copolymers. Often times, the product $\chi_{AB}N$, that expresses the entropic-enthalpic balance, is used along with the composition of block copolymers to parametrize the block copolymer phase behavior. For example, let's consider the theoretical (Fig. 3.1(b)) and experimental (Fig. 3.1 (c)) phase diagram of poly(styrene-isoprene) (PS-PI) demonstrated by Bates and co-authors [5].

*3.1.2.1. Theoretical*

In both theories and experiments dealing with the phase behavior of block copolymers, there are two segregation limits considered in terms of $\chi_{AB}$N: strong segregation and weak segregation limits. Since there are no well-defined criteria for separating these regimes, they are mostly discussed in vague terms; the earlier one corresponds to a regime where $\chi_{AB}$N > 100 while the latter one corresponds to $\chi_{AB}$N ∼10 - the critical segregation limit for symmetric diblock copolymers as estimated by Mark. et al [77]. It has been shown that $R_g \sim N^{1/2}$ in the limit of $\chi N \ll 10$ implying that chain stretching is negligible and hence the chain statistics (confirmation) takes the unperturbed Gaussian distribution, $R_g \sim N^{1/2}$. On the other hand, $R_g \sim N^{2/3}$ in the strong segregation limit. At such a transition, the amplitude of the lamellar pattern grows continuously from zero on lowering the temperature [77].

Theoretically, the phase diagram of block copolymer spanning these two segregation limits can be obtained by self-consistent mean field theory as shown in Fig. 3.1b [5, 48, 77]. The diagram indicates two fundamental transitions: order-to-order transitions and order-to-disorder transitions. In one hand, increasing the composition of the volume fraction of block $A$ to block $B$ from 0 to 1 in the strong segregation limit at a fixed $\chi_{AB}$N, the order-to-order transition begins from closely packed spheres (CPS), which comes immediately after the disordered state, and passes through body-centered cubic spheres (S) followed by hexagonally packed cylinders (C), bicontinuous gyroids (G) (which becomes unstable as the segregation product increases as can be seen from the diagram) and lamellae (L) phase (with alternating layers of the constituent blocks). It is also worth noting that as we move from left to right on the phase diagram of the block copolymers, the composition of the volume fraction of $B$ reduces while that of $A$ increases. In such cases, there exist inversion of morphologies from $B$ dominant to $A$ dominant as can be noted from the equilibrium morphologies of Fig. 3.1(a) where S, C and G are replaced by S', C' and G'. On the

other hand, with decreasing $\chi_{AB}$N (this is possible by increasing temperature) at a particular composition the entropic contribution which always favors mixing, increases implying that the incompatibility between each block decreases. As a result, the copolymers show order-to-disorder transition (ODT) and become homogeneously mixed (disordered). There is a particular transition temperature at which the order-to-disorder transition takes place. This particular temperature is often termed as $T_{ODT}$ [77]. For example, on the segregation limit versus composition phase diagram shown Fig. 3.1, ODT takes place at $\chi N = 10.5$ for the theoretical diagram and $\chi N \sim 18.5$ for the experimental prediction, although these values vary with the polymer size.

#### *3.1.2.2. Experimental*

The experimental study of the phase behavior demands annealing of the sample above its glass transition temperature ($T_g$) for a predefined time followed by rapid quenching below $T_g$. During annealing the polymer structure is controlled by thermodynamics. When the sample is quenched, the polymer structure is found to be kinetically frozen (becomes immobile) due to the extremely low mobility of the chains. The morphology observed after rapid quenching, captures the essential features of the material at the higher annealing temperature. Figure 3.1(c) shows the experimental phase diagram of polyisoprene-block-polystyrene copolymers (Bates and coworkers) [77]. This experimental phase diagram shows a qualitative similarity with the theoretical diagram shown in Fig. 3.1(b).

The block copolymer phase diagram is constructed experimentally by first determining the temperature dependent $\chi_{AB}$ through measuring the ODT for a series of polymers. At ODT, the dynamic shear elastic modulus (G') is found to drop dramatically during the heating process. Once the ODT is determined, the microstructures are mostly

characterized through the combinations of small angle x-ray scattering (SAXS), small angle neutron scattering (SANS) and transmission electron microscopy (TEM) [48, 77].

### *3.1.3. Confinement In Diblock Copolymers*

Unlike in the bulk, where polymer chains exhibit a typical random Gaussian orientation, polymer chains (whether co/homopolymer) - although not ordered - show a stretched configuration beyond the Gaussian chains in the as-cast and confined geometry. This chain stretching is attributed to considerable hydrodynamic shearing effect that occurs at the interface of film and substrate and solvent swelling during spin-casting [79]. However, other than chain stretching, the overall distribution is homogeneous as illustrated schematically in the blow up of Fig. 3.2(a).

When annealed, block copolymers undergo microphase separation and self-assemble into nanoscale morphologies with a well defined periodicities in both bulk and thin film geometries. As pointed out in the previous section, the phase behavior of bulk block copolymer is dictated by three main factors: the interaction between monomers, $\chi_{AB}$, the degree of polymerization, N, and the relative composition of block A and B, $f_{AB}$ [5, 103]. In addition to these factors, constraints such as commensurability between the periods of the block copolymer (i.e. the relationship between the repeat period of the copolymer to the over all thickness of the film) and the film thickness, the tendency of specific blocks to go to one of the two interfaces preferentially (i.e. interfacial interaction between both blocks and the substrate) play huge roles on the morphologies in block copolymer thin films [122, 100]. In this perspectives, there are two possible wetting conditions: symmetric and antisymmetric wetting. The former refers to a situation where an identical block (say block A or B but not both) wets both substrate/air interfaces whereas the later refers to another situation where different blocks preferentially interact with one of the interfaces. When equilibrium is reached, nanodomains, which may be symmetric

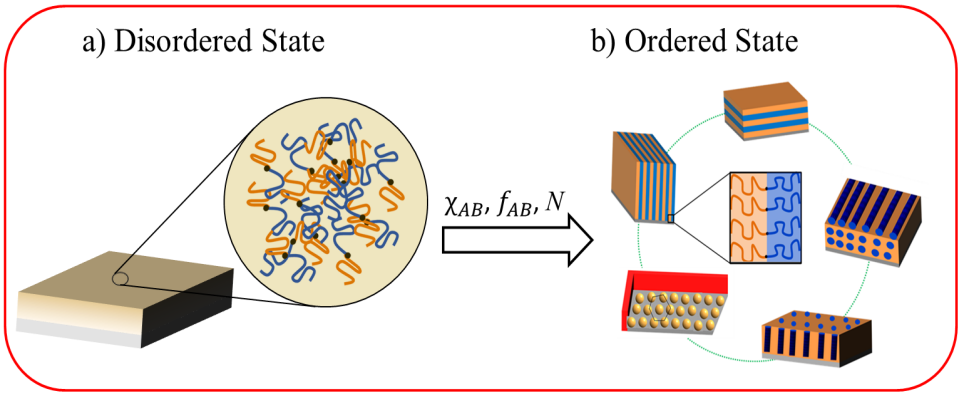


Figure 3.2. Schematics of the structural orientation of a diblock copolymer in a confined geometry. a) The as-cast thin film shows homogeneously mixed (disordered) chains orientation. b) Controlling $\chi_{AB}$, $f_{AB}$ and $N$ help the chains self-assemble into a variety of nanodomains. Furthermore, the presence of the boundaries (air/substrate) make the nanodomains align in a particular orientation to the substrate surface such as lamella parallel or perpendicular, cylinders parallel or perpendicular, hexagonally packed spheres.

or asymmetric, are formed with a particular orientation relative to the substrate plane. For example, lamella parallel or perpendicular, cylinders parallel or perpendicular, hexagonally packed spheres are formed as illustrated in the schematics of Fig. 3.2(b). If the film thickness and the step height, $L_0$ are commensurable, the total film thickness, h, becomes

$$h = \begin{cases} nL_0, & \text{symmetric wetting} \\ (n+1/2)L_0, & \text{antisymmetric wetting} \end{cases}$$

where n = 1, 2, 3, .... When these conditions are met, smooth or flat films of thickness $h = (n+1/2)L_0$ or $h = nL_0$ are observed. If the periods of the block copolymer and the film thickness are incommensurate, then the surface of the film becomes unstable and is decorated by terraces ( islands and/or holes with step height or depth of $L_0$) [6, 100, 127].

In this chapter, we study the effect of lamellar and cylindrical microstructures on the plastic deformation of diblock copolymer thin films. In order to understand how these ordered microdomains affect the onset of plasticity, we make use of thin films made

from symmetric polystyrene-b-poly(2-vinylpyridine) (PS-*P*2VP) as a model material. This polymer was chosen due to similarities in the mechanical properties (such as glass transition temperature, entanglement molecular weight, and elastic modulus) of the two blocks - polystyrene and poly(2-vinylpyridine). Previous studies have shown that reducing the thickness of a polymer film to nanoscopic dimensions results in the changes to the glass transition temperature [60, 34, 36, 85, 95, 10, 78], reduction in the number of entanglements between chains [14, 106], and changes in the mechanical properties (such as crazing, shear yielding) [71, 22] of the film. Remarkably, few studies have considered how failure processes might be altered in thin films, or how plasticity might alter a film's response to other stimuli. Therefore, it is important to understand how the yield strain in a thin film with microstructural domains compares with both disorganized diblock copolymers as well as the individual blocks in homopolymer form. In this regard, an elastic instability-discussed in the previous chapters- will be exploited again to locally bend and impose a *local* tensile stress in thin PS-b-*P*2VP films and directly measure the resulting residual stress caused by the bending. Direct measurements of the damage caused by the bending leads to the identification of a critical strain for plasticity.

## 3.2. Experimental Procedures

Most of the procedures used in the current chapter will be the same as the ones described in the previous chapter. The mechanism of inducing stress, measurement methods and tools, were explained in chapter two and will not be repeated here. Therefore, in this section we provide only the additional procedures needed to complement the previous ones; starting with the description of our model material and sample preparation, followed by results and relevant discussions, and a summary of the main observation of the current project.

### *3.2.1. Materials*

Monodisperse, symmetric and asymmetric polystyrene-b-poly(2-vinylpyridine) (PS-b-P2VP) were purchased from Polymer Source Inc. and used as received. The symmetric PS-b-P2VP has a PS block of molecular weight $M_n$ = 40 kg/mol and a P2VP block of $M_n$ = 40.5 kg/mol. The polydispersity index (PDI) of the diblock is 1.02. The second molecule considered was a cylinder forming PS-b-2VP with PS block of $M_n$ = 56 kg/mol and a P2VP block of $M_n$= 21 kg/mol, and has PDI of 1.06. The two molecules were chosen to have differing microphases but similar total molecular weight. In addition, polystyrene homopolymer of molecular weights $M_n$ = 1.3Mg/mol and $M_n$ = 1.2kg/mol with PDI of 1.15 and 1.04 respectively and Poly(2-vinylepyridine) (P2VP) homopolymer of molecular weight $M_n$ = 135kg/mol and PDI of 1.06, also purchased from polymer source Inc., were used in the experiment as summarized in table 3.1.

Table 3.1. List of the molecular details of the polymers used in this chapter. The numbers following the sample names (e.g. PS-1) are added just to easily distinguish the samples with the same names but different $M_w$, $M_N$ and PDI.

| Samples | $M_N$ (kg/mol) PS | $M_N$ (kg/mol) P2VP | PDI |
|---|---|---|---|
| PS-1 | 1100 | - | 1.15 |
| PS-2 | 115 | - | 1.04 |
| P2VP | - | 135 | 1.06 |
| PS-b-P2VP-1 | 40.5 | 40.0 | 1.10 |
| PS-b-P2VP-2 | 56 | 21 | 1.06 |

### *3.2.2. Substrate and Film Preparation*

We use 3 mm $\times$ 12 mm $\times$ 70 mm substrates of cross linked polydimethylsiloxane (PDMS). Curing agent and PDMS prepolymer (Dow chemical Corning, Sylgard 184) are thoroughly mixed in a 1:20 weight ratio, respectively. After degassing, the polymer mixture

is poured into a petri dish, cured at 85 $^{\circ}$C for two hours and then left in vacuum oven for the next 12-15 hours.

A series of polymers listed in table 3.1 were dissolved in toluene (Anhydrous 99.8%, Sigma-Aldrich Inc.) in concentrations ranging from 0.5% - 3% by weight. Then the solution of polymer/toluene was filtered through a micro-pore system (pore size 0.482 $\mu$m, Cadence Science Inc.) and spin coated at variable speeds ranging from 500rpm - 3000rpm onto a freshly cleaved mica substrate bound to a glass slide.Varying the concentration of the solution and speed of rotation help to vary the thicknesses of the films.

For the PS-b-P2VP, two sets of films are made. The first set is used as spin coated (which are in a disordered state) whereas the second set undergo additional steps of annealing to enable self-assemble. In order to initiate the self-assembly process, samples were annealed at temperatures ranging from (165$^{\circ}$C - 185$^{\circ}$C) all well above the glass transition temperature of the bulk PS-b-P2VP ($\sim$ 100$^{\circ}$C). The second set is called the ordered set. Finally, both series are transferred to a clean deionized water surface (Milli-Q) and subsequently become ready for the next procedure (the mechanics step). In all cases, the films are imaged with Laser Scanning Confocal Microscopy (LSCM - Olympus Fluoview 1000) or with Atomic Force Microscopy (AFM - DI Dimension 2100).

### *3.2.3. Thickness Measurement*

Film thickness is one of the dominant geometric properties related to bending and must be measured carefully. Atomic Force Microscopy (AFM - DI Dimension 2100) is used to image and locally measure a film thickness. The as-cast and flat surface films present little challenge in analysis; films are scratched near the feature of interest and AFM section analysis gives the film thickness. Unlike the as-cast films, the surface of ordered block copolymer films will be decorated by terraces (islands or holes) when the as-cast thickness is not commensurate with a lamellar thickness. Under such conditions,

using AFM cross-section analysis alone is insufficient to completely determine a thickness; instead an average thickness must be contrived from the density of surface features, $f$, the lamellar thickness $L_0$ and the number of complete layers below the surface, $n$. In other words, average thickness is obtained from volume conservation. In this regard, having measured the lamellar spacing ($L_0$), the volume of the sample with full of terraces will be the sum of the volume of the terraces and the volume of the material constituting the flat thickness just beneath the terraces. At equilibrium, the height/depth of the lamella spacing becomes $L_0$. The volume of the features becomes $\left(\text{total feature area x } L_0\right)$ whereas that of the flat film beneath the features becomes $x_0 y_0 n L_0$), where $n = 1, 2, 3...$ ($nL_0$ is the total number of lamella stack of the flat film with dimensions $x_0$, $y_0$ and $nL_0$). Then, another (ideally) flat film of the same x-y dimension as in the film with terraces, with a new thickness (say $h_{avg}$), is created by "smearing" the extra materials on the entire surface of the sample using a "butter knife". From conservation of volume, volume before smearing the extra materials = volume after smearing the extra materials (i.e. $\left(\text{total feature area x } L_0 + x_0 y_0 n L_0\right) = x_0 y_0 h_{avg}$. Dividing by $x_0 y_0$ yields, the required average thickness. Mathematically,

$$h_{avg} = f \times L_0 + n \times L_0. \tag{3.4}$$

where f = (total feature area)/$x_0 y_0$). As an alternative, the largest thickness $(n+1)L_0$ and thickness of only complete layers, $nL_0$ was considered in analysis. Neither resulted in significant changes in the overall trends observed. For the polymer used here, we find $L_0 = \sim 42 \pm 0.7$ nm in agreement with other measurements [55, 71]. Notice that the area of the features and the counting of the number of features is done with the help of imagej.

### *3.2.4. Mechanics*

In order to do the mechanics, one of the now floating films will be picked up with a piece of clean mica held with a tweezer and transferred to a PDMS substrate loaded on a strain stage. Subsequently, a compressional strain is imparted with the custom built strain stage. When under compression, the film buckles out of plane forming a sinusoidal pattern in a process known as wrinkling [15, 43, 12, 110, 20]. As compression is increased, the sinusoidal pattern evolves to eventually form a complex collection of delamination blisters or sharp localized bends [46, 80, 31]. A typical LSCM micrographs of an as-cast PS-b-P2VP film of thickness $h = 71$ nm under: zero-strain (3.3a), compression (3.3b), relaxed (3.3c) and transferred to a silicon substrate (3.3d) is illustrated in Fig. 3.3. A smooth and flat surface is observed while no strain is applied which eventually evolves into wrinkles and delaminations (brightest wrinkle peaks) as compressive stress beyond the critical strain for wrinkling, and delamination [31] is imposed. Confocal imaging of the sample while it is under compression, allows delamination width to be easily measured. More importantly, the heights of each pixel can be determined through LSCM's optical sectioning, from which the amplitude of the delamination [46] can be determined. Thus, we will have a very careful and complete measurement of the films location in three dimensional space at all stages of compression and relaxation. The measurement can easily verify the predicted post-buckled shape of the delamination topography defined as $g(x) = (A/2)(1 + \cos(2\pi x/\omega))$, where $g(x)$ is the surface, $A$ is an amplitude and $\omega$ is the width of the delamination [118]. By employing g(x), coupled with Euler-buckling theory, it is possible to give an estimate of the surface strain along the delamination crest as $\varepsilon_s \sim \kappa h$, where $h$ is the thickness of the film and $\kappa \sim \partial^2 g(x)/\partial x^2 \sim \frac{A}{\omega^2}$ is the peak curvature of the delaminated film. The delamination amplitude decreases as one moves from the crack edge to the tip of the delamination [46]. There is a strong correlation between delamination curvature and the the amount of damage

remaining once film is transferred to a flat silicon substrate. The most relevant feature exploited here is the critical point of the onset of plastic deformation (the yield strain).

## 3.3. Results and Discussion

In chapter two, the measurement of the onset of plasticity in polystyrene thin films was presented in detail. In that work, several observations were made: i) the onset of plasticity occurs at low strain, of the order of $\sim 10^{-3}$, ii) critical strain for plastic failure remains flat in the bulk region but rises as the film confinement increases, iii) the confinement induced increase of the yield strain begins as the film thickness drops below about ($\sim$ 100 nm). In the current chapter, a similar method is used to study the onset of yield strains of a series of films composed of P2VP, as-cast PS-b-P2VP and ordered PS-b-P2VP with variable thicknesses. The critical point is taken at the strain of the localization where damage is no longer visible. In the following subsections, the yield strain measured for each polymer mentioned earlier will be discussed in the following order: P2VP, as-cast PS-b-P2VP and ordered PS-b-P2VP. In all cases, comparison is made with the PS data we obtained in chapter two.

### *3.3.1. Yield Strain in P2VP*

The yield strain of poly(2-vinylpyridine) (P2VP) shows similar behavior to PS films. Both polymers have flat critical strain in the bulk region that dramatically increases as confinement increases. Notably, P2VP has critical strains of $\sim$ 0.4% greater than PS over the entire range of measurement as illustrated in Fig 3.4. The implication is that thin films made from P2VP can stretch further than PS before failure.

The best curve fittings to our data in Fig. 3.4 were made by exploiting the concept of a layer model discussed in chapter two. This model assumes enhanced molecular mobility (liquid-like layer) near the free-surface (over a few lengthscale) than in the bulk polymer.

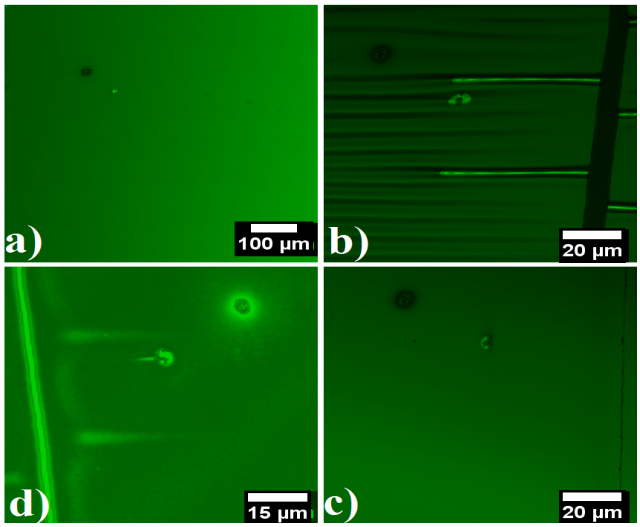


Figure 3.3. Typical surface morphologies of as-cast PS-b-P2VP films at every stages of the mechanics. A confocal microscope image of a) prestrain state. b) the same film under compression with lots of wrinkles and a couple of delaminations.c) the spot of the relaxed film corresponding to the previous delaminations and d) the same film after it has been relaxed and annealed above the glass transition temperature of PS-b-P2VP.

Many researchers, especially in the glass transition community, have made use of this model. For example, several authors [60, 36, 34, 95, 85, 11] have shown that the glass transition temperature of thin polystyrene films reduce significantly compared to the bulk value as confinement increases. With this argument in mind, we have adapted the layer model to our system that can be written as

$$\varepsilon_p(h) = (\ell/h)(\varepsilon_p - \varepsilon_p^\circ) + \varepsilon_p^\circ, \tag{3.5}$$

where $\ell$ is the size of the soft layer and $\varepsilon_p$ and $\varepsilon_p^\circ$ refer to the surface and bulk strain, respectively. The idea of defining the yield strain as a layer model stems from the fact that a larger strain is needed in the liquid-like layer before stress can be stored; since the stress can more easily relax away in the liquid layer than in the bulk layer. In this regard, fitting to our data in Fig. 3.4 give $\varepsilon_p = 0.012 \pm .001$, $\varepsilon_p^\circ = 0.001 \pm .001$, and $\varepsilon_p = 0.50931 \pm .001$, $\varepsilon_p^\circ = 0.26283 \pm .001$, respectively, for PS and P2VP, assuming a typical lengthscale $\ell =$ 10 nm.

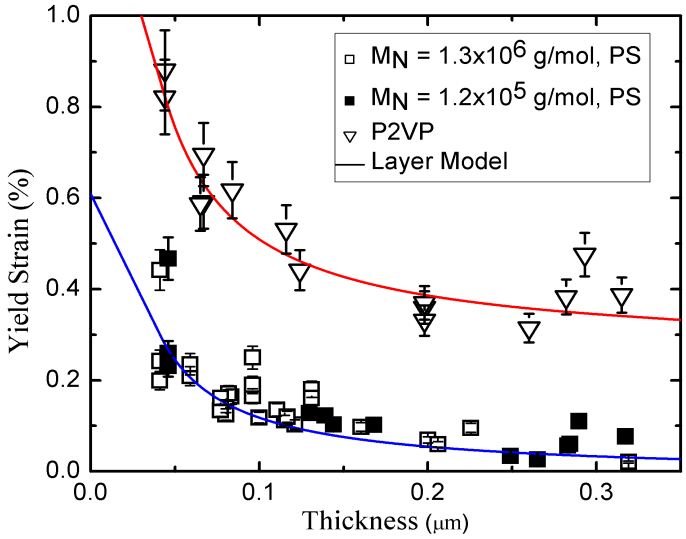


Figure 3.4. Comparison of the evolution of yield stain of PS and P2VP as a function of confinement. The two polymers reveal similar pattern in yield strain except the upward shifting of the yield strain in P2VP implying that P2VP might stretch further before failure compared to PS.

Now that the behavior of yield strains of each of the blocks (PS and P2VP) constituting our model material (PS-b-P2VP) is established, it is natural to ask how the diblock copolymer would respond to similar mechanical deformation. First, we focus on the as-cast PS-b-P2VP films (disordered state) followed by the ordered PS-P2VP films.

### *3.3.2. Yield Strain in As-cast PS-b-P2VP Films*

The yield strain of as-cast PS-b-P2VP not only shows a small value - of the order of 0.1%- but also increases when the thickness decreases below 100 nm as shown in Fig. 3.5. The value of the critical strain for the as-cast PS-b-P2VP overlaps with the PS data for thicknesses above $\sim$ 100 nm. However, a more exaggerated increasing of the yield strain was detected as shown in Fig. 3.5. It is believed that there is a possibility for a ultra thin films, which are inherently in a disordered state while in the bulk, transition to an ordered phase only due to spin coating under a certain degree of confinement [17]. Therefore,

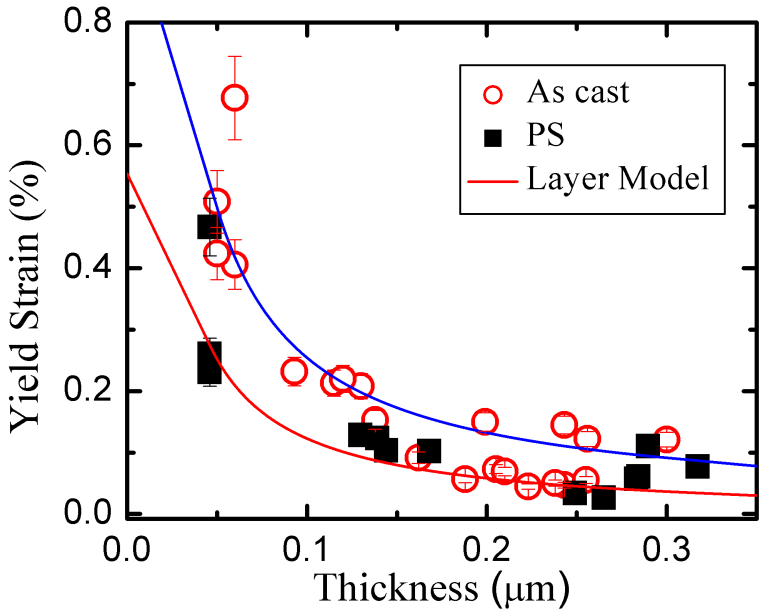


Figure 3.5. Critical strain as a function of film thickness of as-cast and PS films fitted to the layer model described in the text.

the disordered to ordered transition might be the reason why there is a highly pronounced increase of yield strain in the as-cast film with increasing confinement. We notice that disordered films are not well fit by the equation of the layer model.

### *3.3.3. Yield Strain In Ordered PS-b-P2VP Films*

In the foregoing discussions, we have established the behavior of yield strains for PS, P2VP and disordered PS-b-P2VP as a function of film confinement. Interestingly, there is no noticeable difference in the pattern of the yield strains measured in all the polymers - the yield strain remains flat in the bulk and dramatically increases in the confined region. We now turn to the response of ordered PS-b-P2VP films to similar mechanical deformation and investigate how the microstructural orders affect the onset of plasticity. For the diblock copolymer to undergo the self-assembly process and form the microstructural order we are interested in, it is essential to initiate the process. In the mean time, the surface

morphological evolution as well as the variation of yield strain as a function of annealing temperature will be investigated.

#### *3.3.3.1. Surface Morphological Evolution as a Function of Temperature*

In order to probe how the microstructural order affect the onset of plasticity in ordered PS-b-P2VP films, we first initiate the self-assembly process of the diblock copolymer into distinct microstructural orders. This is carried out by, among other methods, thermal annealing [37, 75] and solvent annealing [44]. In our case here, we use thermal annealing approach on a freshly cleaved mica substrate. In thermal annealing the copolymer is heated past its glass transition temperature, ($T_g \sim 100^{\circ}$C for PS and P2VP), for a predetermined time followed by quenching the sample down to room temperature (below $T_g$). During annealing, the polymer chains become mobile and rearrange toward thermodynamic equilibrium structure [4, 77]. When the sample is rapidly quenched below its glass transition temperature, the polymer structure is kinetically frozen due to the extremely low mobility of the chains. Given the composition of the block copolymer considered (PS block of $M_n = 40$ kg/mol and a P2VP block of $M_n = 40.5$kg/mol), alternating PS and P2VP layers (lamella) parallel to the mica substrate is formed at equilibrium. As it has already been demonstrated for the model polymer under consideration [55], PS block has a lower surface energy compared to P2VP and prefers to reside at the free surface; yielding lamella (alternating layers of PS and P2VP) parallel to the substrate.

For the realization of such microstructural order (alternating layers of PS and P2VP), series of samples of similar thicknesses were annealed to temperatures ranging from 165$^{\circ}$C - 185$^{\circ}$C under variable environments (open air, glove box filled with dry nitrogen). When annealed to a temperature above the glass transition of the polymer for an appropriate time, the surface of the block copolymer thin film is decorated by terraces (holes, islands, bi-continuous) when the film thickness is not commensurate with the lamellar spacing. For

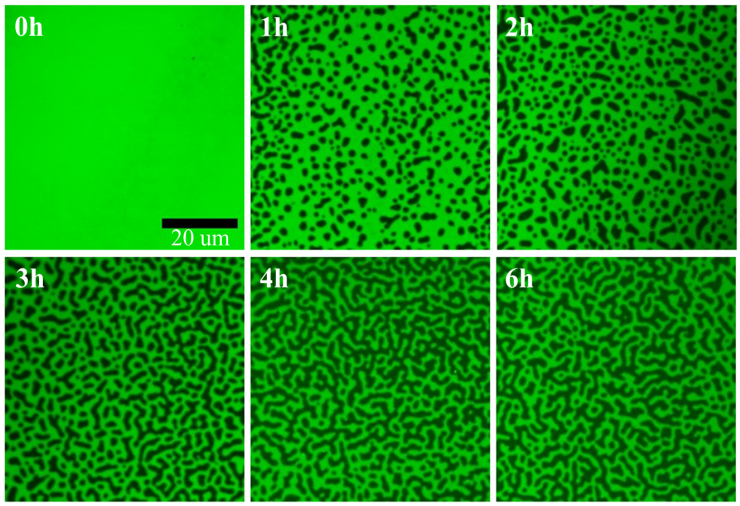


Figure 3.6. Surface morphologies of samples annealed at $175^{\circ}C$ for the annealing times indicated on the pictures. All of the samples are decorated by holes of lamella spacing $42\mu$m. The observed morphologies depend on the commensurability of the film thickness with the lamellar spacing. Scale bar in all the images is $20\mu$m.

example, Fig 3.6 illustrates the surface morphological evolution observed as the samples of similar thicknesses are annealed at a temperature of $175^{\circ}$C on Linkham hot stage for different annealing times. As time progresses, the domain sizes coarsen as expected (see Fig. 3.6). It is apparent from Fig. 3.6 that there will be self assembly of the polymer chains into periodic microdomains even at short annealing times (see samples in Fig. 3.6 annealed for 1-2 hours). Although the true thermodynamic equilibrium takes a long time to be reached, the fact that the surface terraces are not altering significantly upon further annealing (see samples in Fig. 3.6 annealed for 3-6 hours) could be an indication that an equilibrium may have been achieved [107].

#### *3.3.3.2. Yield Strain as a Function of Annealing Temperature*

For better understanding of how the microstructural orders contribute to yield strain, we then conducted an experiment of yield strain measurement with microphase separated

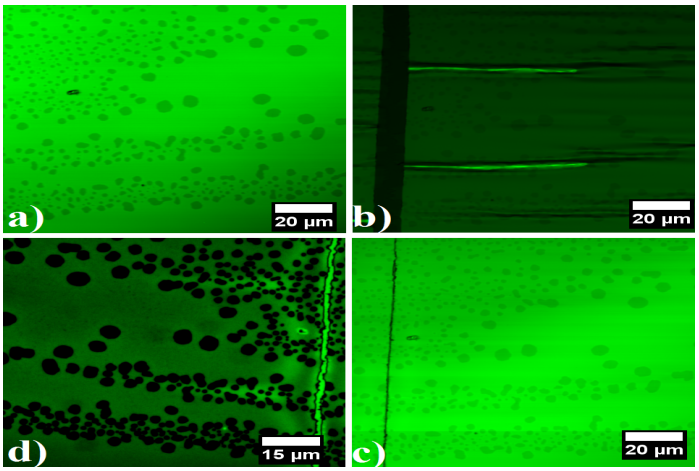


Figure 3.7. Surface morphologies of ordered PS-b-P2VP films at various stages of the experiment. A confocal microscope image of a) prestrain state. b) the same film under compression with lots of wrinkles and a couple of delaminations.c) the spot of the relaxed film corresponding to the previous delaminations and d) the same film after it has been relaxed and annealed above the glass transition temperature of PS-b-P2VP.

PS-b-P2VP samples using the same procedures outlined above for as-cast films. The pre and post buckling state of the sample is illustrated in Fig. 3.7.

Similar to the as-cast films, smooth and flat surface is observed while no strain is applied and eventually evolves to wrinkles and delaminations (brightest wrinkle peaks) as compressive stress beyond the critical strain for wrinkling and delamination is applied. In order to measure the yield strain, several samples of similar thicknesses were annealed at different temperatures for different annealing times. Measuring the yield strain of these microphase separated samples, we observe that the critical strain increases only for short annealing times and eventually relaxes to a finite value for lamella forming molecules as can be seen in Fig. 3.8. For the cylinder forming molecules, however, no significant change was noticed with varying annealing treatment. The inset in Fig. 3.8 makes it more apparent how the yield strain relaxes to a finite value as annealing temperature increases. Within our experimental error, the data plateau in the time scales ranging from 4h-8h. This observation has the implication that annealing a sample to a temperature more than 175$^{\circ}$C and above 4 hours has no significant effect on the yield strain measured as can be seen in Fig. 3.8.

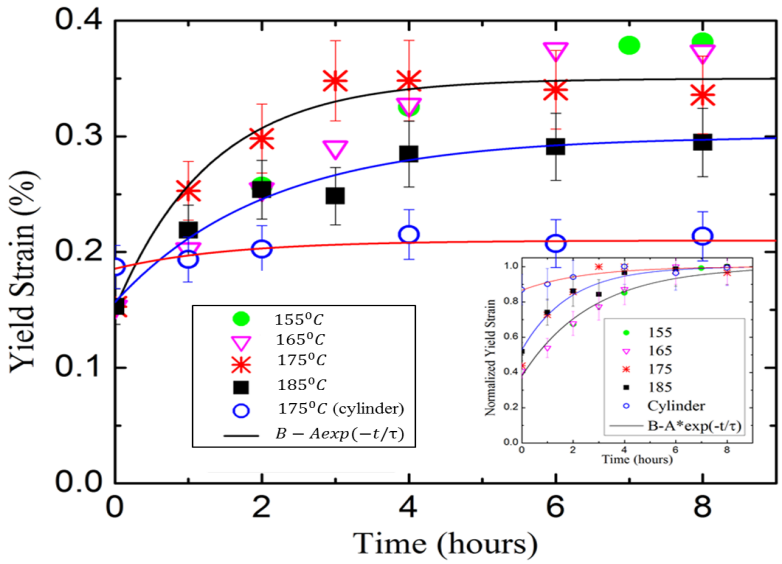


Figure 3.8. Evolution of yield strain of annealed block copolymer films as the annealing time increases. The figure shows that the yield strain, regardless of annealing temperature, relaxes to a finite value after short annealing time . The inset illustrates variation of the yield strain normalized to the respective equilibrium values as annealing time progresses.

The solid lines are the best curve-fitting to the data with an exponential function of $f(t) = B - A \times Exp(-t/\tau)$ where the best fit parameters $A, B$ and $\tau$ are different for each sample. This relaxation to the plateau region of each sample's data can be shown by the relaxation time versus annealing temperature extracted from $f(t)$ and plotted in Fig. 3.9, where the solid line is included to guide the eye of the viewer.

### *3.3.3.3. Yield Strain as a Function of Confinement*

In light of our observations that annealing a sample to a temperature exceeding 175°C for more than 4 hours has insignificant effect on the yield strain, we chose a temperature of 175°C and annealing time of 4 hours for the next experiment. At this temperature, we carried out an investigation of how the yield strain varies with thin film confinement. Consequently, we notice that there is a remarkable shift in yield strain in samples with microstructural orders as compared to the previously described system - as-cast PS-b-P2VP- as illustrated in Fig. 3.10. This increase of the yield strain for the self-

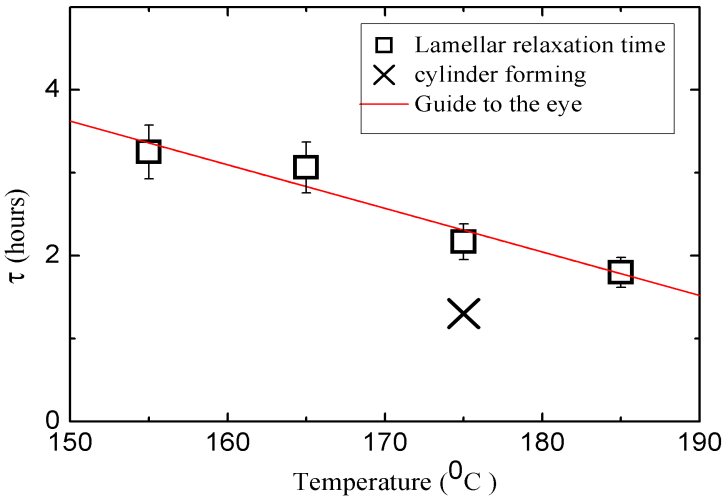


Figure 3.9. Illustration of the relaxation time versus annealing temperature extracted from $f(t)$ described in the text. In the fitting the outlying cylinder forming data is not included.

assembled samples is attributed to the internal microstructural orders. In addition, our careful measurement and analysis of these systems not only indicate that the value of the critical strain is very small - of the order of 0.1%- but also the yield strain increases when the thickness decreases below 100 nm.

### *3.3.4. Comparison of Yield Strains In PS, P2VP, As-cast and Ordered PS-b-P2VP*

While all the polymers considered in here reveal similar interesting patterns (such as low critical strain, flat critical strain in the bulk region, critical strain increases when confinement increases, upturning of the critical strain starts when film thickness $\sim$ 100 nm) in the yield strains, each has a different magnitude of yield strains (see Fig. 3.11). This differences have an implication that we are measuring a material specific property. Specifically, PS is found to be the one with the lowest yield strain (0.1%) whereas P2VP with the highest yield strain (0.4%) compared to all the three systems considered (PS, as-cast and ordered P2VP). Although the difference between the yield strain of PS and as-cast is not significant, still the as-cast PS-b-P2VP shows a tendency of being higher than PS.

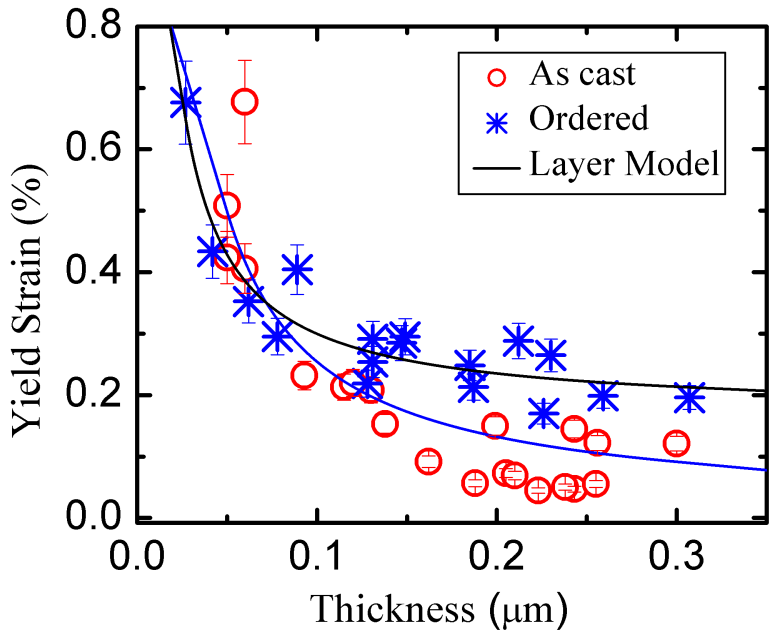


Figure 3.10. Yield strain as a function of film thickness of both as-cast and ordered films fitted to the layer model described in the text.

Since PS-b-P2VP is constituted from two homopolymers (PS and P2VP), it may be the case that the phenomenon we observe (yield strain of the copolymer lies in between the yield strains of PS and P2VP) stems from the fact that yield strain is measured for a material made from two different materials with its own properties. The implication is that PS-b-P2VP shares some properties from each constituents and hence its yield strain falls in the middle of the individual homopolymers' strain. On the other hand, there is a noticeable increase in the yield strain of ordered PS-b-P2VP compared to the as-cast PS-P2VP as microstructural order takes place. Fitting the layer model defined in equation 3.5 to our data in Fig. 3.11, gives $\varepsilon_p = .2886 \pm .001$, $\varepsilon_p^\circ = .15916 \pm .001$ for self assembled PS-b-P2VP films.

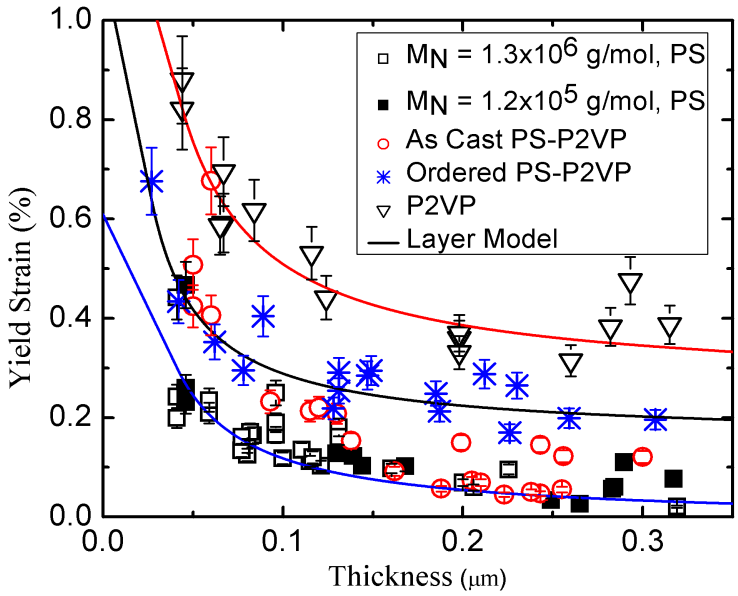


Figure 3.11. Comparison between the yield strains as a function of film thickness of polystyrene, as-cast and ordered block copolymer films fitted to the layer model described in the text.

### 3.4. Summary

The purpose of the present research was to investigate how the onset of strain is affected by the microstructural order formed when block copolymers undergo self-assembly. We focused only on symmetric PS-b-P2VP which has a strong Flory interaction parameter between the two individual blocks and their relative interaction with air/substrate. Thin films made from this block copolymer has the ability to self-assemble into well-aligned lamellar domains parallel to the substrate if the total film thickness is commensurate with the step height $L_0$. For better understanding of the response of such films to mechanical deformation, we first studied how the individual blocks (PS and P2VP) constituting our model material (PS-b-P2VP) respond to mechanical deformations followed by how both the as-cast and self-assembled films made from PS-b-P2VP respond. Poly(2-vinylpyridine) (P2VP) shows similar pattern with the yield strain of PS films we measured. Although both

polymers have flat yield strain in the bulk region and dramatically increase as confinement increases, there is noticeable upward shift of the yield strain in P2VP (by 0.4%) as compared to PS. This has an implication that thin films made from P2VP can stretch further before failure as compared to PS films.

Our measurements in the yield strains of both the as-cast and ordered PS-b-P2VP are also consistent with the yield strain of polystyrene we measured. The results are significant in three respects: 1) the trend of the yield strain follows the same pattern as the function of confinement (see Fig. 3.11), 2) the up turning of the yield strains start nearly at about the same film thicknesses ($\sim$ 100 nm) and increases significantly with increasing confinement, and 3) the yield strain occurs at much lower strains, of the order of 0.1%, albeit it causes the material to deform plastically. In addition, self-assembled PS-b-P2VP films and films decorated with terraces (islands, holes and bi-continuous) show higher yield strain as compared to as-cast PS-b-P2VP and polystyrene films, suggesting that the microstructures slightly increase the failure strain of the films. This implies that films with microstructural orders require high strain to break. It is essential to emphasis here that such measurement has implications for many current experimental investigations of the elastic properties of thin polymer films, particularly in experiments attempting to probe the far from threshold elastic behavior.

# 4. LOCALIZATION IN AN IDEALIZED HETEROGENEOUS ELASTIC SHEET

## 4.1. Background

When a system consisting of a thin film bound to an elastic substrate is subjected to a compressive stress, the film will initially be compressed in-plane. As compression increases, the film will buckle out of plane by forming a repetitive sinusoidal pattern (also known as surface wrinkling) when a critical wrinkling stress is reached [110, 20]. If the compression is stopped, the film remains wrinkled. However, when confined beyond the wrinkling threshold stress, focusing (localized) deformation in the film can occur [31, 81, 118]. Often times such deformation is associated to a form of energy focusing. In the limit of small strain, an elastic energy of the system is smoothly distributed throughout the surface of the film. In the large strain limit, however, the initially smoothly distributed elastic energy becomes more nonuniform and concentrated within certain strongly bent regions (region with high curvature). One of the simplest examples to consider in demonstrating the heterogeneous energy distribution in a system is to look at the response of a crumpled piece of paper. In a crumpled piece of paper, there arise highly deformed ridges and flat planes throughout the surface of the paper that is strongly confined or localized implying the non homogeneous energy distribution causing the mixed states (flat planes and highly deformed ridges) [123, 128].

Localized deformation is ubiquitous in many natural and engineering materials. For example, the development of chaotic fluid motion into turbulence, where the kinetic energy injected uniformly into a fluid becomes progressively concentrated in regions of

[0]Andrew Croll and Bekele Gurmessa designed and conducted the experiment in this chapter in close cooperation. The work in this chapter is *in preparation for publication.*

strong vorticity in space and strong intermittency in time (alternately ceasing and beginning again), strong mechanical forcing of a solid that leads to fracture [123].

In their recent publications, Pocivavsek et al. [93] showed the transition of uniform undulations to localizations of a homogeneous system (polymer thin film) bound to an elastic foundation or on a water substrate when a uniaxial stress is applied. They demonstrate that such transitions occur when $\Delta \sim 1/3\mathrm{L}$ where $\Delta$ is the lateral displacement of the system due to compression and $L$ is the length of the sheet on a foundation. Furthermore, Croll and his colleagues [23] have also shown similar transition by considering a heterogeneous system (self-assembled block copolymers). Their finding suggests that the transition take place when the lamella spacing of the block copolymer becomes the same as the natural buckling wavelength of the film. These demonstrations provide a great insight for systems with a uniform stiffness through out its surface. The natural question one could raise here is how a similar system with a non-uniform stiffness would respond when subjected to similar mechanical deformation (uniaxial stress).

In this chapter, we discuss the response of nanoscale films with idealized, non-homogenous stiffness subjected to uniaxial compression. The idealized/patterned surface layers are created by selective ultraviolet/ozone (UV/$O_3$) treatment of the top surface of polydimethylsiloxane (PDMS) using a mask. By controlling the exposure time of UV/$O_3$, samples ranging from continuous thin films to sets of isolated small plates were created. Despite studying of surface modification of PDMS during the UV/$O_3$ exposure [33, 88, 7], no one has yet used such heterogeneous systems to a controlled study of localized deformation. To this end, the goal of the current chapter is to investigate how the modified heterogeneous surface layers respond to mechanical deformation. First, the chemical details behind the creation of a rigid layer on PDMS with UV/$O_3$ will be discussed. Following this, the experimental approach used and the results will be discussed.

### *4.1.1. Interaction of Ultra-violet/Ozone with Air*

Exposing a sample of PDMS to UV/$O_3$ is carried out in air at atmospheric pressure (as opposed to vacuum) in a UV/$O_3$ Chamber (Jelight Company, Inc., Model 42). This results in an interaction between UV radiation and air. Ultraviolet (UV) radiation is part of the electromagnetic spectrum whose wavelengths lie in the range of 10nm-400nm as illustrated in Fig. 4.1. This wavelength range is shorter than visible light, and it is invisible to the naked eye. The chamber contains a sample holder and the UV/$O_3$ source called low pressure mercury lamp. The low pressure mercury lamp emits radiation strongly at two wavelengths, 184.9 nm and 253.7 nm. The two wavelengths emitted by the UV source have unique functions. The first wavelength is absorbed by oxygen molecules in the air and leads to the generation of ozone while the second wavelength is absorbed by ozone, not by molecular oxygen. As absorption is followed by dissociation, the molecular oxygen at 184.9 nm dissociates to form atomic oxygen as indicated in 4.1 below. Eventually, the atomic oxygen reacts with molecular oxygen to form ozone (see 4.2 below). On the other hand, the 254.7 nm wavelength is strongly absorbed by ozone which dissociates into molecular oxygen and atomic oxygen as indicated in 4.3 below [88, 7].

$$\mathrm{h}\nu(185\mathrm{nm}) + \mathrm{O}_2 \longrightarrow \mathrm{O} + \mathrm{O} \tag{4.1}$$

$$\mathrm{O}_2 + \mathrm{O} \longrightarrow \mathrm{O}_3 \tag{4.2}$$

$$\mathrm{h}\nu(254.7\mathrm{nm}) + \mathrm{O}_3 \longrightarrow \mathrm{O} + \mathrm{O}_2 \tag{4.3}$$

The absorption of 254.7 nm by ozone is considered as the reason for the continuous destruction of ozone in the chamber [88].

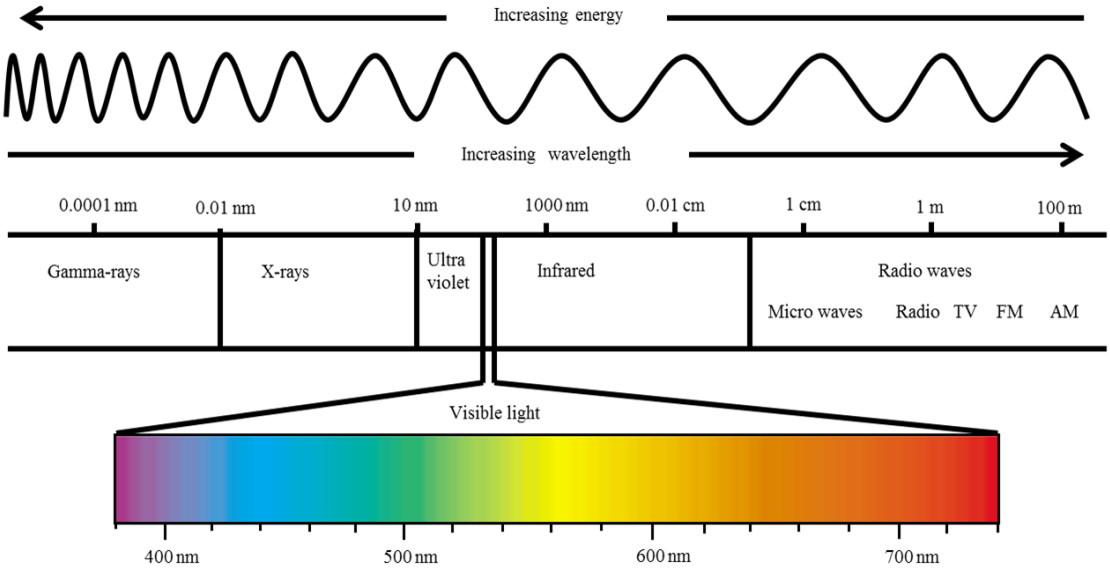


Figure 4.1. Electromagnetic spectrum of radiation. Redrawn from [104]

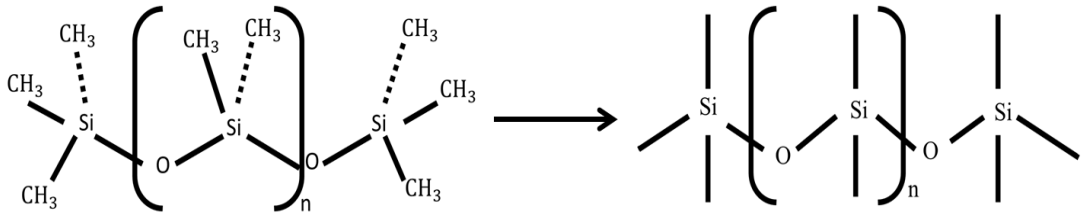


Figure 4.2. Illustration of the chemical structure taken from the surface of a PDMS before treatment ( left) and after UV/$O_3$ treatment (right). After the methyl groups are removed by the absorption of UV/$O_3$ radiation, atomic oxygen combines with the silioxane component remaining behind and hence silicon oxide layer is formed on the surface of the PDMS.

### *4.1.2. Interaction of Ultra-violet/Ozone with the Sample*

It has already been documented that the surface of a PDMS is chemically modified when it is exposed to UV/$O_3$ radiation [33]. The process involves photo-sensitized oxidation. That is, the molecules of the PDMS are excited or dissociated by the absorption of short-wavelength UV radiation resulting in free radical formation. Berdichevsky et al. [7] and Ouyang et al. [88] have demonstrated that both oxygen and ozone can react with organic materials. When polymers and organic materials absorb UV/$O_3$ radiation, there will be formation of free radicals which eventually react with the atomic oxygen and ozone to form some bi-products such as carbon dioxide (C$O_2$) and water (H2O). In a polydimethylsiloxane (PDMS), which is a silicon containing polymer as shown in Fig. 4.2, treated with UV/$O_3$, the methyl groups are dissociated by the absorption of UV/$O_3$ radiation. This desorption of the organic portion (methyl group) leaves the siloxane (silicon backbone) component behind. As a result, oxide layer is formed on the surface of the PDMS when atomic oxygen combines with the silicon remaining behind. This silicon oxide layer is what we call thin film. It has been demonstrated that the thickness of the layer is directly proportional to the duration of treatment [35].

## 4.2. Experimental Approach

### *4.2.1. Sample Preparation*

Cross-linked polydimethylesiloxane (PDMS) was made by mixing a 40:1 by weight ratio of pre-polymer and cross-linker (Dow chemical Corning, Sylgard 184). PDMS is a Si based organic polymer that is highly viscous liquid at room temperature and is optically transparent. Thorough mixing for about ten minutes is needed in order to ensure the curing agent is uniformly distributed. Mixing introduces air bubbles thats need to be removed (degassed) before curing. To do so, the sample is placed in a vacuum oven (Napco 5831

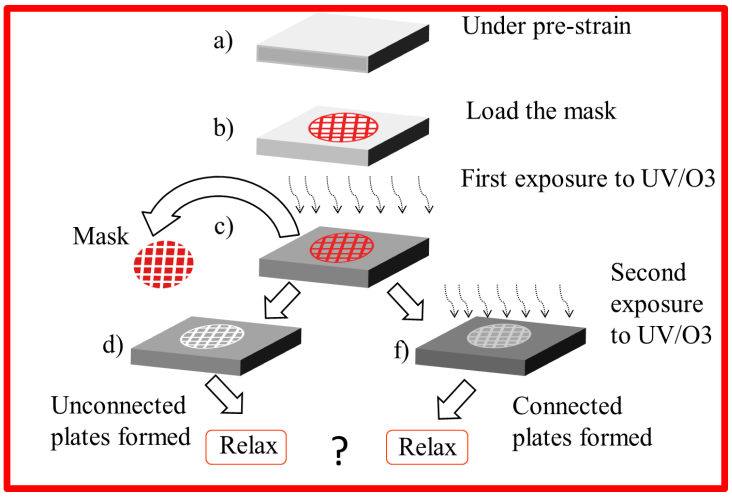


Figure 4.3. Schematic illustration of ultraviolet-ozone(UV/$O_3$) treatment of the surface of PDMS for pattern transferring. A pre-stretched PDMS (a) loaded with a TEM grid mask (b) was irradiated to UV/$O_3$ light (c). As a result of the UV/$O_3$, the surface of the PDMS is patterned (d). Re-exposing the sample to UV/$O_3$ (f) creates additional layer on the already exposed regions and new thinner layer on the previously covered region. After removing the compressive stresses, how will each sample (d and f) respond?

Vacuum Oven). Then the valve of the oven will be closed and released in certain time intervals until the trapped bubbles are fully removed. After degassing, the polymer mixture is poured into a 9.6 cm x 9.6 cm petri dish with a thickness of about 3 mm and cured at 85°C for two hours in the vacuum oven and then are kept in the oven for the next 12-15 hours. After cooling, the PDMS is cut into a rectangular sections of 1.2 cm x 7 cm x 0.3 cm.

### *4.2.2. Surface Patterning*

In order to create a controlled surface pattern, the strategy depicted in Fig. 4.3 has been used. First, an initially flat, un-patterned PDMS is stretched to a pre-determined strain (see Fig. 4.3a). Then, the PDMS is loaded with Transmission Electron Microscopy (TEM) grid used as a mask (see Fig. 4.3b). Finally, the pre-stretched PDMS loaded with the grid is placed in a UV/$O_3$ Chamber (Jelight Company, Inc., Model 42) and exposed to UV/$O_3$

(see Fig. 4.3c). The chamber consists of a low pressure mercury lamp designed to emit radiation strongly at 184.9 nm and 253.7 nm wavelengths. Ultraviolet/ozone treatment of the top layer of the PDMS this way yields four distinct regions: 1.) *bulk region* - a region which is not covered by the mask, 2.) *ring region* - a region covered by the wide edge of the mask and is not initially exposed to UV/$O_3$, 3.) *plate region* - a region exposed to the UV/$O_3$ through the hole of the mask, and 4.) *the in between plates region* - a region protected from UV/$O_3$ by the bar of the mask and is confined between two treated plates. For future convenience, the first two regions are termed as continuous regions while the last two as patterned regions. Although the continuous sheet of the bulk region and the isolated plates are exposed to the same dose of UV/$O_3$, they differ in plate-size and boundary conditions. The bulk regions are considered infinite in length and unbounded whereas the plates are confined by untreated strips of PDMS. Notably, this boundary can be manipulated through a second UV/$O_3$ exposure once the mask has been removed. In the first route (see Fig. 4.3d), both the ring and the in between regions are not exposed to UV/$O_3$ in the experiment. They are protected by the mask. When the sample is re-oxidized during a second exposure time after the mask has been removed (see Fig.4.3f), thinner layers of $SiO_x$ will be created between the plates. Of course, the thickness of the plates will also increase. Doubly exposed samples are termed "connected" whereas singly exposed samples are termed "unconnected". Typical examples of continuous (ring and bulk) and patterned (In between and plate) surfaces are shown in Fig. 4.4.

### *4.2.3. Buckling Mechanics*

The idealized inhomogeneous surface, with its surface patterned into regions with variable stiffness, is slowly released from the pre-strain (the global strain). This releasing of the pre-strain of the PDMS results in buckling of the $SiO_x$ layer. While the pre-strain is released, the Poisson effect induces tensile stress in the perpendicular direction of the pre-

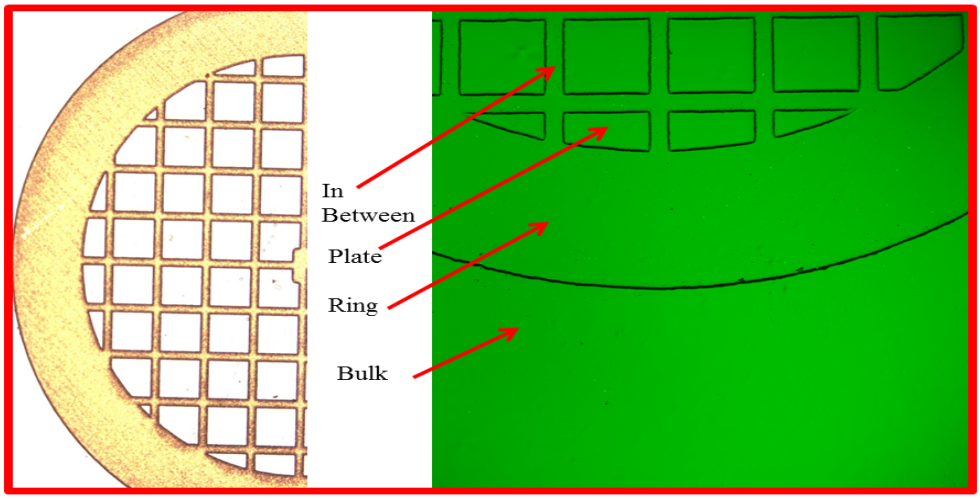


Figure 4.4. Illustration of part of the TEM grid used (left) and the four regions formed during surface patterning (right). The squares of the grid are 205$\mu$m X 205$\mu$m and a bar of 45$\mu$m wide. The confocal microscopy image of a sample under a pre-strain state is shown to the right. Ideally the plates and the in between regions take the size of the hole and the bar width at a prestrain state.

strain. It is important to note that all regions will not respond to the compressive stress at the same time due to differences in stiffness (see Fig. 4.5). They respond only when the critical stress of each region is attained. Once the critical stress of each region is reached, the layer buckles out of plane in order to relieve of the compressive stress. The corresponding width and depth of the undulations are controlled via controlling the UV/$O_3$ treatment time as well as the amount of the globally applied pre-strains.

## 4.3. Results and Discussion

### *4.3.1. Buckling Profiles as a Function of Treatment Time*

The mechanical response of idealized inhomogeneous elastic sheet with different layer (film) thickness and mechanical stiffness (Young's modulus) was studied. The first thing we have looked into was how the buckling profiles change as a function of exposure

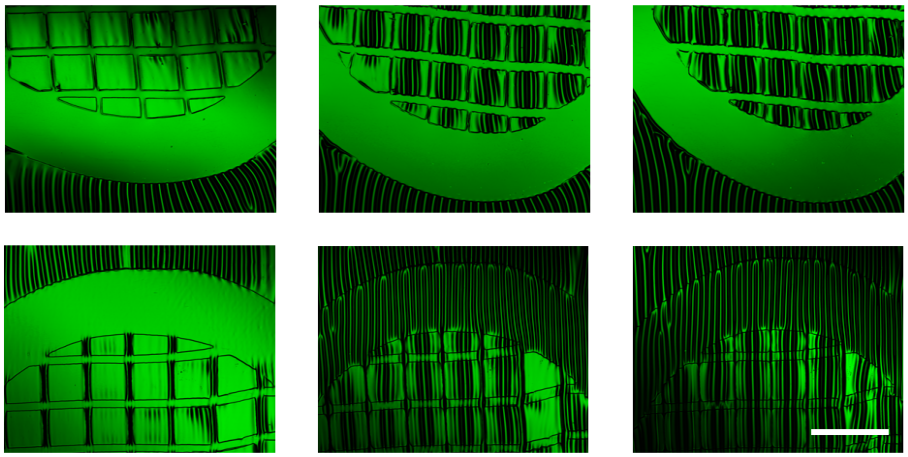

Figure 4.5. Typical laser scanning confocal microscopy images of unconnected plates (top row) and connected plates (bottom row) under the same mechanical strains of 13.94%, 22.38% and 28.15%, respectively, from left to right). For each sample, the same spot is scanned for three times under three different strains. Both the connected and unconnected plates are treated for the same amount of treatment time of total 9 minutes.

time. To study this, arrays of masked PDMS samples were considered and exposed to different exposure times ranging from 1 minutes - 8 minutes. Previous studies have also shown that large exposure time increases not only the stiffness of the PDMS surface but also the thickness of the silicate layer ($SiO_x$) created [128]. Here, the dependence of the buckling profiles (amplitude and wavelength) on the exposure time of UV/$O_3$ and on the pre-strain level have been systematically studied for continuous samples. The result shows that both the wavelength and amplitude increase linearly as exposure time increases as illustrated in Figs. 4.6. All the samples for this measurement were subjected to the same global strain of 31%.

Next, the response of each region to variable applied strain have been explored by exposing the sample to a fixed total UV/$O_3$ exposure time of 9 minutes. Our results indicate a clear difference between how the continuous regions (bulk and ring) and the patterned regions respond to the applied compressive stress.

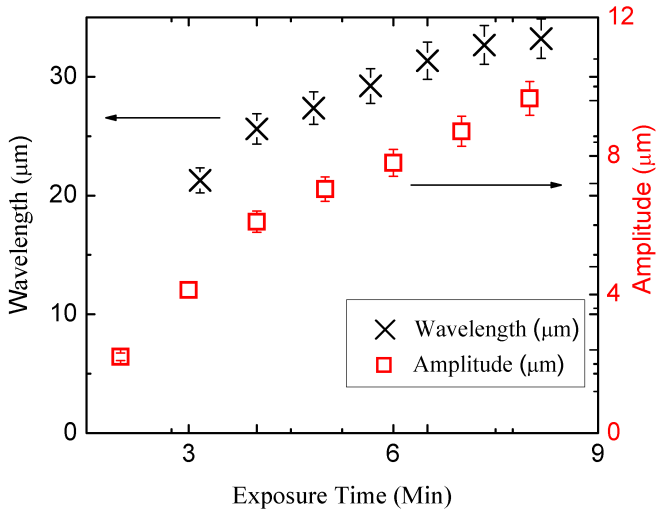


Figure 4.6. Evolution of the buckling wavelength and amplitude as a function of various ultraviolet/ozone (UV/$O_3$) exposure time. As the exposure time is increased, the buckling profiles increase.

### *4.3.2. Continuous Region*

Continuous region refers to the bulk and ring regions. In a singly exposed sample, out of the two regions, only the bulk region form uniform undulations when the pre-strain is relaxed. Nothing happens to the ring area regardless of the magnitude of the compressive stress imposed. This is because the ring region does not have an $SiO_x$ layer on its surface. Hence, its surface remains as the initial elastomer as shown in the top row of Fig. 4.5. When the sample is re-oxidized during a second exposure time, after the mask has been removed, thinner layer of $SiO_x$ is created in the ring region. Moreover, the thickness of the bulk region increases during the second exposure. When placed under compression, now both the bulk and the ring regions respond to the compression (see the bottom row of Fig. 4.5). They form isotropic undulations under compressive stress. Under a small strain limit, observing such uniform undulation is not surprising. What is more intriguing is that these regions remain wrinkled even in the limit of our maximum global (and local) strains used here, as illustrated in Fig. 4.7.

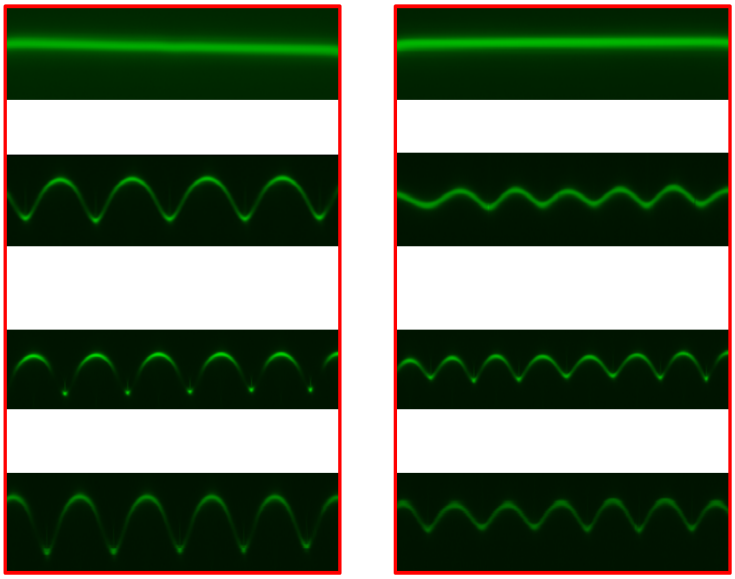

Figure 4.7. 3D cross sectional view of the continuous regions (bulk (left) and ring (right)) of a sample under mechanical strains of (0,0)%, (21.5, 11.0)%, (24.9, 15.0)% and (28.2, 19.7) % from top to bottom, respectively). The numbers in the parenthesis represent the global and local strains, respectively.

### *4.3.3. Patterned Region*

The patterned region consists of plates and the in between plates regions. In a small strain limit, the patterned region also responds to mechanical deformation similar to the continuous region. That means, both the plates and the in between plates regions form uniform undulations when low strain is applied. In the large strain limit, however, the response of the patterned region gets more complicated. This is due, in part, to the inhomogeneity of the sample's stiffness. As the strain increases, there is a transition from isotropic undulation to localization, a behavior that is never observed in the continuous region over the strain range used in this experiment. To have a better understanding of the response of the patterned region, the following questions must be answered: how is a globally applied strain distributed across each region? how does each region respond to its local strain?

#### *4.3.3.1. Unconnected Plates (Singly Exposed Sample)*

Unconnected plates are part of the patterned region whose lateral dimensions are confined by boundary conditions that arise due to the untreated soft regions of the PDMS surfaces. Similar to the continuous region, such plates also show periodic undulation in low strain limits. When the applied strain is increased, however, the uniform undulations slowly transition to a *single dominant localization*, often at the *middle of the plates*, whose depth increases at the cost of the neighboring wrinkles as indicated in the cross sectional view of Fig. 4.8. To understand the response of the plates, it is essential to consider how a globally applied strain is distributed in the patterned region. Since the patterned region is not a homogeneous solid, strain should not be expected to be uniform. One way to quantify this effect is through measuring strains locally. To this end, a 3D LSCM picture is taken before every increment of the global strain and the width of the plates and the in between regions are measured. As indicated in Fig. 4.9, the local strains measured for the unconnected plates as well as the bulk regions are similar. Even though, these regions experience similar local and global strains, their topographies are notably different (compare Figs. 4.7(left) and 4.8(right)). In addition, we measured the amplitude of the crest that develops into a dominant localization and the average wavelength as the global and local strains are varied (Fig 4.10). The amplitude of the bulk region grows as a square root of strain ($A \sim \varepsilon^{1/2}$), as expected, with both global and local strains (see the top row of Fig 4.10). In contrast to the bulk region, however, the amplitude of the plates grows monotonically (see the bottom row of Fig 4.10) with the strains. In addition, when the wavelengths of the bulk and plates are compared, we observe that they decrease with both global and local strains (see the top left of Fig 4.10). More importantly, the different wavelengths collapse to a master curve when plotted as a function of local strains implying that the small plates do not significantly impact the wavelength (see the top right of Fig 4.10).

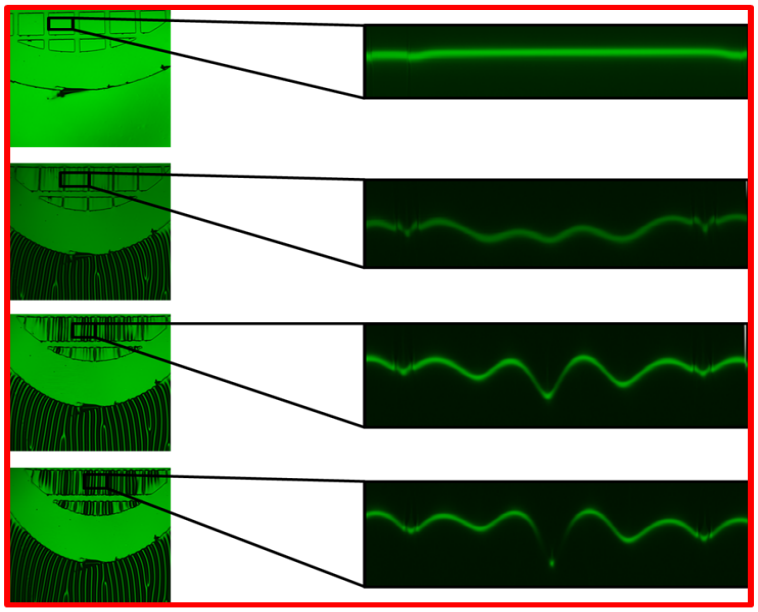

Figure 4.8. Laser scanning confocal microscopy images of a sample with unconnected plates (left column) and the corresponding 3D cross sectional view of a particular plate (right column) under mechanical strains of (0,0)%, (21.5, 11.0)%, (24.9, 15.0)% and (28.2, 19.7) % from top to bottom, respectively). The numbers in the parenthesis represent the global and local strains, respectively.

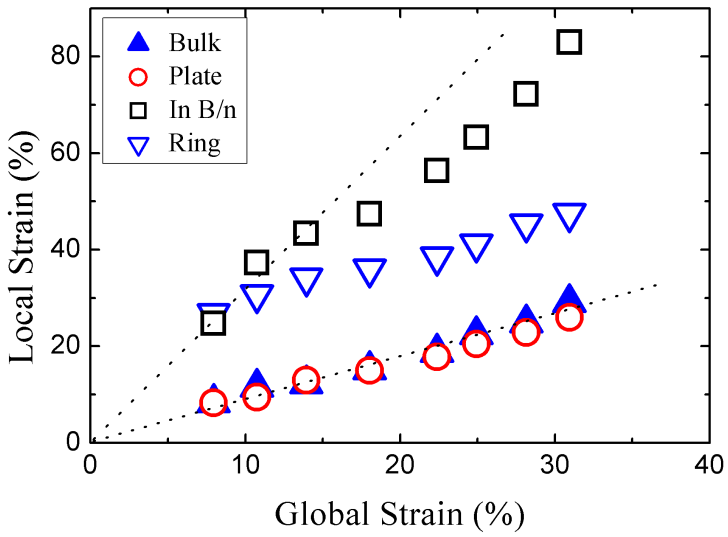


Figure 4.9. Local strains of all the four regions of a sample with unconnected plates as a function of the global strain.

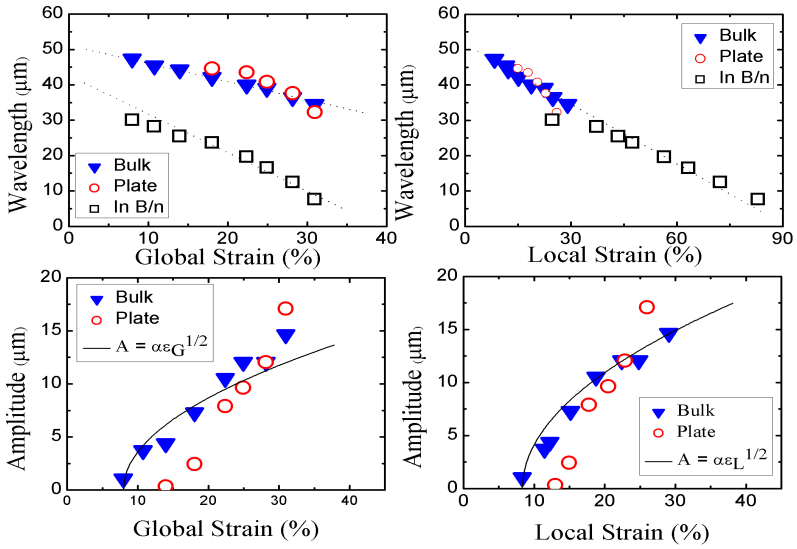


Figure 4.10. Variation of the wavelength of undulation and depth of the bulk region and unconnected plate as a function of the corresponding global and local strains.

### *4.3.3.2. Connected Plates (Doubly Exposed Sample)*

Our initial hypothesis of the reason why the two systems (bulk and isolated plates) subjected to identical treatment conditions (treatment time, global and local strains, thickness) respond differently was plate-size and boundary conditions. To further validate our assumption, we have repeated another similar experiment where the boundary conditions are changed through re-oxidizing a sample under identical treatment times. The plate created in this way is termed as *connected plates*. In contrast to unconnected plates, the boundary conditions of the connected plates arise due to small thickness oxide/silicate layers formed by re-exposing the already treated sample with UV/$O_3$ radiation after the mask has been removed. The bottom row of Fig. 4.5 illustrates the confocal microscopy images of a sample re-oxidized for the same amount of time as the unconnected plates (9 minutes) and subjected to the same mechanical strains of 13.94%, 22.38% and 28.15%, respectively, from left to right. Again, similar to the continuous region, the patterned region also undergo uniform wrinkling for small strain limit and eventually evolves to localization

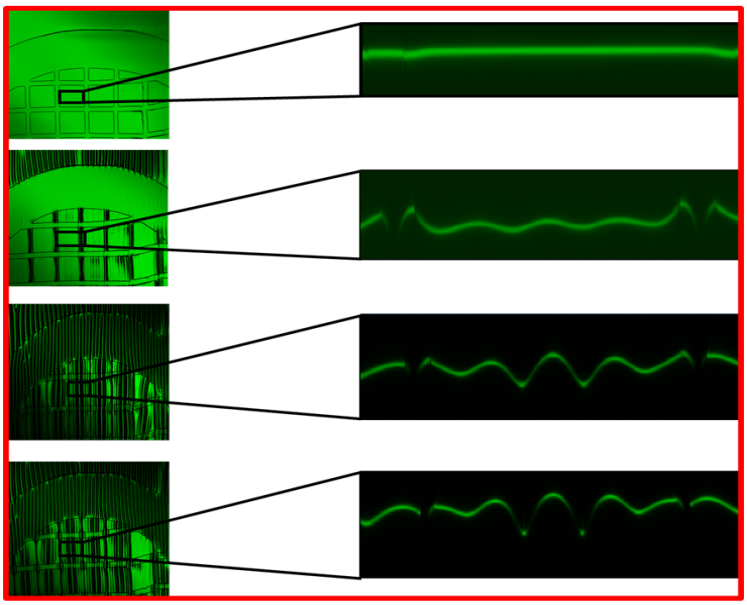

Figure 4.11. Laser scanning confocal microscopy images of a sample with connected plates (left column) and the corresponding 3D cross sectional view of a particular plate (right column) under mechanical strains of (0, 0)%, (13.94, 11)%, (22.4 19.7)% and (28.15, 21.7)%, from top to bottom, respectively). The numbers in the parenthesis here represent respectively the global dna local strains.

as the applied strain is increased. Unlike the localization observed in the unconnected plates, however, the connected plates form two symmetric localizations as illustrated in Fig. 4.11. This could be due to change in the boundary condition, otherwise, it would have been similar to the morphology observed for the unconnected plates. This has an implication that if the thickness of the in between region were the same as the plate, the result would be a continuous sample which undergoes uniform undulations as described in the continuous region. In the unconnected plates, the majority of the global strains are absorbed by the "in between plates region" (softer region) and hence the plate will be subjected only to reduced local strains only.

When the local strains of each region of the doubly exposed samples were measured, similar strain behavior as in the singly exposed samples was observed as the global strain is increased. This is shown in Fig. 4.12. Despite the similarities in local strains of the two regions, connected and unconnected plates, the response of the two regions are

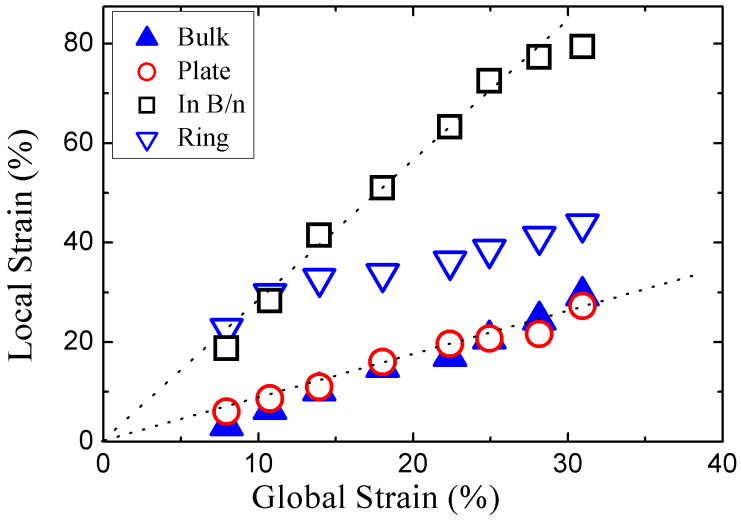


Figure 4.12. Illustration of how local strains of all the four regions of a sample with connected plates evolve as a function of global strains.

not morphologically the same (compare Figs. 4.8 and 4.11). Furthermore, the buckling amplitude and wavelength of the response were measured as a function of both global and local strains. As the strain increases, the amplitude increases whereas the wavelength decreases as illustrated in Fig. 4.13. The solid line in the amplitude is curve fits to the square root of the corresponding strains. Plotting the different region's wavelength as a function of local strain collapses onto a master curve as shown in the top right of Fig. 4.13. This collapse imply that each region moves proportionally (i.e. if one region shrinks more, there will always be a region which shrinks less) when the global strain is applied.

Based on what has been observed in the previous sections, a phase map (state diagram) is constructed for each regions change of states as in Fig. 4.14. As discussed earlier, the transition of each region from unbuckled state to wrinkled requires a threshold strain which vary for all the regions. The phase map clearly shows that the continuous regions remain wrinkled, even under large compressions. However, the patterned regions undergo both unbuckled to wrinkled and then wrinkled to localized states. Considering the

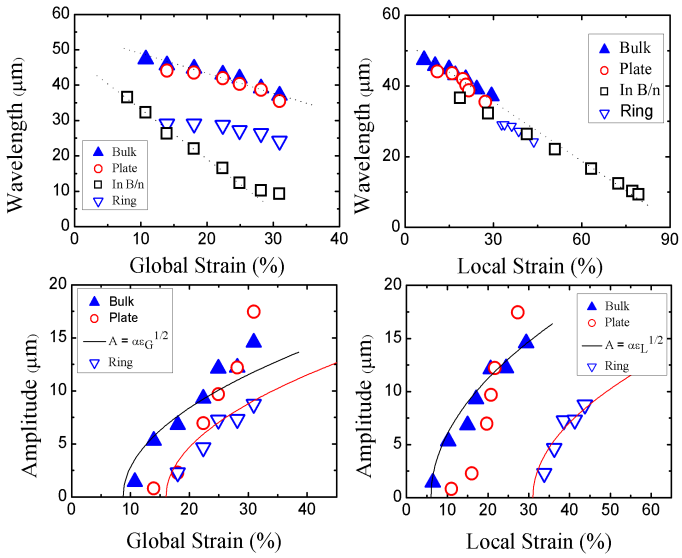


Figure 4.13. Summary of buckling profiles of samples with connected plates: The top row is wavelength as a function of global (left) and local (right) strains of each region whereas the bottom row amplitudes of the same samples as a function of global and local strains. The solid lines are curve fitting to square roots of the corresponding strains.

onset of wrinkling and localization, we observe that the "in between plates region" buckles first, followed by the bulk, the plate and finally the ring region.

#### *4.3.3.3. Simple Scaling: Spring Model*

Previously, we have measured the buckling profiles and local strains of isolated plates by exposing the plate boundaries to a fixed total exposure time. For a better understanding of how the buckling profiles of isolated plates are affected by a change in the boundary conditions, local strains of plates have been monitored (see Fig. 4.15). As can be seen in the figure, the increase in local strain is directly proportional to the exposure time of the boundary layers at a particular global strain. As the exposure time of the "in between plates" region increases, the local strain of the plates also increases. This has an implication that, the in between plates region is no more taking a large amount of global strain as when it was softer. As a result, the plate gets large local strain as opposed to when

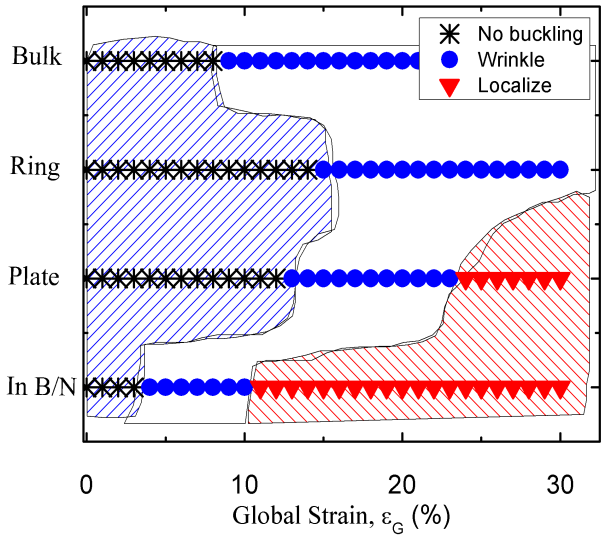


Figure 4.14. State diagram depicting the onset of buckling as a function of global strains.The symbols indicate: nothing happens (stars), wrinkles (circles) and localization (triangles). Comparing how quickly each region localizes, we notice that the patterned region undergoes localization as well whereas the continuous region remains wrinkled within the range of strain applied ,30%.

the "in between plate" is soft to absorb a majority of the global strains. When the ratio of local strains to the global strains is plotted as a function of the inverse of the exposure time ratio of the plates to the in between plates region (i.e. the exposure time of the in between plates to the total exposure time of the plates (9 min)), the data collapses to one master curve, as shown in Fig. 4.17. In an effort to modeling the data, a simple system of two springs connected in series is hypothesized.

The model consists of two springs having spring constants $k_1$ and $k_2$ representing, respectively, the plate and the in between plates region. Initially, the springs are assumed to have zero displacement and width of $x_1$ and $x_2$, and the total of $x_1$ +$x_2$. Once deformed, the total length of the springs change as:

$$\Delta X = \Delta x_1 + \Delta x_2. \tag{4.4}$$

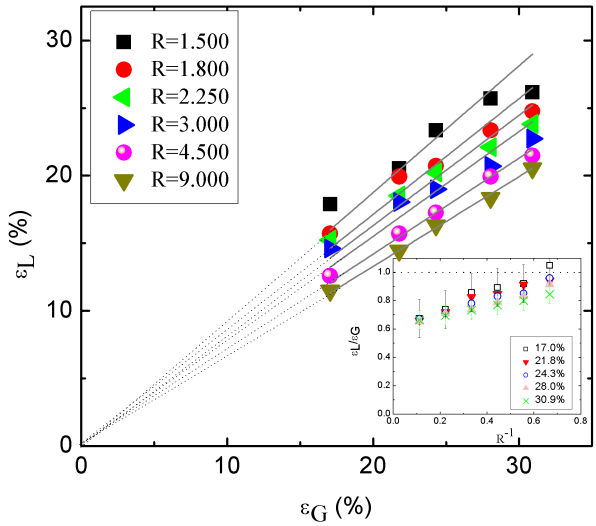


Figure 4.15. Variation of local strain as a function of global strain of a connected plate as oxidation time of the in between region increases. The ratio, R, denotes the ratio of the total exposure time of the plates (9 minute) to the variable exposure time of the in between plates region (1min-6min). The data shown in the inset indicate the collapse of the data in the main panel when plotted as a function of $R^{-1}$.

Multiplying each terms by 1 yields

$$\frac{X(\Delta X)}{X} = \frac{x_1(\Delta x_1)}{x_1} + \frac{x_2(\Delta x_2)}{x_2}. \tag{4.5}$$

With $\Delta X/X = \varepsilon_G$, $\Delta X_1/X_1 = \varepsilon_{L_1}$ and $\Delta X_2/X_2 = \varepsilon_{L_2}$ where $\varepsilon_G$, $\varepsilon_{L_1}$ and $\varepsilon_{L_2}$ are, respectively, the global strain, local strain of the plate and local strain of the in between regions, equation 4.5 becomes

$$\varepsilon_G X = \varepsilon_{L_1} x_1 + \varepsilon_{L_2} x_2. \tag{4.6}$$

Under an assumption of small strain (Hook's law ), the restoring forces are of the form $\varepsilon_{L_1} E_1 = \varepsilon_{L2} E_2$ where the $E_1$ and $E_2$ are the modulus of each region. The equality of

the forces here stems from the fact that two springs connected in series experience identical forces. From this, $\varepsilon_{L_2} = \varepsilon_{L1} E_1/E_2$. Thus, equation 4.6 becomes,

$$\frac{\varepsilon_{L_1}}{\varepsilon_G} = \frac{X}{x_1 + x_2(E_1/E_2)}. \tag{4.7}$$

As discussed earlier, large exposure time increases not only the layer thickness but also the stiffnesses of the PDMS surface. In this context, assumptions have been made such that $E_1 \sim t_1$ and $E_2 \sim t_2$ as the oxidation times of each region increases. Hence, equation 4.7 can be approximated as

$$\frac{\varepsilon_{L1}}{\varepsilon_G} = \frac{X}{x_1 + x_2 R}, \tag{4.8}$$

where $R \sim t_1/t_2$. When fitted to the data of Fig. 4.15, we get reasonable fit, especially in the limits of large exposure times of the boundary regions as illustrated in the inset of Fig. 4.17.

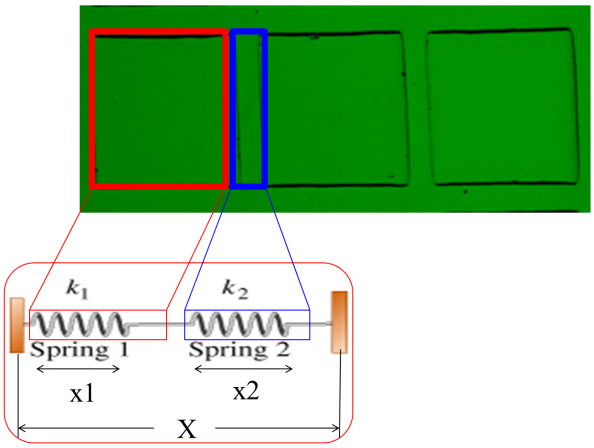


Figure 4.16. Schematics showing the different variables used in the two springs connected in series to model a simple scaling relationship between local and global strains and the ratio of the treatment time of the plates to the in between regions. The X's are the values of the pre-strain width of the plates and the in between regions.

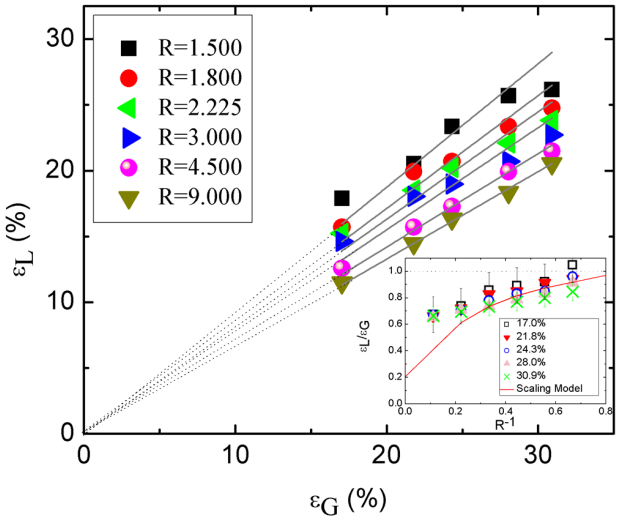


Figure 4.17. Illustration of the data in Fig. 4.15 where the inset is now fitted with equation 4.8, obtained from the simple model for $\varepsilon_{L1}/\varepsilon_G$ as a function of $R^{-1}$. It is important to mention here that when the exposure time of the boundary is small, local strain of the plate is small implying that the majority of the global strain goes to the in between soft region than to the plate. In contrast, if the boundary is treated for a long time, the plate's local strain grows since the in between plate region is now stiffer to absorb as much global strain.

### *4.3.4. Numerical Modeling*

Many researchers have demonstrated the transition of uniform undulations to localizations of thin polymer films having homogeneous stiffness experimentally [93, 23], numerically [28] and analytically [29]. These studies focused on considering thin films that are bound to substrates such as elastic and fluid substrates and characterized how the deformation profile height evolves under uniaxial stresses. These demonstrations provide a great insight for systems with a uniform stiffness and in the limit of plate-sizes approaching to infinity [28]. In fact, most recently, a group of researchers [89] have investigated the response of a laterally confined thin elastic system lying on a fluid substrate and subjected to mechanical deformation both numerically and analytically. They concluded that localization can take place in a finite sheet as well; similar to the infinitely long system, except that it takes place at a single spot in the confined sheets.

In this section, we consider - following the notion of Diamant [29] - a series of elastic sheets of plate-sizes ranging from a few micrometers to infinitely long sizes that represent, respectively, the plates in the patterned and continuous regions described in the previous sections. The aim is to numerically analyze the *effect of plate sizes* and *boundary conditions* on the buckling profiles. To this end, consider a 2D plate of length $L$, width $w$, bending modulus $B$ and bound to an elastomer foundation with effective stiffness $K$. The plate is created by curing the surface of a stretched PDMS using UV/$O_3$. The two parameters, $K$ and $B$ are related to the buckling wavelength as $K \sim E_s/\lambda$ and $B \sim \lambda^3 E_s$. When the system is uniaxially compressed along x-axis by $\Delta$, it deforms in the xy-plane. However, this deformation costs energy. The overall energetic cost of the system comes from plate bending, $U_B$, substrate deformation, $U_S$, and the work of the external horizontal force per unit length, P, as shown in Fig. 4.18. In this regard,

$$U_B = \frac{B}{2}\int_{-L/2}^{L/2} ds\dot{\theta}^2 \tag{4.9}$$

where B is the bending stiffness of the plate and $\theta$ is the angle between a tangent line at a given arc length and the x-axis as illustrated in Fig. 4.18. The dot denotes differentiation with respect to the arc length s (note that the derivative of the angle with respect to arc length gives the curvature). The foundation is assumed to consist of a large number of elastic springs tied to the plate and anchored at infinity so that they remain normal to the neutral axis of the plate as it deflects. The strain (stretching) energy stored in these springs is then given exactly by the expression

$$U_s = \frac{K}{2}\int_{-L/2}^{L/2} dsh^2, \tag{4.10}$$

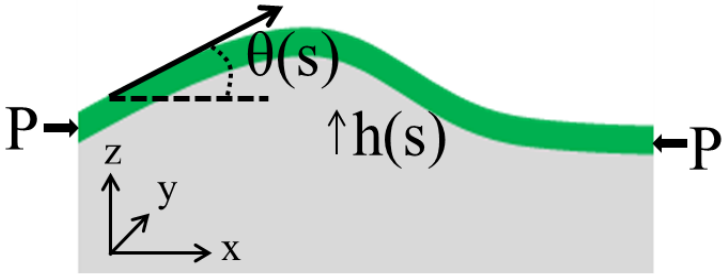


Figure 4.18. Schematic view of buckling of thin plate on an elastic foundation. The angle $\theta$ gives the position of the tangent line as a function of arc length. The deflection profile is expressed as h(s).

with K representing the substrate stiffness. The corresponding horizontal deflection, $\Delta$, of the axial load is given by

$$\Delta = \int_{-L/2}^{L/2} ds(1-\cos\theta). \tag{4.11}$$

From the geometry of the profile one can infer the relationship between deformation height and slope angular profiles as $\dot{h}(s) = \sin\theta(s)$.

The total potential energy of the system is then given as

$$U = U_B + U_s - P\Delta \tag{4.12}$$

which can further be rewritten with the help of the relation between the height and the angle the tangent line makes with x axis at a particular arc length as

$$U = \int_{-L/2}^{L/2} ds\left(\frac{B}{2}\frac{\ddot{h}^2}{1-\dot{h}^2} + \frac{K}{2}h^2 - P\left(1-\sqrt{1-\dot{h}^2}\right)\right). \tag{4.13}$$

In order to reduce equation 4.9 to $h(s)$ dependence, the advantage of geometrical relation, $\dot{h}(s) = \sin\theta(s)$, is considered. Differentiating both sides with respect to the arc length ($\ddot{h}(s) = \cos(\theta)\dot{\theta}(s)$) and considering $\cos(\theta) = \sqrt{1-\sin^2\theta}$ yield $\dot{\theta}^2 = \ddot{h}^2/(1-\dot{h}^2)$.

Minimizing the functional in equation 4.13 with respect to h(s) and setting it equal to zero ($\delta U = 0$) yields the deformation height profile, h(s), at equilibrium for a particular compressional displacement, Δ. The result of the minimization gives

$$Khd^3 + B\left(\dddot{\dddot{h}}d^2 + 4\dot{h}\ddot{h}\dddot{\dddot{h}}d + \ddot{h}^3 d - 4\dot{h}^2\ddot{h}^3 d + 8\dot{h}^2\ddot{h}^3\right) + P\ddot{h}d^{3/2} = 0, \tag{4.14}$$

where $d = 1 - \dot{h}^2$. Rearranging equation 4.14 yields:

$$\dddot{\dddot{h}} = \frac{4\dot{h}^2\ddot{h}^3}{1-\dot{h}^2} - \left(\frac{K}{B}\right)h\left(1-\dot{h}^2\right) - \frac{4\dot{h}\ddot{h}\dddot{\dddot{h}}}{1-\dot{h}^2} - \frac{\ddot{h}^3}{1-\dot{h}^2} - \frac{8\dot{h}^2\ddot{h}^3}{\left(1-\dot{h}^2\right)^2} - \left(\frac{P}{B}\right)\frac{\ddot{h}}{\left(1-\dot{h}^2\right)^{1/2}}, \tag{4.15}$$

After rewriting the fourth order differential equation in (4.15) as four systems of first order differential equations (see Appendix A), it is possible to solve for the deformation profile ($h(s)$) numerically by providing appropriate boundary conditions. In this regard, four boundary conditions are required for both the continuous and patterned regions. The boundary conditions used for the continuous systems were: $h(-L) = h(L) = constant$, $\dot{h}(-L) = \dot{h}(L) = 0$. In the patterned regions, different boundary conditions were required for the connected and unconnected plates, as expected. For the connected plates: $h(-L/2) = constant$, $h(0) = h_0$, and $\dot{h}(-L/2) = \dot{h}(0) = 0$. Similarly, for the unconnected plates: $h(-L/2) = constant$, $h(0) = -h_0$, $\dot{h}(0) = 0$ and $\ddot{h}(-L/2) = 0$. In both connected and unconnected plates, the assumption that the profile is even ($h(s) = h(-s)$) as observed in our experiment, is taken into account (i.e. the integration is made from -L/2 to 0 and followed by reflection due to symmetry). The *constants* and $h_0$ are supplied from experimental outcome.

In all the cases, there is remarkable agreement between the data obtained from experiment and numerical modeling, especially in the low strain limit. As confinement

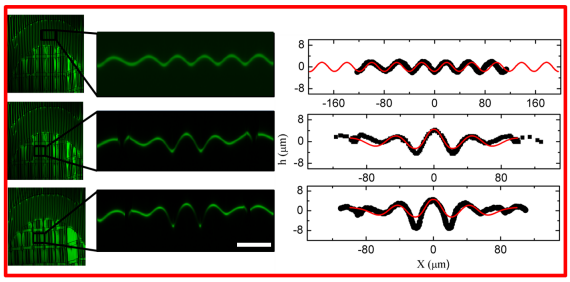


Figure 4.19. Comparisons of the experimental (black) and numerical modeling (red) of the deformation height profile, h(x), of the ring region and connected plate under mechanical strains of 19.72%, 22.38% and 28.15%, respectively. Note the experimental and numerical data are not matching for the bulk region (top right). That is because the $L$ for the numerical is set to a large number to account for the unbound plate for the bulk compared to the experimental data which is constrained by the image size captured. The scale bar represents $20\mu$m.

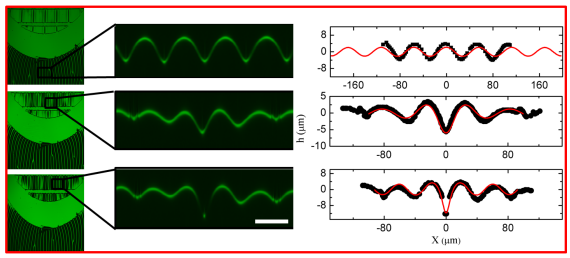


Figure 4.20. Comparisons of the experimental (black) and numerical modeling (red) of the deformation height profile, h(x) of the bulk region and unconnected plate under mechanical strains of 19.72%, 22.38% and 28.15%, respectively. Note that the experimental and numerical data are not matching for the ring region (top right). That is because plate length is set to a large number to account for the unbound plate for the ring compared to the experimental data which is constrained by the image size captured. The scale bar represents $20\mu$m.

increases, the fitting starts to deviate for the connected plates. This might be due to the broken symmetry in the localization of connected plate.

## 4.4. Summary

In this chapter, the mechanical response of idealized inhomogeneous elastic sheet with patterned regions of different thicknesses and stiffnesses, to mechanical deformation is studied. The idealized/patterned surface layers are created by selective ultraviolet/ozone

(UV/$O_3$) treatment of the top surface of polydimethylsiloxane (PDMS) using TEM grid mask. By controlling the exposure time of the UVO, samples ranging from continuous thin films to sets of isolated small plates were created. Large exposure time increases not only the stiffness of the PDMS surface but also the thickness of the silicate layer ($SiO_x$) created. Our results indicate that the amplitude of the continuous regions (bulk and ring) grow according to A$\sim \varepsilon^{1/2}$ while that of the plates, both connected and unconnected, show monotonically increasing amplitudes, while no significant difference was observed in the wavelengths of each region. Although uniform undulation occurs in both the continuous and patterned regions, in the limit of small strains, high localization is observed only in the confined small plates, as opposed to the continuous regions. For a better understanding of how the buckling profiles of isolated plates are affected by a change in the boundary conditions, local strains of plates have been monitored. A simple scaling model which consists of two springs having spring constants $k_1$ and $k_2$ representing, respectively, the plate and the in between plates have been developed which reasonably fit our experimental observation, especially in the limits of large exposure times of the boundary regions. By creating variable boundary conditions of the plates, the deformation height profile has also been estimated through numerical modeling.

# 5. THE BUCKLING OF COLLOIDAL LAYERS

## 5.1. Background

This chapter focuses on the responses of discrete systems (colloidal layers) to mechanical deformations. Combined experimental methods and theoretical modeling will be exploited for the better understanding of the responses. Experimentally, the colloidal layers are made on a freshly cleaved mica from polystyrene and silica particles of variable sizes (diameters ranging from $3nm$-$10\mu m$) and transferred to an elastic substrate, polydimethylsiloxane (PDMS) before subjected to a compressive stress. The buckling profiles measured, when the system is under compression, demonstrate a great insight that the continuum model may not be able to predict such discrete systems. Theoretically, a granular model is constructed and structural stability analysis was investigated in both the pre-buckling and post-buckling regimes in order to predict the experimental observations. The agreement of the experimental and theoretical observations is remarkable. In the following sections, a brief review of continuum model (in the limit of small strain), the experimental methods, summary of the theoretical modeling, and the results found will be presented.

### *5.1.1. Continuum Model*

Continuum model, in this context, refers to the model developed to describe the responses of continuum thin films to mechanical deformation [110]. In the continuum model, as discussed in the previous chapters, a thin film bound to an elastic substrate

[0]The work in this chapter is done in collaboration with Antoinette Tordesillas and David Carey. Andrew Croll and Bekele Gurmessa designed and conducted the experiment in close cooperation whereas the numerical modeling was done independently by Antoinette Tordesillas and David Carey. The work in this chapter is published in refs. [24, 116].

undergoes an in-plane deformation until a threshold strain is attained when subjected to compressive stress. As compression increases beyond the threshold, the film will buckle out of plane forming a repetitive sinusoidal pattern (also known as surface wrinkling) [110, 20]. The mechanism behind the formation of periodic surface buckling instabilities lies in the competition between bending energy of the thin film and stretching energy of the foundation. Minimization of the total energy yields intermediate (critical) pattern spacing, given as [110, 20, 63]

$$\lambda_c = 2\pi h(\bar{E_f}/3\bar{E_s})^{1/3}, \tag{5.1}$$

where $h$ is the film thickness and $E_{f(s)}$ is the reduced film (substrate) modulus; while the buckling amplitude is given as

$$A = h(\varepsilon/\varepsilon_c - 1)^{1/2}, \tag{5.2}$$

with $\varepsilon$ and $\varepsilon_c$ being the applied strain and the threshold strain, respectively.

Many previous experimental studies have demonstrated that, once buckled out of plane, the buckling wavelength and amplitude evolve as illustrated in Fig. 5.1 and Fig. 5.2 [110, 20, 63]. As shown in Fig. 5.1, the sample remains flat at low strains and then increases non-linearly beyond the critical strain. Similarly, the data in Fig. 5.2 demonstrate that the buckling wavelength increases monotonically with film thickness while the modulus of the film remains unchanged for film thickness greater than $\sim 100nm$. These experimental observations were qualitatively predicted through the continuum models shown in equations 5.1 and 5.2. Specifically, the threshold wavelength of wrinkling is directly proportional to the film thickness and the cubic root of the ratio of the elastic moduli of the film and substrate, respectively whereas the buckling amplitude is not explicitly dependent on material properties. The natural question that arises is whether the continuum model can predict the buckling of a discrete system as well. Throughout

this chapter, we are guided by the following questions: First, can a continuum model really predict the response of a particle layer (discrete system)? Second, how would the wavelength and amplitude of the buckling instability in the discrete system depend on the size of the colloids, the modulus of the colloids, and the strain imposed on colloidal layers? Third, is it possible to numerically model and predict the experimental observations?

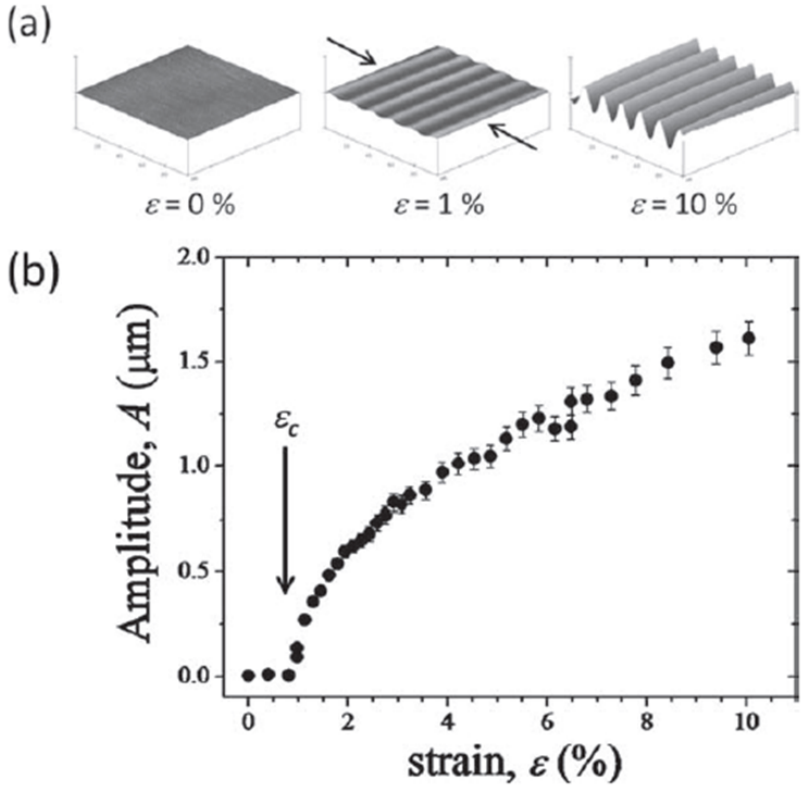


Figure 5.1. Demonstration of AFM to detect both the critical strain for wrinkling as well as the amplitude of the wrinkle pattern. a) AFM images showing the transition from a flat film to a wrinkled surface as compressive strain is increased. b) Amplitude as a function of applied strain, showing both the critical strain and the amplitude increasing non-linearly with strain. Adapted by permission from [20], copyright (2011) Macmillan Publishers Ltd.

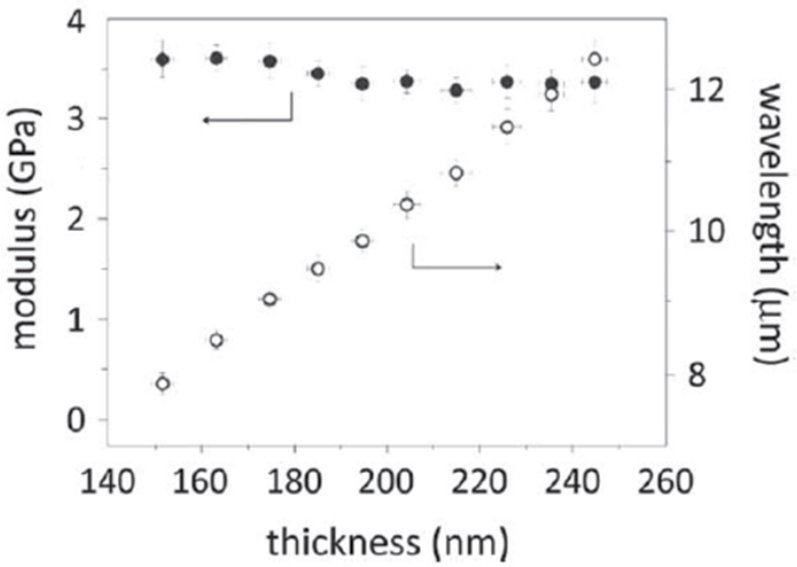


Figure 5.2. Illustration of the wrinkling wavelength and stiffness of polystyrene film as a function of film thickness. Adapted by permission from [20], copyright (2011) Macmillan Publishers Ltd.

## 5.2. Experimental Procedures

### *5.2.1. Substrate Preparation*

Elastic substrates were formed with a commercial two part polydimethylsiloxane (PDMS) elastomer (Sylgard 184, Dow Corning) in different weight ratios. The cured PDMS has fair adhesion to the colloidal particles and its modulus can be easily controlled over several orders of magnitude by mixing various ratios of polymer and prepolymer. After mixing, the PDMS is poured into a form such that many 1 cm $\times$8 cm $\times$0.5 cm pieces were fabricated in each batch. Forms were placed in a vacuum oven, degassed, and annealed at 70$^{\circ}$C for 1 hour and subsequently aged an additional 12 hours before use.

### *5.2.2. Formation of 2D Arrays of Colloidal Spheres*

Two-dimensional colloidal monolayers were formed on freshly cleaved mica substrates through a typical drop drying method from colloidal solutions created by mixing

dry colloids with pure (Milli-Q) water [27]. Colloids shipped in water solution were used as received. Occasionally, samples were cooled in a refrigerator in order to slow down the water evaporation and crystal formation process. In order to make the two dimensional layers, a drop or two of the colloidal suspension is dispensed on a clean, freshly cleaved mica sheet and kept in a room temperature environment until all the water evaporate (at least for about 24 hours). When water evaporates from the colloid suspension, the colloids remain behind often making a hexagonally packed layer as shown in Fig. 5.3. The figure shows snapshots of drying colloidal solutions at different times as captured by optical microscope (a and b). After fully dried, the particle monolayer is transferred to a PDMS substrate by light compression and imaged by a high resolution confocal microscopy as shown in Fig. 5.3(c). The removal of the mica sheet during the transfer is aided by putting a drop of milli-Q water at the PDMS/mica contact line. Once again, after transferred to the PDMS substrate, the sample is allowed to dry at room temperature before mechanical compression is imposed.

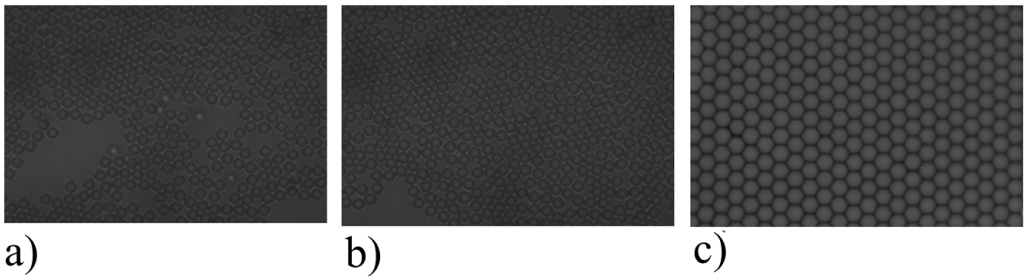


Figure 5.3. Snapshots of a drying $3.2\mu m$ monodispered polystyrene colloidal spheres at a) early stage, b) intermediate stage and c) after fully dried as captured by optical microscopy and confocal microscopy respectively. During the early and intermediate stages the colloids are unstable and move around until the water is evaporated. After the water is fully evaporated the colloids remain behind making nice hexagonally packed colloidal layers.

### *5.2.3. Mechanics*

Once transferred to a pre-strained PDMS as described in the previous subsection, a home-made strain-stage is used to apply a compressive stress in the composite of the film and substrate as indicated in Fig. 5.4. Fig. 5.4(a) shows a film made of colloids of diameter $3.2\mu m$ loaded on to a pre-strained PDMS substrate mounted on a strain stage. At this point, the sample is free from any strain and hence it remains a perfectly ordered, hexagonally packed monolayer (see Fig. 5.4(b)). When the composite of the monolayer and the soft foundation is compressed to a strain that exceeds a critical value, despite the absence of bending energy, the layer responds by making a uniform undulation. This is shown in Fig. 5.4(c) for the same sample as in part (b) but under a strain of 10.43%. In all of the experimental measurements in this chapter, image acquisition is made through the use of Olympus Flouview 1000 laser scanning confocal microscopy to trace the positions of each particle in three dimensions that enabling the measurement of accurate peak-valley (amplitude) and peak-peak (wavelength) positions.

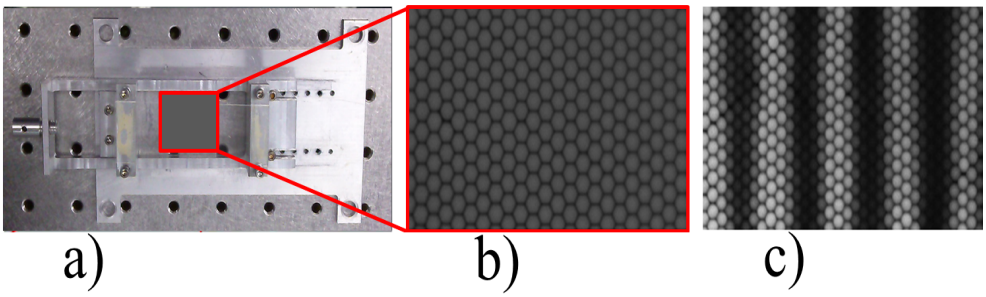


Figure 5.4. a) Photograph of the mechanical strain stage used in these experiments. The stage compression is driven by a motor (Left of image), and a PDMS substrate is shown clamped into the stage. The highlighted region shows a typical sample. b) A Laser Scanning Confocal Microscope (LSCM) image of an uncompressed monolayer particle (radius $R$=1.6 $\mu$m polystyrene spheres). c) The same particle layer under a compressive strain of 10.4%, showing out-of-plane buckling.

## 5.3. Modeling

In order for forces to be transmitted from one particle to the next in a granular materials, there must be contacts between the particles. Granular materials refer to collections of macroscopic particles such as sand piles, which are visible to the naked eye. Over the past few decades, researchers have observed that, when subjected to load, the majority of particles in a granular material carry less than the average force [92, 131]. The particles bearing forces less than the average load are termed 'the weak networks'. The weak network particles surround and provide lateral stability to another group of particles which form strong network of forces and carry above average load. The strong network of forces are carried through chainlike particle groups referred to as force chains. Consider a force chain model consisting of $N+2$ chains of identical spherical particles, each of radius $R$. The chain of particles, here assumed to be bound to an elastic foundation, is subjected to compressive force. Figure. 5.5(a) is a schematics of undeformed initial configuration of a thin monolayer bound on a very thick elastic substrate. When subjected to uniaxial compressive force, the particle layer will be constrained not only to the axially applied force but also to the forces and moments stemming from the interactions between the particles. As a consequence, the total potential energy stored in the buckled particle layer (see Fig. 5.5(b)) is described by the summation of energy contributions from: the lateral support of the elastic foundation, the tangential (sliding) force between two neighboring particles, the contact (rolling) moment that occur between two neighboring particles, and from the work done by the applied axial load $F$. Mathematically, the total potential energy function for the complete system is given as

$$V = \frac{k^f R^2}{2} \sum_{i=0}^{N+1} q_i^2 + \frac{k^s}{2} \sum_{i=0}^{N} d_i^2 + \frac{k^r R^2}{2} \sum_{i=0}^{N} \psi_i^2 - F \sum_{i=0}^{N} \Delta_i, \tag{5.3}$$

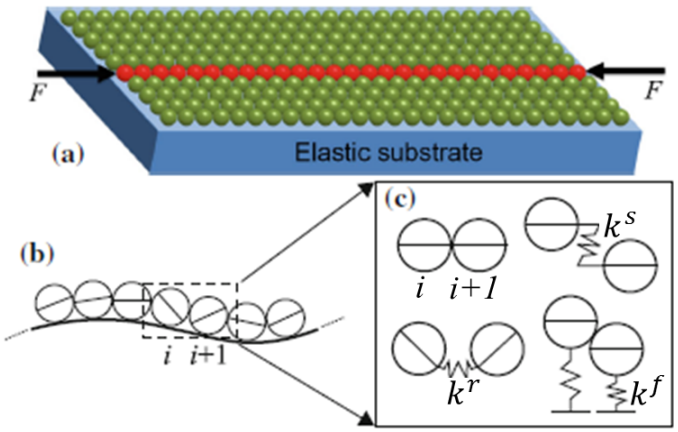


Figure 5.5. Illustration of a) initial undeformed configuration of thin monolayer on a very thick substrate (only top part depicted), showing particle chain in layer under axial compression. b) Buckled configuration of chain showing adjacent particles $i$ and $i+1$. c) From top left in clockwise direction: particles $i$ and $i+1$ in initial undeformed plane, and spring resistances to relative particle displacement (sliding) in direction tangential to the contact plane, vertical displacement from undeformed axis of chain (due to the elastic foundation), and relative particle rotation (rolling), shown with relevant spring stiffness parameters $k^s, k^f, k^r$, respectively.

where the stiffness parameters, $k^f, k^s, k^r$ denote, respectively, 1.) the resistance to out of plane deformation by the elastic foundation, 2.) the resistance to sliding (tangentially) between the contact particles and 3.) the resistance to rolling (again tangentially) between the contact particles as depicted schematically in Fig. 5.5(c). Furthermore, the tangentially sliding distance, the rolling angle between consecutive particles ($i$th and $(i+1)$th) and the axial compressional displacement (end-shortening) are denoted, respectively by

$$d_i = R\left[2\arcsin\left(\frac{q_{i+1}-q_i}{2}\right) - \omega_{i+1} - \omega_i\right], \tag{5.4}$$

$$\psi_i = \omega_{i+1} - \omega_i, \tag{5.5}$$

$$\Delta_i = 2R\left(1-\sqrt{1-\left(\frac{q_{i+1}-q_i}{2}\right)^2}\right). \tag{5.6}$$

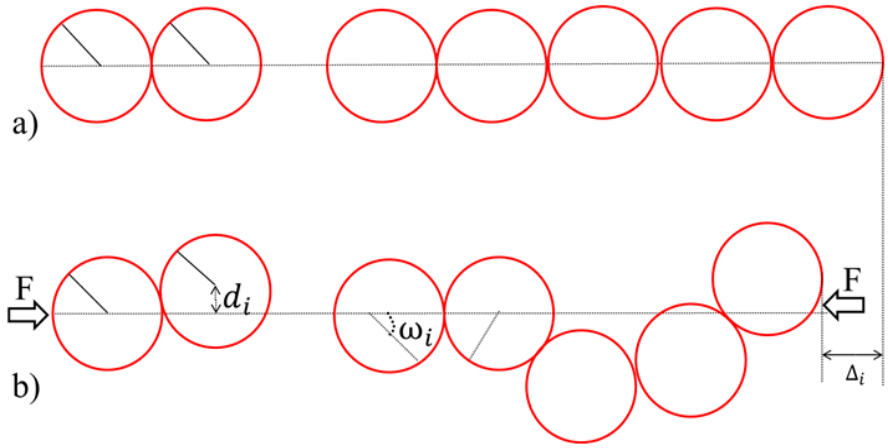


Figure 5.6. Depiction of the undeformed a) and deformed b) configurations of a force chain showing the variables defined in equations 5.4, 5.5 and 5.6. Note that the measurement is made with respect to the undeformed doted axis.

In order to determine the critical buckling wavelength (mode), the authors exploit linear analysis approach. Notably, by performing the necessary substitutions and taking first-order expressions for the arcsines in the sliding distance between adjacent particles, $d_i$ and the square roots in the axial compression displacement (end shortening) during deformation, $\Delta_i$, shown in equations 5.4 and 5.6, the linearized potential function becomes:

$$V_{\text{lin}} = \frac{1}{2}k^f R^2 \sum_{i=0}^{N+1} q_i^2 + \frac{1}{2}k^r R^2 \sum_{i=0}^{N} (\omega_{i+1}-\omega_i)^2 + \frac{1}{2}k^s R^2 \sum_{i=0}^{N} (q_{i+1}-q_i-\omega_{i+1}-\omega_i)^2 - \frac{1}{4}FR\sum_{i=0}^{N}(q_{i+1}-q_i)^2 \tag{5.7}$$

$$\equiv V(q_0, q_1, ..., q_{N+1}, \omega_0, \omega_1, ..., \omega_{N+1}). \tag{5.8}$$

By introducing the unknown parameters $q_i$ and $\omega_i$ as diagonalizing transformations or Fourier modes (which produce a set of $N$ orthogonal modes with wave number $m$ and amplitudes $u_m$ and $\phi_m$ )

$$q_i = \sum_{m=0}^{N+1} u_m \sin\left(\frac{im\pi}{N+1}\right), \tag{5.9}$$

$$\omega_i = \sum_{m=0}^{N+1} \phi_m \cos\left(\frac{im\pi}{N+1}\right), \tag{5.10}$$

the linearized potential energy has been written in another form as a function of the modal amplitudes $u_m$ and $\phi_m$:

$$W = W(u_1, ..., u_N, \phi_0, \phi_1, ..., \phi_{N+1}). \tag{5.11}$$

Obtaining a diagonalized form of the potential function ($W$) with $N$ degrees of freedom by providing appropriate boundary conditions (pin-ended boundary condition such that $q_0 = 0$ and $q_{N+1} = 0$ which are satisfied by equation 5.9) allows for the elimination of $u_0$ and $u_{N+1}$ in equation 5.11. The second derivative of the diagonalized function (potential) with respect to the modal amplitudes ($u_m$), results in $N$ stability coefficients. The critical load, $F_m^C$ was obtained by setting the stability coefficients to be zero from which the corresponding characteristic buckling mode ($m_{min}$) and hence the wavelength ($\lambda = 2(N+1)/m_{min}$) were obtained.

In order to further examine the behavior of buckling under the limit of large strains (in the post buckling regime), the non-linearized potential function defined in equation 5.3 was solved with AUTO (a non-linear-solver) [116]. As a result, the post buckling configurations were determined. In the post buckling regime, the buckling profiles (amplitude and wavelength) as a function of strain were calculated for a fixed stiffness constants of ($k^f = k^s = k^r = 400$) $kN/m$ as opposed to the variable stiffnesses considered

in the pre-buckling regime. The reason behind the choice of these stiffness constants to be identical is that both the sliding and the rolling distances are not negligible as compared to the vertical displacement (note that in the linear-analysis the spring constants for the contact forces were bigger than that of the foundation; but here all are set to be the same.). This value is chosen to be in the same order as the experimentally measured Young's modulus.

## 5.4. Results and Discussion

Despite the absence of bending energy, the colloidal layers buckle out of plane, forming a sinusoidal topography - a behavior typical of an elastic, continuum plate (see Fig. 5.4(c)). In order to study the differences and similarities between how continuum and discrete films respond to imposed compressive stress, we focus on measuring two emerging length scales: the buckling wavelength and amplitude.

### *5.4.1. Buckling Wavelength*

When subjected to a uniaxial stress, similar to the continuum system, the colloidal particle layer also responds by making periodic patterns. A typical sample response under compressional stress is shown as in Fig. 5.4(c). The figure shows a 3D laser scanning confocal microscopy image of a sample under a compressive strain of 10.4%. From the 3D images, each particle is located in 3D space. The buckling wavelength is measured from peak-to-peak of the buckled sample in the compression direction and is denoted by $\lambda$. The data presented in Fig. 5.7(a) demonstrates the evolution of the wavelength of the colloidal layer made of both silica and polystyrene particles as a function of the applied strain. The buckling wavelength in all the samples considered here decrease monotonically with increasing compression. Furthermore, colloidal layers made from colloids with larger size not only have longer wavelength but also require larger applied strain in order to buckle (see the left hand side of Fig. 5.7). This clearly shows that the different colloids

have different onset of buckling strain, as expected. How are these buckling wavelengths compared with the continuum model's prediction ?

### *5.4.2. Comparison with Continuum Model*

The buckling wavelengths presented in Fig. 5.7 (left) were obtained from the responses of colloidal layers made from polystyrene and silica - particles with significantly different material properties. When scaled by the particle size (diameter), however, the data collapses to one master curve as indicated in Fig. 5.7 (right). It is important to note that particles of significantly different modulus (polystyrene and silica) also collapse onto one master curve. This phenomenon has an implication that the buckling wavelength in the discrete system is independent of the modulus of the particles. In order to connect this observation to the continuum system, an assumption that the modulus of a continuum film is associated with the modulus of particles in the colloidal layer is considered. Under this assumption, our observation (see Fig. 5.7 (right)) and the prediction of continuum theory ($\lambda \sim E_f^{1/3}$ (f denotes film)) are compared, which clearly show that there is no agreement between the two. Another sign of the fact that continuum theory my not be able to predict the discrete system appears when the buckling wavelength is plotted as a function of Young's modulus and the substrate modulus is varied. To this end, the buckling wavelength of a set of particle layers bound to substrates which vary with an order of magnitude have been measured. Our result indicates that the wavelength remains essentially constant (see Fig.5.8). This result also reveals the fact that our observation disagrees with the continuum theory's prediction which states that the buckling wavelength varies as $\lambda \sim E_s^{-1/3}$ (s denotes substrate). Finally, when the buckling wavelength is plotted as a function of the size (diameter) of each particle, the data collapses to a linear curve as can be seen from Fig. 5.8 (right). This has an implication that the underlying mechanism is granular (discrete such that the particles are undeformable ) in nature not continuum.

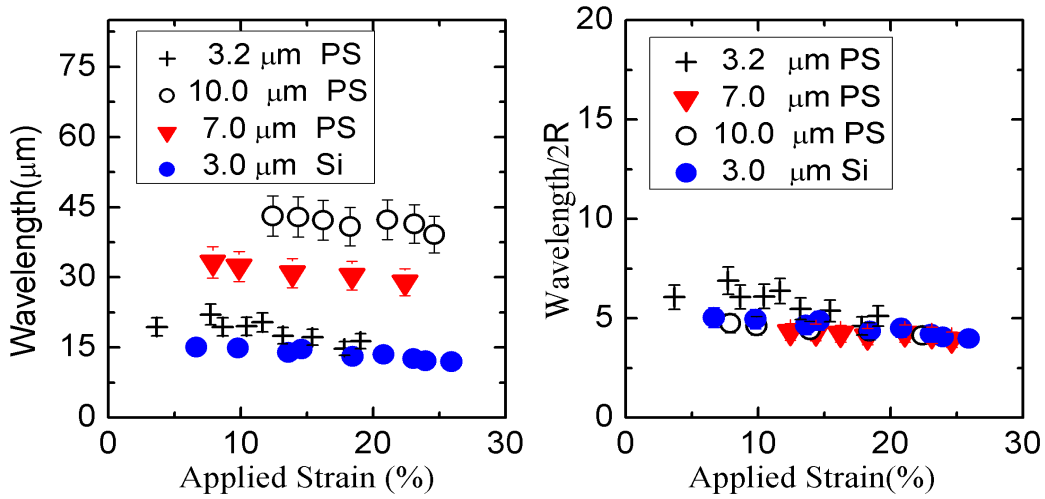


Figure 5.7. Evolution of the buckling wavelength as measured for several particles (left) and scaled by particle size (right) as a function of applied strain. When the average of the normalized wavelengths in (right) is extrapolated to the zero strain limit, it yields a value that corresponds to a normalized critical wavelength ($5.3 \pm 0.4$). Notice that the data collapse to one master curve when scaled by the diameter of each colloid implying that the wavelength is independent of the material properties like Young modulus of the colloids.

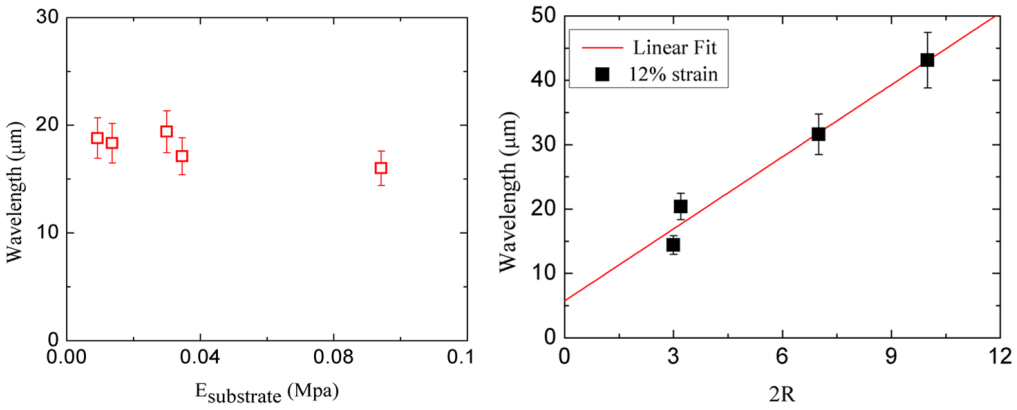


Figure 5.8. Critical wavelength (obtained by extrapolating the measured wavelengths to zero strain) as a function of substrate modulus (left). It shows that the wavelength remains the same, though the modulus is varied by an order of magnitude. Compare this with $\lambda \sim E_s^{-1/3}$ as predicted by continuum theory. The figure to the right hand side is wavelength as a function of 2R; an example showing the dependence of the buckling wavelength on the radii of the colloidal particles at a particular applied compressive strain (12%); and has a slope of 4).

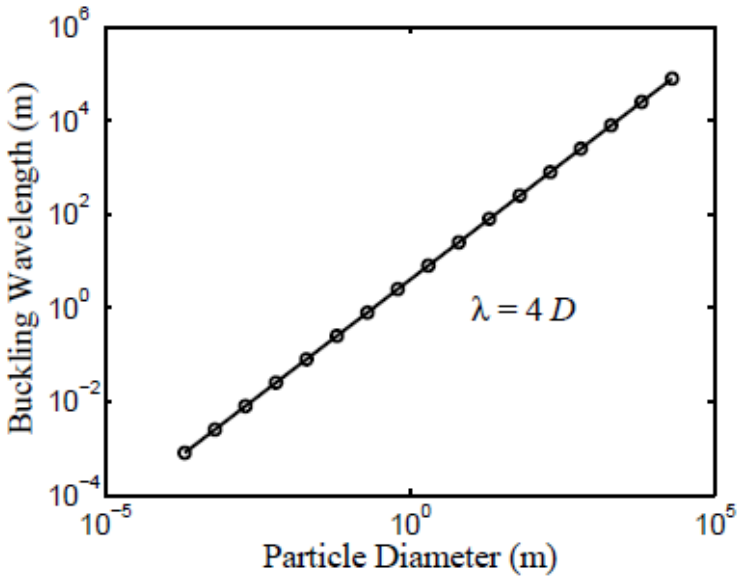


Figure 5.9. Model prediction of the variation of the buckling wavelength as a function of particle diameter. The wavelength shows linear dependence on the particle size as shown experimentally in Fig. 5.8. Adapted from [116].

A direct comparison of an experimental observation and a numerical modeling of critical wavelength varying with the diameter of the particles are shown in Fig.5.8 (right) and Fig.5.9. In order to measure the critical wavelength experimentally, a monolayer of colloidal particles is considered. While varying the applied strain, we closely monitor the response of the sample under a microscope. The critical wavelength is measured from a micrograph captured when the sample buckles out of plane for the first time as it becomes optically visible. On the other hand, the full potential function is differentiated twice to find the critical buckling force from which a minimum buckling mode and critical wavelength is found. As shown in the figure, the two have remarkable matching.

### *5.4.3. Buckling Amplitude*

When performing buckling experiments, it is essential to give close attention to the mode of deformation: elastic deformation or plastic deformation. In particular, when dealing with significantly sensitive material systems like our thin films, it is possible that

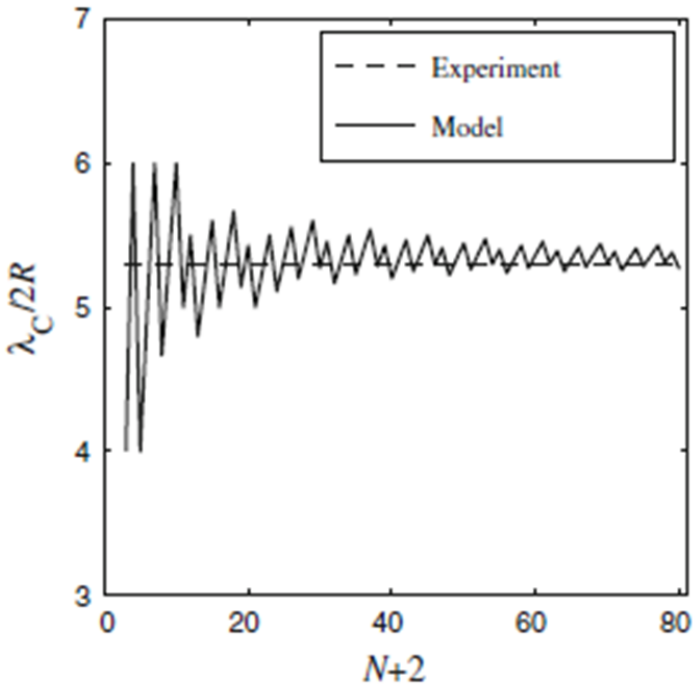


Figure 5.10. Model prediction of the critical buckling wavelength as a function of chain length. The wavelength initially shows oscillation but rapidly decays as the chain length increases implying the linear dependence of the particle size as shown experimentally in Fig. 5.8 (right). Adapted from [116].

plastic deformation can take place easily. In this regard, we consider a strain loop (forward and reverse) and measure the buckling wavelength and amplitude. When strain is increased gradually, the resulting amplitudes and wavelengths of the colloidal layers take the form of Fig. 5.11 (denoted by red color). Reversing the direction of the strain to zero or unloading does not incur change in the peak-valley or spacing of the patterning as shown by the overlapping data in Fig. 5.11; revealing the absence of hysteresis in the loading/unloading deformation processes. This indicates that the deformation during the forward and reverse loading in the buckling wavelength and amplitude is under purely elastic deformation, not plastic deformation.

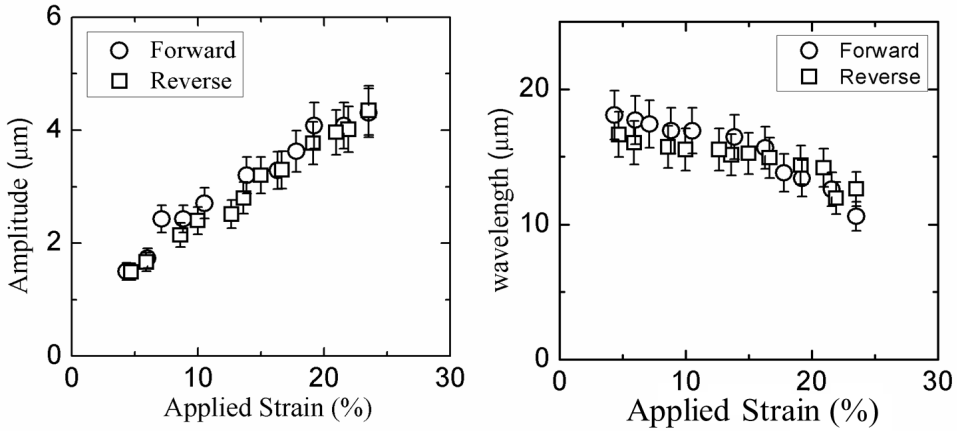


Figure 5.11. Experimental results of a) amplitude b) wavelength as a function of the forward and reverse direction of applied strain of $3.2\mu$ of polystyrene sphere. There is little effect of hysteresis loop in both cases. This observation has an implication that the material is not undergoing plastic deformation in the range of our applied strain. Adapted from [24].

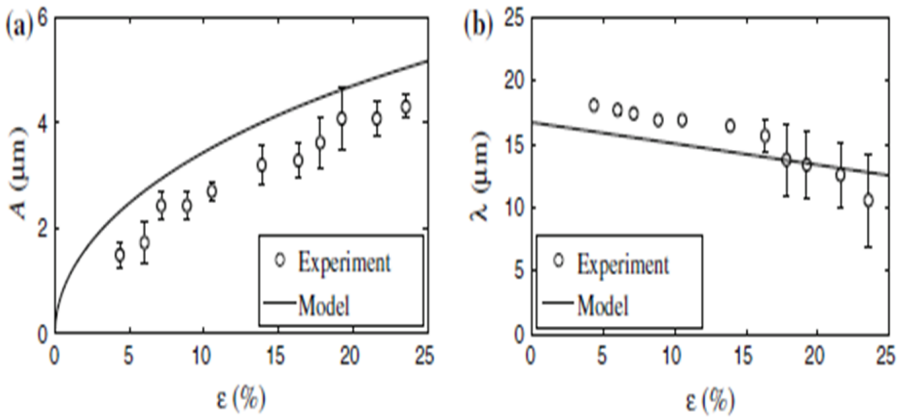


Figure 5.12. Comparison between experimental observation and model predictions of the buckling amplitude and wavelength of particle system. In our experiment, polystyrene colloids of diameter $3.2\mu m$ were considered as shown in the forward strain loop where as the model prediction was made for N+2 = 35 particles. Adapted from [116].

### *5.4.4. Model Versus Experiment*

Our experimental observations and theoretical predictions show good agreement in capturing the essential features of investigated systems. Specifically, our experimental observation of the collapsing threshold wavelength normalized by the size of the particles illustrated in Fig. 5.7 (right) was verified through the numerical modeling conducted independently by our collaborators (see Fig. 5.10). They used the physics of force chain buckling as presented in detail in references [24, 116] and summarized above. The result of the threshold buckling wavelength was calculated for variable stiffness constants ($k^f = 400, k^s = 1,100$ and $k^r = 1,000) kN/m$. These values were chosen based on the fact that the relative slips and rotation of neighboring particles in the experiment were assumed to be insignificant compared to the large vertical displacement implying that the spring constants for the contact forces are large compared to the resistance of the lateral foundation. As can be seen in Fig.5.10, there is good agreement of the threshold wavelength with our experimental observation. It is noteworthy that the threshold wavelength, although it oscillate for small chain lengths, rapidly approaches a finite value as the chain length increases.

The monotonically increasing (decreasing) of the buckling amplitude (wavelength) observed in our experimental measurements were also predicted to be in a reasonable agreement with the numerical modeling. In contrast to the linear-regime, the buckling profiles (amplitude and wavelength) plotted as a function of strain in Fig. 5.12 were calculated for a fixed stiffness constant of ($k^f = k^s = k^r = 400$) $kN/m$ in the post-buckling regimes. Although not perfectly matching, there is qualitative agreement between the model and the experimental observation as presented in Fig. 5.12. The small deviation observed between the experimental and numerically predicted amplitude is attributed to the differences in the substrates used in the two approaches: experiment and model. In the former, the substrate used is made from elastic continuum (PDMS) while in the later,

it is made from discrete springs. As a result, the continuum substrate will drive down the buckling amplitude more than the spring stiffness does.

## 5.5. Summary

In this chapter, the response of colloidal particle layers to mechanical deformation was studied by a combination of experimental and theoretical methods. Experimentally, micron scale colloidal particles bound to an elastic foundation were subjected to a uniaxial stress. Beyond a threshold strain, the layer undergo out of plane buckling by forming periodic undulations similar to wrinkling in the continuum system. As a result, several observations have been made: 1.) the buckling wavelength is independent of the modulus of the particles studied, 2.) the threshold buckling wavelength and the radius of the particles are directly proportional and 3.) the threshold wavelength normalized to the size of the particles relaxes to a finite value ($\lambda_C/2R \sim 5.3 \pm 0.4$) as the applied strain increases. These observations provide great insights leading to the sign of failure of continuum theory to predict discrete systems. Theoretically, a granular model of this system was considered. In the model, structural stability analysis in both small and large stain limits were employed to predict the results observed experimentally. Specifically, by considering the small strain limit (linear-analysis), the threshold buckling wavelength observed experimentally ($\lambda_C/2R \sim 5.3$) has been remarkably predicted. On the other hand, by analyzing the large strain limit (non-linear analysis to post-buckling regime), both the buckling wavelength and amplitude evolutions as a function of increasing strain were also successfully predicted by the model which again is qualitatively in fair agreement with the experimental observations.

# 6. CONCLUSION

In this chapter, a brief summary of the entire thesis will be provided. This thesis focused on understanding the response of nanoscale polymer films to mechanical deformation. In order to realize this goal, surface elastic instability is exploited. An elastic instability is useful in creating localized deformation in nanoscale films through bending. Through the application of this method, we were able to: 1.) develop a novel strategy for characterizing the response of nanoscale films to mechanical deformation, 2.) investigate how microstructural orders in self-assembled block copolymers contribute to yield strain, 3.) demonstrate how idealized, spatially non-homogeneous thin films respond to mechanical deformation and 4.) show that continuum theory fails to predict the buckling of discrete systems (colloidal particles).

In chapter 2, we developed a novel method of quantifying the strain at which a nanoscale polymer film starts permanent deformation. For a bulk material, the conventional method of measuring such deformation is through instron tensile/compression test. This method is not applicable for nanoscale films for two main reasons: first, the tensile test requires the test specimen to be in a bulk form in order to fit to the grips, and second, the nanoscale films are so sensitive that they can break very easily during the process. In our approach, the specimen is not required to be thick. Thus, even very delicate specimen which is as thin as 10 nm, can be processed through the current approach due, in part, to the support it gets from the substrate. The composite of film and substrate is subjected to uniaxial compression until part of the film debonds from the substrate. After debonding, it is possible to measure the width and height of the delamination of a micrograph through optical sectioning of confocal microscopy. Finally, knowing the width and amplitude, together with the thickness of the film, which can be measured using AFM, will enable to measure the surface strain via Euler buckling theory. The yield strain for the onset of

permanent deformation corresponding to the surface strain beyond which no permanent deformation.

Next, using lessons from the technique we developed in the study of the response of homopolymer to mechanical deformations, coupled with our quest to examine the mechanical response of more complex material system, another experiment has been designed to investigate how the onset of strain is affected by the microstructural orders formed when block copolymers undergo the self-assembly processes. To this end, poly (styrene-b-divinylpyridine) (PS-b-P2VP) has been chosen as our model material. Thin films made from this block copolymer has the ability to self-assemble into well-aligned lamellar domains parallel to the substrate if the total film thickness is commensurate with the step height $L_0$. For a better understanding of the response of such films to mechanical deformation, we first studied how the individual blocks (PS and P2VP) constituting our model material (PS-b-P2VP) respond to mechanical deformations followed by how both the as cast and self-assembled films made from PS-b-P2VP respond. Poly(2-vinylpyridine) (P2VP) shows similar behavior to the yield strain of PS films. Notably, both polymers have flat yield strain in the bulk region and dramatically increase as confinement increases. However, some differences exist between the yield strains measured for PS and the P2VP. There is noticeable upward shift of the yield strain in P2VP as compared to PS. This has an implication that thin films made from P2VP can stretch further before failure as compared to PS films. Our measurements in the yield strains of both the as cast and ordered PS-b-P2VP are also consistent with the yield strain of polystyrene we measured. The results are significant in three aspects: 1.) the trend of the yield strain follows the same pattern as the function of confinement (see Fig. 3.11), 2.) the up turning of the yield strains start nearly at about the same film thicknesses ($\sim$ 100 nm) and increases significantly with increasing confinement, and 3.) the yield strain occurs at much lower strains, of the order of 0.1%. In addition, self-assembled PS-b-P2VP films and films decorated with terraces (islands,

holes and bi-continuous) show higher yield strain as compared to as cast PS-b-P2VP and polystyrene films, suggesting that the microstructure significantly increase the failure strain of the films. This implies that films with microstructural orders require high strain to break. It is essential to emphasis here that such measurement has implications for many current experimental investigations of the elastic properties of thin polymer films, particularly in experiments attempting to probe the far from threshold elastic behavior.

The use of idealized/patterned surface layers created by selective ultraviolet/ozone treatment of the top surface of polydimethylsiloxane (PDMS) using TEM grid mask was a good approach to characterize the response of non-homogeneous system to mechanical deformations. This approach creates variable strain fields in the materials. In this project, by controlling the exposure time of UV/O3, we created samples ranging from continuous thin films to sets of isolated small plates and observed that the continuous regions form isotropic undulations upon compression, even beyond high strain where the patterned regions localize, whereas the patterned films show much more complex behavior. For a better understanding of how the buckling profiles of isolated plates are affected by a change in the boundary conditions, we studied local strains of plates as the boundary condition is changed. A simple scaling model have been developed by using the concept of two springs connected in series. The ratio of local strain of a plate to the global strain is plotted as a function of the exposure time of the "in between plates" which reasonably fit our experimental observation, especially in the limits of large exposure times of the boundary regions. In addition, the patterned regions provide interesting behavior in how the isolated films can localize their strains as the applied strain increases. In order to understand this behavior, an equilibrium shape of the deformation height profile was modeled numerically by a simple model that made use of certain local boundary conditions. The agreement between our experimental and numerical height profile is remarkable.

Finally, the responses of discrete systems (colloidal layers) to mechanical deformations have been exploited in the last chapter. Here, a combined experimental methods and theoretical modeling has been designed and used for the better understanding of the responses. Experimentally, the colloidal layers were made on freshly cleaved mica from polystyrene and silica particles of variable sizes (diameters ranging from $3nm$-$10\mu m$) and transferred to an elastic substrate, polydimethylsiloxane (PDMS) before subjected to a compressive stress. The buckling profiles measured, when the system is under compression, demonstrate a great insight that the continuum model may not be able to predict such discrete systems. Theoretically, a granular model was constructed and structural stability analysis was investigated in both the pre-buckling and post-buckling regimes in order to predict the experimental observations. Specifically, by considering the small strain limit (linear-analysis), the threshold buckling wavelength observed experimentally ($\lambda_C/2R \sim 5.3$) has been remarkably predicted. On the other hand, by analyzing the large strain limit (non-linear analysis to post-buckling regime), both the buckling wavelength and amplitude evolutions as a function of increasing strain were also successfully predicted by the model. The agreement of the experimental and theoretical observations was remarkable.

# BIBLIOGRAPHY


[1] Argon, A. S., Andrews, R. D., Godrick, J. A., and Whitney, W., J. Appl. Phys. **39** (1968), 1899–1906.

[2] Audoly, B., and Pomeau, Y., *Elasticity and geometry*, Oxford University Press, 2010.

[3] Balzer, B. N., et al., ACS applied materials & interfaces **5** (2013), no. 13, 6300–6306.

[4] Bates, F. S., and Fredrickson, G. H., Annu. Rev. Phys. Chem. **41** (1990), 525–557.

[5] Bates, F. S., Science **251** (1991), 898–905.

[6] Bates, F. S., and Fredricksonl, G. H., Physics Today **52** (1999), 32.

[7] Berdichevsky, Y., et al., Sensors and Actuators B: Chemical **97** (2004), no. 2, 402–408.

[8] Berg, J. C., *An introduction to interfaces & colloids: the bridge to nanoscience*, World Scientific, 2010.

[9] Berthier, L., and Biroli, G., Reviews of Modern Physics **83** (2011), no. 2, 587.

[10] Bodiguel, H., and Fretigny, C., Phys. Rev. Lett. **97** (2006), 266105.

[11] Böhme, T. R., and de Pablo, J. J., J. Chem. Phys. **116** (2002), 9939–9951.

[12] Bowden, N., Brittain, S., Evans, A. G., Hutchinson, J. W., and Whitesides, G. M., Nature **393** (1998), 146–149.

[13] Bower, D. I., *An introduction to polymer physics*, Cambridge University Press, 2002.

[14] Brown, H. R., and Russell, T. P., Macromolecules **29** (1996), 798–800.

[15] Cerda, E., and Mahadevan, L., Phys. Rev. Lett. **90** (2003), 074302.

[16] Chai, H., Babcock, C. D., and Knauss, W. G., International Journal of Solids and Structures **17** (1981), no. 11, 1069–1083.

[17] Chattopadhyay, S., Datta, A., Giglia, A., Mahne, N., and Nannarone, S., arXiv preprint arXiv:0709.2528 (2007).

[18] Chen, K., and Schweizer, K. S., Macromolecules **44** (2011), no. 10, 3988–4000.

[19] Chen, Y., et al., Nature **423** (2003), 136.

[20] Chung, J. Y., Lee, J. H., Beers, K. L., and Stafford, C. M., Nano. Lett. **11** (2011), 3361–3365.

[21] Chung, J. Y., et al., Adv. Mater. **23** (2011), 349–368.

[22] Chung, P. C., Glynos, E., and Green, P. F., Langmuir (2014).

[23] Croll, A. B., and Crosby, A. J., Macromolecules **45** (2012), no. 9, 4001–4006.

[24] Croll, A. B., Tordesillas, A., Carey, D., and Gurmessa, B., AIP Conference Proceedings, vol. 1542, 2013, p. 409.

[25] Dalnoki-Veress, K., et al., Phys. Rev. E **63** (1996), 031801–031810.

[26] Dalnoki-Veress, K., Forrest, J., Murray, C., Gigault, C., and Dutcher, J., Physical review E **63** (2001), no. 3, 031801.

[27] Denkov, N., et al., Langmuir **8(12)** (1992), 3183.

[28] Diamant, H., and Witten, T. A., arXiv (2010), 1009.2487v1.

[29] Diamant, H., and Witten, T. A., Physical review letters **107** (2011), no. 16, 164302.

[30] Dutcher, J. R., and Marangoni, A. G. (eds.), *Soft materials: Structure and dynamics*, Marcel Dekker, New York, 2005.

[31] Ebata, Y., Croll, A. B., and Crosby, A. J., Soft Matter **8** (2012), 9086–9091.

[32] Eduard, V., and Theodor, K., *Thin plates and shells*, Marcel Dekker, Inc, 2001.

[33] Egitto, F., Matienzo, L., Spalik, J., and Fuerniss, S., *Removal of poly (dimethylsiloxane) contamination from silicon surfaces with uv/ozone treatment*, MRS Proceedings, vol. 385, Cambridge Univ Press, 1995, p. 245.

[34] Ellison, C. J., and Torkelson, J. M., Nature Mater. **2** (2003), 695–700.

[35] F. D. Egitto, L. J. M., J Mater Sci **41** (2006), 6362–6373.

[36] Fakhraai, Z., and Forrest, J. A., Science **319** (2008), 600.

[37] F.Green, P., and Limary, R., Adv. in Colloidal and Interface Science **94** (2001), 53–81.

[38] Forrest, J. A., et al., Phys. Rev. Lett **77** (1996), 0031–9007.

[39] Forrest, J. A., et al., Advances in Colloid and Interface Science **94** (2001), 167–196.

[40] G., D. G. P., *Scaling concepts in polymer physics*, Cornell University, Ithaca, New York, 1979.

[41] Gedde, U., *Polymer physics*, Springer, 1995.

[42] Gray, L. A. G., and Roth, C. B., Soft Matter, DOI:10.1039/c3sm52113c (2014).

[43] Groenewold, J., Physica A. **298** (2001), 32–45.

[44] Grozea, C. M., Li, I. T., Grozea, D., and Walker, G. C., Macromolecules **44** (2011), no. 10, 3901–3909.

[45] Gu J, Bullwinkel MD, C. G., J. Electrochem. Soc. **142** (1995), 907–913.

[46] Gurmessa, B., and Croll, A., Phys. Rev. Lett **110** (2013), 074301.

[47] H, T., et al., materialstoday **13** (2010), 0025.

[48] Hamley, W., *The physics of block copolymers: Introduction*, Oxford University Press, 1998.

[49] Hasan, O. A., and Boyce, M. C., Polymer **34** (1993), 5085–5092.

[50] Hasegawa, H., Hashimoto, T., Kawai, H., Lodge, T. P., Amis, E. J., Glinka, C., and Han, C. C., Macromolecules **18** (1985), no. 1, 67–78.

[51] Honeker, C. C., and Thomas, E. L., Chemistry of Materials **8** (1996), no. 8, 1702–1714.

[52] Howarter, J. A., and Stafford, C. M., Soft Matter **6** (2010), no. 22, 5661–5666.

[53] Hunter, G. L., and Weeks, E. R., Reports on Progress in Physics **75** (2012), no. 6, 066501.

[54] Hutchinson, J. W., and Suo, Z., Adv. Appl. Mech **29** (1992), 63–191.

[55] Ji, S., Liu, C.-C., Son, J. G., Gotrik, K., Craig, G. S., Gopalan, P., Himpsel, F., Char, K., and Nealey, P. F., Macromolecules **41** (2008), no. 23, 9098–9103.

[56] Jones, R. A., *Soft condensed matter*, 2002.

[57] Jones, R. A., and Richards, R. W., *Polymers at surfaces and interfaces*, Cambridge University Press, 1999.

[58] K. Norrman, A. G.-S., and Larsen, N. B., Annu. Rep. Prog. . Chem., Sect. C **101** (2005), 174–201.

[59] Kahl, D.-Y., and Others, Adv. Funct. Mater. **18** (2008), 1–11.

[60] Keddie, J. L., Jones, R. A. L., and Cory, R. A., Europhys. Lett. **27** (1994), 59–64.

[61] Keddie, J., and Jones, R., Israel journal of chemistry **35** (1995), no. 1, 21–26.

[62] Khang, D.-Y., et al., Science **311** (2006), 208–212.

[63] Khang, D.-Y., Rogers, J. A., and Lee, H. H., Adv. Funct. Mater. **19** (2009), 1526–1536.

[64] Kondic, L., Siam review **45** (2003), 95–115.

[65] Kramer, E. J., J. Macrom. Sci. B **10** (1974), 191–205.

[66] Kramer, E. J., Crazing in polymers, Springer, 1983, pp. 1–56.

[67] Landau, L. D., and Lifshitz, E., *Theory of elasticity, vol. 7*, Course of Theoretical Physics **3** (1986).

[68] Landau, L. D., and Lifshitz, E. M., *Fluid mechanics: Landau and lifshitz: Course of theoretical physics*, vol. 6, Elsevier, 2013.

[69] Lawrence CJ, Z. W., Journal of Nonnewtonian fluids **39** (1991), 137–187.

[70] Lee, J.-H., Chung, J. Y., and Stafford, C. M., ACS Macro. Lett. **1** (2012), 122–126.

[71] Lee, J.-Y., and Crosby, A. J., Macromolecules **38** (2005), 9711–9717.

[72] Leibler, L., Macromolecules **13** (1980), 1602–1617.

[73] M., D., and F., E. S., *Theory of polymer dynamics*, Clarendon Press, Oxford, 1986.

[74] M. C. M. van der Sanden, H. E. M., and Lemstra, P. J., Polymer. **34** (1993), 2148.

[75] Mai, Y., and Eisenberg, A., Chem. Soc. Rev., (1996).

[76] Makke, A., Perez, M., Lame, O., and Barrat, J.-L., Proceedings of the National Academy of Sciences **109** (2012), no. 3, 680–685.

[77] Mark F. Schulz, A. K. K., and Bates, F. S., Macromolecules. (1996).

[78] Masson, J. L., and Green, P. F., Phys. Rev. E. **65** (2002), 031806.

[79] McGraw, J. D., Fowler, P. D., Ferrari, M. L., and Dalnoki-Veress, K., The European physical journal. E, Soft matter **36** (2013), no. 1, 7–7.

[80] Mei, H., Landis, C. M., and Huang, R., Mech. Mater. **43** (2011), 627–642.

[81] Mei, H., and Others, Appl. Phys. Lett. **90** (2007), 151902.

[82] Michler, G., Journal of Materials Science **25** (1990), no. 5, 2321–2334.

[83] Miller, A. F., Science **137** (2007), 605–606.

[84] Miquelard-Garnier, G., et al., Soft matter **6** (2010), 5789–5794.

[85] OConnell, P. A., M., Science **307** (2005), 1760.

[86] Oron, D., and Bankoff, Rev. Mod. Phys **69** (1997), 931–980.

[87] Ortiz, M., , and ., G. G., J. Mech.Phys. Sol. **42** (1994), 531–559.

[88] Ouyang, M., et al., Journal of Membrane science **177** (2000), no. 1, 177–187.

[89] Oz Oshri, F. B., and Diamant, H., arXiv:1503.01674 [cond-mat.soft].

[90] Park, C. H., Kim, J. H., Ree, M., Sohn, B.-H., Jung, J. C., and Zin, W.-C., Polymer **45** (2004), no. 13, 4507–4513.

[91] PC, S., JES **138** (1991), 1712–1719.

[92] Peters, J., Muthuswamy, M., Wibowo, J., and Tordesillas, A., Physical review E **72** (2005), no. 4, 041307.

[93] Pocivavsek, L., Dellsy, R., Kern, A., Johnson, S., Lin, B., Lee, K.-Y. C., and Cerda, E., Science **320** (2008), 912–916.

[94] Puttick, K., Journal of Physics D: Applied Physics **11** (1978), no. 4, 595.

[95] Pye, J. E., and Roth, C. B., Phys. Rev. Lett. **107** (2011), 235701.

[96] Reis, P. M., et al., Phys. Rev. Lett **103** (2009), 045501.

[97] Reiter, G., Macromolecules **27** (1994), 3046–3052.

[98] Roth, C. B., and Dutcher, J. R., Journal of Electroanalytical Chemistry **584** (2005), no. 1, 13–22.

[99] Rubinstein, Michael; Colby, R. H., *Polymer physics*, Oxford University Press, USA, 2003.

[100] Russell, T. P., et al., Adv.Mater **21** (2009), 4769–4792.

[101] Ryu, C. Y., Ruokolainen, J., Fredrickson, G. H., Kramer, E. J., and Hahn, S. F., Macromolecules **35** (2002), no. 6, 2157–2166.

[102] Sarva, S., and Boyce, M., Journal of Mechanics of Materials and Structures **2** (2007), no. 10, 1853–1880.

[103] Segalman, R. A., Materials Science and Engineering R **48** (2005), 191–226.

[104] Serway, R., and Jewett, J., *Physics for scientists and engineers*, Cengage Learning, 2013.

[105] Sharp, J. S., et al., Phys. Rev. Lett **91** (2003), 0031–9007.

[106] Si, L., Massa, M. V., Dalnoki-Veress, K., Brown, H. R., and Jones, R. A. L., Phys. Rev. Lett. **94** (2005), 127801.

[107] Sivaniah, E, H. Y., Matsubara, S., Kiyono, S., Hashimoto, T., Fukunaga, K., Kramer, E., and Mates, T., Macromolecules **38** (2005), no. 5, 1837–1849.

[108] Skibo, M., Hertzberg, R., Manson, J., and Kim, S. d., Journal of Materials Science **12** (1977), no. 3, 531–542.

[109] Sperling, L. H., *Introduction to physical polymer science*, A John Wiley and Sons, Inc., 2006.

[110] Stafford, C. M., Harrison, C., Beers, K. L., Karim, A., Amis, E. J., Vanlandingham, M. R., Kim, H.-C., Volksen, W., Miller, R. D., and Simonyi, E. E., Nature Mater. **3** (2004), 545–550.

[111] Strobl, G. R., *The physics of polymers: Concepts for understanding their structures and behavior*, Springer, 2007.

[112] Stuart, M. A. C., et al., Nature materials **9** (2010), no. 2, 101–113.

[113] Teraoka, I., *Polymer solutions: An introduction to physical properties*, John Wiley & Sons, 2002.

[114] Timoshenko, S., *Theory of elastic stability*, McCGraw-Hill Book Componey, 1961.

[115] Tiwari, A. N., and Others, Prog. Photovolt: Res. Appl **9** (2001), 211–215.

[116] Tordesillas, A., Carey, D., Croll, A. B., Shi, J., and Gurmessa, B., Granular Matter (2013), 1–10.

[117] Tsui, O. K., and Zhang, H., Macromolecules **34** (2001), no. 26, 9139–9142.

[118] Vella, D., Bico, J., Boudaoud, A., Roman, B., and Reis, P. M., Pro. Nat. Acad. Sci. **106** (2009), 10901–10906.

[119] Vorselaars, B., Lyulin, A. V., and Michels, M. A. J., The Journal of Chemical Physics **130** (2009), no. 7, –.

[120] Wallace, W. E., van Zanten, J. H., and Wu, W. L., Phys. Rev. E **52** (1995), R3329–R3332.

[121] Weidisch, R., Ensslen, M., Michler, G., and Fischer, H., Macromolecules **32** (1999), no. 16, 5375–5382.

[122] Widin, J. M., et al., Macromolecules **46** (2013), 4472–4480.

[123] Witten, T. A., Rev. Mod. Phys. **79** (2007), 643–675.

[124] Witten, T. A., *Structured fluids, polymers, colloids and surfactants*, Oxford University Press, 2004.

[125] Wu, et al., Macromolecules **34** (2001), no. 16, 5627–5634.

[126] Xia, et al., EJGE **14** (2009).

[127] Xiang, H., Shin, K., Kim, T., Moon, S., McCarthy, T., and Russell, T., Journal of Polymer Science Part B: Polymer Physics **43** (2005), no. 23, 3377–3383.

[128] Yu, C., and Jiang, H., Thin Solid Films **519** (2010), no. 2, 818–822.

[129] Yu, H. H., and Huchinson, J. W., Int. J. Fract. **113** (2002), 39–55.

[130] Yu, H.-H., and Hutchinson, J. W., International Journal of Fracture **113** (2002), no. 1, 39–55.

[131] Zhang, L., Wang, Y., and Zhang, J., Physical Review E **89** (2014), no. 1, 012203.